ACTIVE FLUID MECHANICS FOR PROGRAMMABLE MATTER

A Dissertation

Presented to the Faculty of the Graduate School

of Cornell University

In Partial Fulfillment of the Requirements for the Degree of

Doctor of Philosophy

by

Mekala Krishnan

August 2011

ACTIVE FLUID MECHANICS FOR PROGRAMMABLE MATTER

Mekala Krishnan, Ph. D.

Cornell University 2011

In this research I have explored the use of fluid mechanics to create programmable matter. Programmable, reconfigurable systems are those whose properties can be reconfigured on-the-fly, either on-command to enhance functionality, or autonomously in response to internal/external stimuli. I have investigated two approaches to creating such programmable systems. In the first approach, I have used microfluidics to carry out directed fluidic assembly of microscale tiles to create programmable and reconfigurable target structures, while in the second approach, I have examined the use of optofluidics to reconfigure flow pathways and build morphable channel structures on a microfluidic device, thus creating programmable microfluidic systems.

BIOGRAPHICAL SKETCH

Mekala Krishnan was born in 1984 in New Delhi, India. She did her undergraduate education at the Indian Institute of Technology Delhi, India, where she received a Bachelor of Technology degree in Mechanical Engineering. In November 2006, Mekala joined Prof. David Erickson's "Integrated Micro- and Nanofluidic Systems Laboratory" at the Sibley School of Mechanical and Aerospace Engineering, Cornell University as a PhD student. She was awarded a Master of Science degree in Mechanical Engineering in August 2009.

ACKNOWLEDGMENTS

I would like to begin by thanking my PhD advisor, Prof. David Erickson. I have learnt a tremendous amount during my time in his research group, both academically and otherwise and for this, I am very grateful. He has been a great mentor, and someone whose work ethic, drive and dedication I will always strive to emulate. I would also like to thank the other members of my PhD committee; Prof. Hod Lipson, Prof. Sunil Bhave and Prof. Sidney Leibovich. I have always enjoyed, been stimulated by and learnt much from my discussions with them and I deeply appreciate their support and advice during my PhD. I would also like to thank other professors I have been fortunate enough to interact with along the way; Professor Brian Kirby for a wonderful class on microfluidics and the late Professor Kenneth Torrance who taught me how rewarding teaching can be.

I would also like to thank all the members of my research group, the "Integrated Micro- and Nanofluidic Systems Laboratory" with whom I have had many incredible intellectual discussions, particularly Bernardo Cordovez, Sudeep Mandal and Aram Chung, who have been wonderful colleagues and friends. I also thank Michael Tolley and Joonsik Park, whom I have been fortunate enough to collaborate with on various projects.

My time at Cornell has been among the best years of my life and I have crossed paths with many wonderful people, all of whom I have learnt a lot from. Alex Barbati who helped me keep my sanity and always gives me perspective, and Rajendran Narayanan, Krishna Iyengar and Boram Kim who helped me experience a world outside of my research. I would also like to thank Michael Kalontarov, Edgar Cuji and Vishal Tandon, who have been wonderful colleagues and friends, Denise Wong, one of the happiest people I know, Joyjit Roy, a great statistician and Pavithra

Sundararajan, who was always willing to have long discussions with me on fluid mechanics. Finally, other friends that have supported me during my time at Cornell including Swastika Shreshtha, Sowmya Kondapalli, Natalie Galley, Janet Shen and Abhishek Ramkumar. I also am grateful to my friends from college, who have visited me in remote Ithaca from all corners of the world; Rashi Goyal, Prerna Dubey, Pooja Arya, Aditya Agrawal and Nidhi Nakra.

I especially thank Marcia Sawyer, our Graduate Field Administrator, an incredible person who manages to make everything look easy and whose office I always leave with a weight off my shoulders.

Finally, I would like to thank my family. My brother, Nikhil, who has been an inspiration, perhaps without which I would never have gone down this path, as well as his wife, Sonia. My cousin, Raghu, who always had a kind ear for someone experiencing a mid-PhD crisis. My aunt, Usha Rajagopal, who first taught me what efficiency meant, and who was never more than a phone call away. My parents, who helped me on my path to engineering, and who have had to put up with years of uncertainty during my PhD. Thank you for believing in me, and for all your support, encouragement, tidying up and worrying! Last, but certainly not least, I would like to thank my twin sister Akhila with whom I have had innumerable conversations during work hours and without whom I could not have finished my PhD.

TABLE OF CONTENTS

LIST OF FIGURES

LIST OF TABLES

LIST OF SYMBOLS

ρ	=	mass density
U	=	fluid velocity
v	=	velocity
μ	=	dynamic viscosity
α	=	thermal diffusivity
k	=	thermal conductivity
c_p	=	specific heat
Re	=	Reynolds number
Pe	=	Peclet number
p	=	pressure
F	=	Faraday's constant
$\boldsymbol{F}$	=	Force
$\boldsymbol{T}$	=	Torque
T	=	temperature
Φ	=	electric potential
λ_D	=	Debye length
ε	=	permittivity of the medium
ζ	=	surface (zeta) potential
k_b	=	Boltzmann's constant
v_{EO}	=	electroosmotic velocity
$D_{x,y}$	=	translational docking parameter
D_θ	=	rotational docking parameter

CHAPTER 1

INTRODUCTION

1.1 Research Scope

In this research, I have explored the use of fluid mechanics to create programmable matter. Programmable, reconfigurable systems are those whose properties can be reconfigured on-the-fly, either on-command to enhance functionality, or autonomously in response to internal/external stimuli. I have examined the problem of how to create programmable systems from two different directions; in the first approach I have looked at the use of microfluidics to carry out directed fluidic assembly to create programmable matter, and in the second, I have examined the use of optofluidics to create programmable microfluidic systems.

In this chapter, I will lay out an overview of the literature related to these research areas. To that end, I will begin with a brief introduction to programmable matter and discuss the advantages of these systems. This shall be done specifically in the context of the two approaches I have taken to the implementation of this paradigm, specifically microscale assembly and creating reconfigurable microfluidic systems. I will then discuss the broad research fields I have explored to develop programmable matter, namely microfluidics and optofluidics. My research accomplishments will then be presented in detail in Chapters 2 through 5 and I will finally conclude in Chapter 6 with a presentation of the impact of my work along with potential future directions.

1.2 Programmable Matter

1.2.1 Microscale Assembly

Manufacturing using traditional top down device fabrication approaches based on lithography are essentially two dimensional in nature, and require that the various components of a device be manufactured using compatible fabrication technologies. Self-assembly[1-8] offers advantages over these top down fabrication techniques in that they enable the fabrication of three dimensional structures[9] from non-uniform sub-elements, allowing designers to build devices comprising of complex arrays of different materials or functionalities which would be impossible to achieve using traditional microfabrication techniques[10]. However, these self-assembly methods are largely stochastic in nature and rely on large component numbers to carry out successful assembly and reduce errors. These techniques lend themselves well to the building of regular structures rather than irregular shapes which reduces the scope of applications for these methods. Finally, since the affinity between two components is static in nature, thus the assembling components need to be carefully designed for each target structure and cannot be used for other target structures, limiting the versatility of these methods. Thus, the creation of truly programmable materials whose functionality can be rapidly tuned on the fly is difficult with such top-down as well as bottom-up approaches.

To overcome these limitations, I describe an alternative approach based on directed fluidic assembly that offers the potential to build programmable matter. This approach can be applied to create target structures that are dynamically reconfigurable with irregular shapes and can also be used to correct for any errors that occur during the

assembly process. Chapter 2 describes the approach and the modeling work I have done to understand the fluid mechanics and the fluid-solid interactions that arise during the assembly scheme, as well as analyze various kinds of assembly schemes. Chapter 3 then describes experimental work done to implement dynamically tunable affinities between assembling components to directly reconfigure assembled components, create irregular components and correct for assembly errors.

1.2.2 Reconfigurable Microfluidics

Programmable systems are those that change their properties on-command, to enhance functionality, or autonomously, in response to internal/external stimuli. The Field Programmable Gate Array (FPGA) is perhaps the best example of a commercial application of reconfiguration, that has resulted in numerous benefits to the field of electronics including versatility, cost, adaptability, robustness, and security. However, despite these advantages, this paradigm has seen limited development in the case of other chip-based technologies. Specific to the field of microfluidics, the ability to dynamically control and manipulate fluid flow is crucial to the development of nearly all lab-on-chip technologies[11]. The creation of programmable microfluidic systems with reconfigurable transport pathways could allow one to change the analysis performed on a chip based on results upstream, correct for manufacturing by rerouting flows along alternate pathways and also lower overall costs by producing versatile and robust devices.

As will be discussed in more detail later, microfluidic devices can either be characterized as being channel-based[12,13], or discrete droplet translocation based[14-16].

The latter are largely reconfigurable since it is relatively straightforward to fabricate an array of electrodes on a chip to actuate a droplet around an arbitrary path. At present however the vast majority of microfluidics is done using channel-based chips that are fundamentally limited in that the flow control structures need to be designed, fabricated and placed on the microchip *a priori* and cannot be reconfigured. As will be discussed in more detail in Chapters 4 and 5, the field of optofluidics[17,18] does offer potential solutions to these issues[19-23], though many of these approaches offer only limited reconfigurability or are or have engineering limitations such as slow flow rates (on the order of a few hundred micrometers per second) and/or poor switching times (on the order of tens of minutes to hours). In those chapters, I will propose a novel optofluidic approach to creating reconfigurable microfluidic systems. This approach, initially implemented to create reconfigurable valves (Chapter 4) is then adapted to dynamically and rapidly tune flow environments and reconfigure entire flow pathways (Chapter 5). The application of this technique as a biological analysis tool, through the trapping of nanoparticles and biomolecules is also demonstrated here.

1.3 Microfluidics

Microfluidics is defined as the study of fluid flow and transport having a characteristic dimension between about 100nm and 100μm[24]. This area has considerably expanded and developed in the last twenty years due to advancements in microfabrication that have led to the ability to create two and three dimensional microchannel networks. Today, the broad applications of this field are largely related to creating lab-on-chip technologies for chemical and biological analysis as well as

small scale energy production. These devices have unique engineering advantages including small size and minimized reagent consumption[25], as well as the ability to utilize phenomena like surface tension[14,26] and optical forces[17] that become particularly significant at these size scales. Beyond improvements in microfabrication[27-29], microfluidics has also benefited from the development of on-chip flow control elements such as valves, pumps and mixers[29-32].

Microfluidic devices broadly categorized as being either channel-based, *i.e*. based on continuous transport or microchannel flows, or droplet-based, *i.e.* based on the manipulation of discrete droplets[14,26]. The former category of devices are actuated using pressure or electrokinetics while digital or droplet based microfluidics systems usually consist of devices on open substrates driven with techniques such as electrowetting[14,26] and thermal actuation [33]. Further details on microscale transport can be obtained from a review by Stone *et al.*[11]

Microscale flow transport differs from that at larger scales in being characterized by strongly laminar behavior, having more significant surface tension effects (particularly relevant at the nanoscale, and for droplet based microfluidic systems), and the influence of electrokinetics on these flows. Another characteristic of microfluidic flows is their poor mixing ability; while laminar behavior makes it easy to control flows, it leads to poor mixing (particularly relevant for biological or chemical analysis systems). In the following sections, I will briefly describe the relevant equations of flow and the two main transport phenomena important to channel-based microfluidics, namely pressure driven flow and electrokinetic flow. Droplet-based microfluidic systems will not be discussed in more detail as they are not

directly relevant to my research, and the reader is referred to Stone *et al.*[11] for more details on these systems.

1.3.1 Equations of flow

Microfluidic and nanofluidic flow can be well described by continuum mechanics[34] with the Navier-Stokes equations used in traditional fluid mechanics. The Reynolds number, Re of these systems is usually much less than one where Re = $\rho L v_o / \eta$ where L is the characteristic length scale of the system, v_o is the characteristic velocity and ρ and η are the fluid density and viscosity respectively. For example, a channel containing water having a characteristic length of 50 μm and a flow velocity of 100 μm/s has a Reynolds number on the order of 0.005. The equations of continuity and the Navier-Stokes equations (for momentum balance) respectively for an incompressible, Newtonian fluid with constant fluid properties are as below:

$$\nabla \cdot \boldsymbol{v} = 0 \qquad (1.1a)$$

$$\rho\left(\frac{\partial \boldsymbol{v}}{\partial t} + \boldsymbol{v} \cdot \nabla \boldsymbol{v}\right) = -\nabla p + \eta \nabla^2 \boldsymbol{v} \qquad (1.1b)$$

where $\boldsymbol{v}$ is the fluid velocity and p is the fluid pressure. In the limit of low Reynolds number, the Navier-Stokes equations reduce to the Stokes equations, with the time dependent and convective transport terms on the left side of the momentum equation (1.1b) dropping out to yield

$$\nabla \cdot \boldsymbol{v} = 0 \qquad (1.2a)$$

$$0 = -\nabla p + \eta \nabla^2 \boldsymbol{v} \qquad (1.2b)$$

We note here that the dropping of the time dependent term results in microfluidic flows being characterized as time independent. For a physical system, this implies that the transient period between when flow conditions are changed is very short and in many cases the flow response to external changes (for example input pressures) can be assumed to be instantaneous. For electroosmotic flow, suitable modifications may be made to Equation 1.2 as will be discussed below.

1.3.2 Pressure Driven Flow

Pressure driven flow is commonly used for microfluidics, being robust with little dependence on fluid and surface properties. Flow is usually driven using off chip pneumatics or syringe pumps, along with on-chip valves[13,29] to locally manipulate flow. The characteristic flow velocity profile in a pressure driven system can be calculated from Equation 1.2 above where pressure is applied along the *x* direction and the channel is sufficiently wide such that flow is not affected by the sidewalls of the channel. For a channel height of *2b*, the solution to Equation 1.2 is described by a Poiseuille flow profile as shown below:

$$v_x(y) = -\frac{1}{2\eta}\left(\frac{dp}{dx}\right)\left(b^2 - y^2\right) \qquad (1.3)$$

where v_x is the fluid velocity along the *x* direction. Here the term *dp/dx* represents the applied pressure gradient along the *x* direction. For a simple channel geometry, $dp/dx = (p_2-p_1)/L$. Thus, the flow velocity in pressure driven flow exhibits a parabolic profile across the channel height with flow being faster in the center of the channel than near the edges, where it is zero (as enforced by the no slip boundary condition).

The above equation clearly indicates the limitations of pressure driven flow to actuate microfluidic devices. Firstly, we see that pressure driven flow does not scale well with small channel sizes, since flow velocity is proportional to the square of the channel size. Additionally, the parabolic velocity profile can lead to significant dispersion of a transported chemical sample or tumbling of larger objects like cells as the flow in the middle is faster than that near the wall.

1.3.3 Electrokinetic Flow

Electrokinetic flow phenomena refer to a larger family of flow phenomena including electroosmosis, electrophoresis and dielectrophoresis. It is mainly used as a transport mechanism for lab-on-chip type devices and has been used to transport, separate and concentrate a range of species in [35-38]. Electrokinetic flow helps overcome some of the limitations of pressure driven flow discussed above, as the flow exhibits a flat velocity profile (plug flow) with minimal dispersion and flow vorticity. It also scales well with smaller channel dimensions, having an average velocity that is largely independent of channel height. However, this technique has other limitations, being less robust than pressure driven flow as appreciable flow velocities can only be obtained for low ionic concentration aqueous solutions and under certain surface conditions, and electric fields. Additionally, joule heating effects in such systems can prove to be fairly significant[39].

The net particle velocity in electrokinetically driven flow, $\boldsymbol{v}_p$ is given by

$$\boldsymbol{v}_p = \boldsymbol{v}_{flow} + \boldsymbol{v}_{ep} + \boldsymbol{v}_{dep} \qquad (1.4)$$

where $\boldsymbol{v}_{flow}$ is the velocity of the flow at the location of the particle, $\boldsymbol{v}_{ep}$ is the electrophoretic velocity of the particle and $\boldsymbol{v}_{dep}$ is the dielectrophoretic velocity of the particle. $\boldsymbol{v}_{flow}$ represents the speed at which the particle is advected with the bulk fluid motion and could be due to an applied external pressure (as discussed in the previous section) and/or an electroosmotic flow velocity which is described below.

Electroosmotic flow is driven by the interaction of the electrical double layer (EDL) with an externally applied field. The EDL usually forms due to the absorption or desorption of charged species from the channel surface [36,37], with a characteristic depth given by the inverse of the Debye-Hückel parameter (1/κ). This depth is dependent on the ionic strength of the bulk solution and can range from a few nanometers to over a micrometer. Electroosmotic flow occurs when an electric field is applied across a channel that then exerts a net force on the excess ions present in the fluid. These are dragged along the channel walls, pulling the rest of the fluid in the channel. The flow equations describing this flow can be modified from the Stokes equations above by adding a Coulombic force term because of the ions in the EDL, giving

$$\nabla \cdot \boldsymbol{v} = 0 \qquad (1.5a)$$

$$\eta \nabla^2 \boldsymbol{v} = \nabla p + \rho_e \nabla \phi \qquad (1.5b)$$

where ρ_e is the charge density in the electrical double layer and $\boldsymbol{\nabla\phi}$ is the gradient of the electrical potential. A common simplification of this equation is the Helmholtz-Smoluchowski approximation [35], applicable in the limit of a thin EDL that yields an electroosmotic velocity, $\boldsymbol{v}_{eo}$, at the edge of the double layer as

$$\boldsymbol{v}_{eo} = \mu_{eo}\nabla\phi = \mu_{eo}\boldsymbol{E} = -\frac{\varepsilon\varepsilon_o\zeta}{\eta}\boldsymbol{E} \qquad (1.6)$$

where μ_{eo} is the electroosmotic mobility, $\boldsymbol{E}$ is the applied electric potential, ζ is the zeta potential, ε_o is the permittivity of a vacuum ($\varepsilon_o = 8.854x10^{-12}$ *C/Vm*), ε is the dielectric constant of the particle and η is the fluid viscosity. For more details on electrokinetic transport, including governing equations and practical implementations, it is suggested that readers consult Erickson and Krishnan[24].

1.4 Optofluidics

The field of optofluidics[17,18,40] broadly refers to two different research areas that are concerned with the fusion of optics with micro- and nanoscale fluidics. The first relates to the use of fluids and microfluidic transport to enhance the functionality of optical devices while the second relates to the use of optical phenomena to influence microfluidic transport. The latter includes a variety of different techniques ranging from the use of optical forces to manipulate particles and flows directly[41-45] as well as indirectly, through the interaction of optics with electronic[21], chemical[46] and thermal effects[47,48]. The latter of these two approaches to optofluidics is relevant to the scope of the thesis, and a brief background into this particular aspect field is given in what follows. For more details on the former, the reader is referred to the recent book chapter by Krishnan and Erickson[49].

1.4.1 Optically enabled microfluidic transport

1.4.1.1 Governing Equations

The optical force is defined using a stress tensor (similar to the stress tensor used to describe fluidic forces) [50]. The force on a system, $\boldsymbol{F}$ is the sum of all the forces, $\boldsymbol{f}_V$ on each of the volume elements, dV of the system. Thus,

$$\boldsymbol{F} = \int \boldsymbol{f}_V(\boldsymbol{r}) dV \qquad (1.7)$$

The volume integral is converted to a surface integral using a second order tensor, $\boldsymbol{T}$, to give

$$\boldsymbol{F} = \int \nabla \cdot \boldsymbol{T} dV = \oint \boldsymbol{T} \cdot \boldsymbol{dS} \qquad (1.8)$$

where $\boldsymbol{dS}$ is an infinitesimal surface element. In the case of electromagnetics, this tensor is called the Maxwell Stress Tensor (MST) and is given by

$$\boldsymbol{T} = \varepsilon_o \varepsilon_m \boldsymbol{EE} + \mu_o \mu_m \boldsymbol{HH} - \frac{1}{2}\boldsymbol{I}\left(\varepsilon_o \varepsilon_m \boldsymbol{E} \cdot \boldsymbol{E} + \mu_o \mu_m \boldsymbol{H} \cdot \boldsymbol{H}\right) \qquad (1.9)$$

where $\boldsymbol{E}$ and $\boldsymbol{H}$ refer to the electric and magnetic fields respectively, ε_o is the permittivity of a vacuum ($\varepsilon_o = 8.854 \times 10^{-12}$ *C/Vm*), ε_m is the dielectric constant of the medium, μ_o is the permeability of a vacuum ($\mu_o = 4\pi \times 10^{-7}$ *NA*$^{-2}$), μ_m is the relative permeability of the medium, $\boldsymbol{I}$ is the identity tensor and the dyadic notation is implied in the first two terms above. Thus the optical force exerted can be calculated by finding the electromagnetic field (or the optical field), yielding $\boldsymbol{E}$ and $\boldsymbol{H}$ and Equation 1.8 can then be used to find the optical force.

1.4.1.2 Manipulation of Fluids with Optical Forces

Optical actuation to drive fluid flow is particularly advantageous, being a non-contact means of actuation and and can also be dynamically reconfigurable in that one need not predefine a microfluidic network beforehand. Light is used to manipulate fluids in two ways. In the first approach, light is used to control the path of a fluid which is actuated by some other transport mechanism. In the second, the fluid is actuated using light, either through radiation pressure, or through indirect means like photothermal effects. The former will be discussed in more detail in the section on reconfigurable microfluidics. An example of the latter is work by Wunenburger *et al.* [51,52], who used laser light impinging on an interface between two fluids with different refractive indices to deform the interface. It has been shown that similar light induced interfacial deformations can lead to fluid dynamical instabilities and create liquid jets of microdroplets [53]. These "opto-hydrodynamic" instabilities have also been used to form large aspect ratio liquid channels and guide light through the channels [54,55]. Laser actuation has been used in droplet-based microfluidic systems as well, to drive the motion of droplets using the thermocapillary effect, where a droplet in a carrier fluid placed in a thermal gradient experiences a surface tension gradient due to the dependence of surface tension on temperature [23]. This in turn induces a viscous stress in both fluids, resulting in interfacial flow. Finally, and perhaps more relevant for this thesis, absorption of laser light can be used to create thermal gradients and thus drive droplet flow. Laser induced thermocapillary forces have been used to carry out mixing in microchannels, make optofluidic valves and carry out sorting and merging of droplets [56,57]. Finally, fluidic actuation has also been carried out using photothermal

nanoparticles suspended near the liquid-air interface of a microchannel[22]. These nanoparticles convert optical energy from a laser beam of submilliwatt power to thermal energy and the resulting liquid evaporation and condensation has been used to drive fluid flow along the path of the laser beam.

1.5 Research Overview and Dissertation Breakdown

Chapter 2 describes analytical work I have carried out to investigate fluidically driven microscale assembly. Previous methods to model and quantify assembly techniques have largely focused on fluidic assembly driven by capillary interactions. Our approach to fluidically driven microscale assembly is fundamentally different, where fluid flow is used to push objects in an assembly chamber to target assembly locations, where objects are assembled based on a shape-matching affinity interaction. This assembly method involves the interaction between fluid flow and the subsequently generated fluid forces, which are used to drive assembly, with the motion of the object being assembled. Chapter 2 will discuss the analytical tools I have developed to investigate this interaction and the use of these tools to examine various kinds of assembly schemes. I will also discuss the parameters I have developed to quantify and compare the success of these assembly methods.

Chapter 3 continues with a description of experimental work I have carried out to tune interaction affinities in directed fluidic assembly. Current microscale assembly approaches are static in nature, with the final assembled structure being preprogrammed before the assembly process begins. As will be discussed in more detail in Chapter 3, this is due to the static affinities between assembling objects that

only lead to a unique final structure, limiting the robustness and versatility of these assembly methods as well as making them error prone. To overcome these limitations, I discuss a technique to tune the affinities between assembling objects by a local modification of flow environments through on-chip valving. By labeling specific locations on a target object as negative affinity regions (by a modification of the local flow field), an assembling object can then specifically be directed to other positive affinity regions. This capability is demonstrated through the use of a particular kind of polymer solution that undergoes a solution to gel transition on being heated, allowing a dynamic tuning of assembly affinities. In this chapter, I describe the implementation of dynamically tunable affinities and demonstrate reconfigurable assembly, the creation of irregularly shaped objects and error correction with this approach.

Chapter 4 and 5 continue my investigations into creating programmable systems and examine the use of optofluidics for reconfigurable microfluidics. Current channel-based microfluidic devices are fundamentally limited in that the flow control structures need to be designed, fabricated and placed on the microchip *a priori* and cannot be reconfigured. In Chapter 4, I present a dynamic, rapid, low power optofluidic approach to creating reconfigurable valves on a microfluidic device. This approach uses the polymer solution discussed above, along with a microfluidic chip with an absorbing substrate that converts optical energy from a milliwatt power laser beam to thermal energy. Reconfigurable valving is demonstrated with this approach and the temporal and leakage characteristics of the valve are quantified in detail.

Chapter 5 demonstrates a first step towards large scale microchannel reconfiguration. The approach for reconfiguration is similar to that described above. However, rather than laser light, spatial light modulation is used to illuminate the chip with optical patterns and thus dynamically tune thermal fields present on the chip. Using this approach, it is possible to create, reconfigure and remove solid regions on the chip that act as channel walls and thus reconfigure flow pathways and build morphable channel structures. In addition to characterizing this effect, it is also applied as a biological analysis tool. Dynamic trapping of nanoparticles and biomolecules is demonstrated through a suppression of particle diffusion.

Finally, Chapter 6 concludes my thesis with a summary of the outcome of my work. I also provide potential future directions of this work, describing both the work that has already begun in my research group through my efforts as well as other possible directions this work can take.

REFERENCES

1. Whitesides, G. M. & Boncheva, M. Beyond molecules: Self-assembly of mesoscopic and macroscopic components. *PNAS* **99** (2002).

2. Philp, D. & Stoddart, J. F. Self-assembly in natural and unnatural systems. *Angew. Chem.* **35** (1996).

3. Whitesides, G. M. & Grzybowski, B. Self-Assembly at all scales. *Science* **295** (2002).

4. Winfree, E., Liu, F. R., Wenzler, L. A. & Seeman, N. C. Design and self-assembly of two-dimensional DNA crystals. *Nature* **394** (1998).

5. Olenyuk, B., Whiteford, J. A., Fechtenkötter, A. & Stang, P. J. Self-assembly of nanoscale cuboctahedra by coordination chemistry. *Nature* **398** (1999).

6. Rothemund, P. W. K. Folding DNA to create nanoscale shapes and patterns. *Nature* **440** (2006).

7. Yeh, H. J. & Smith, J. S. Fluidic Self-Assembly for the integration of GaAs Light-Emitting Diodes on Si substrates. *IEEE Photon. Technol. Lett.* **6** (1994).

8. Zheng, W. & Jacobs, H. O. Shape-and-solder-directed self-assembly to package semiconductor device segments. *Appl. Phys. Lett.* **85** (2004).

9. Jackman, R. J., Brittain, S. T., Adams, A., Prentiss, M. G. & Whitesides, G. M. Design and fabrication of topologically complex, three-dimensional microstructures. *Science* **280** (1998).

10. Cohn, M. B. *et al.* in *Proc. SPIE Micromachining and Microfabrication, Conference on Micromachining and Microfabrication Process Technology IV* 2-16 (SPIE, Santa Clara, CA, USA, 1998).

11. Stone, H. A., Stroock, A. D. & Ajdari, A. Engineering flows in small devices: Microfluidics toward a lab-on-a-chip. *Annual Review of Fluid Mechanics* **36** (2004).

12. Duffy, D. C., McDonald, J. C., Schueller, O. J. A. & Whitesides, G. M. Rapid prototyping of microfluidic systems in poly(dimethylsiloxane). *Analytical Chemistry* **70** (1998).

13. Thorsen, T., Maerkl, S. J. & Quake, S. R. Microfluidic large-scale integration. *Science* **298** (2002).

14. Pollack, M. G., Shenderov, A. D. & Fair, R. B. Electrowetting-based actuation of droplets for integrated microfluidics. *Lab Chip* **2** (2002).

15. Miller, E. M. & Wheeler, A. R. A digital microfluidic approach to homogeneous enzyme assays. *Analytical Chemistry* **80** (2008).

16. Teh, S. Y., Lin, R., Hung, L. H. & Lee, A. P. Droplet microfluidics. *Lab on a Chip* **8** (2008).

17. Psaltis, D., Quake, S. R. & Yang, C. H. Developing optofluidic technology through the fusion of microfluidics and optics. *Nature* **442** (2006).

18. Monat, C., Domachuk, P. & Eggleton, B. J. Integrated optofluidics: A new river of light. *Nature Photonics* **1** (2007).

19. Casner, A. & Delville, J. P. Laser-induced hydrodynamic instability of fluid interfaces. *Physical Review Letters* **90** (2003).

20. MacDonald, M. P., Spalding, G. C. & Dholakia, K. Microfluidic sorting in an optical lattice. *Nature* **426** (2003).

21. Chiou, P. Y., Ohta, A. T. & Wu, M. C. Massively parallel manipulation of single cells and microparticles using optical images. *Nature* **436** (2005).

22. Liu, G. L., Kim, J., Lu, Y. & Lee, L. P. Optofluidic control using photothermal nanoparticles. *Nat. Mater.* **5** (2006).

23. Ohta, A. T., Jamshidi, A., Valley, J. K., Hsu, H. Y. & Wu, M. C. Optically actuated thermocapillary movement of gas bubbles on an absorbing substrate. *Appl. Phys. Lett.* **91** (2007).

24. Erickson, D. & Krishnan, M. in *Lab-on-Chip Technology: Fabrication and Microfluidics* (eds A. Rasooly & K. Herold) (Horizon Scientific Press, 2008).

25. Kock, M., Evans, A. & Brunnschweiler, A. *Microfluidic Technology and Applications*. (Research Studies Press, 2000).

26. Cho, S. K., Moon, H. J. & Kim, C. J. Creating, transporting, cutting, and merging liquid droplets by electrowetting-based actuation for digital microfluidic circuits. *J. Microelectromech. Syst.* **12** (2003).

27. McDonald, J. C. *et al.* Fabrication of microfluidic systems in poly(dimethylsiloxane). *Electrophoresis* **21** (2000).

28. Quake, S. R. & Scherer, A. From micro- to nanofabrication with soft materials. *Science* **290** (2000).

29. Unger, M. A., Chou, H. P., Thorsen, T., Scherer, A. & Quake, S. R. Monolithic microfabricated valves and pumps by multilayer soft lithography. *Science* **288** (2000).

30. Laser, D. J. & Santiago, J. G. A review of micropumps. *J. Micromech. Microeng.* **14** (2004).

31. Biddiss, E., Erickson, D. & Li, D. Q. Heterogeneous surface charge enhanced micromixing for electrokinetic flows. *Analytical Chemistry* **76** (2004).

32. Stroock, A. D. *et al.* Chaotic mixer for microchannels. *Science* **295** (2002).

33. Darhuber, A. A., Valentino, J. P., Troian, S. M. & Wagner, S. Thermocapillary actuation of droplets on chemically patterned surfaces by programmable microheater arrays. *J. Microelectromech. Syst.* **12** (2003).

34. Israelachvili, J. N. Measurement of the viscosity of liquids in very thin-films. *J. Colloid Interface Sci.* **110** (1986).

35. Hunter, R. J. *Zeta potential in colloid science: principles and applications*. (Academic Press, 1981).

36. Lyklema, J. *Fundamentals of Interface and Colloid Science, Volume 1: Fundamentals*. Vol. 1 (Academic Press, 1991).

37. Lyklema, J. *Fundamentals of Interface and Colloid Science, Volume 2: Solid Liquid Interfaces*. (Academic Press, 1995).

38. Li, D. Q. *Electrokinetics in Microfluidics*. (Elsevier Academic, 2004).

39. Erickson, D., Sinton, D. & Li, D. Q. Joule heating and heat transfer in poly(dimethylsiloxane) microfluidic systems. *Lab Chip* **3** (2003).

40. Erickson, D., Yang, C. H. & Psaltis, D. Optofluidics emerges from the laboratory. *Photonics Spectra* **42** (2008).

41. Ashkin, A. Acceleration and Trapping of Particles by Radiation Pressure. *Physical Review Letters* **24** (1970).

42. Ashkin, A., Dziedzic, J. M., Bjorkholm, J. E. & Chu, S. Observation of a Single-Beam Gradient Force Optical Trap for Dielectric Particles. *Optics Letters* **11** (1986).

43. Grier, D. G. A revolution in optical manipulation. *Nature* **424** (2003).

44. Wang, M. M. *et al.* Microfluidic sorting of mammalian cells by optical force switching. *Nature Biotechnology* **23** (2005).

45. Curtis, J. E., Koss, B. A. & Grier, D. G. Dynamic holographic optical tweezers. *Optics Communications* **207** (2002).

46. Sugiura, S. *et al.* On-demand microfluidic control by micropatterned light irradiation of a photoresponsive hydrogel sheet. *Lab on a Chip* **9** (2009).

47. Krishnan, M., Park, J. & Erickson, D. Opto-thermorheological flow manipulation *Optics Letters* **34** (2009).

48. Shirasaki, Y. *et al.* On-chip cell sorting system using laser-induced heating of a thermoreversible gelation polymer to control flow. *Analytical Chemistry* **78** (2006).

49. Krishnan, M. & Erickson, D. in *Handbook of Optofluidics* (eds H. Schmidt & A. Hawkins) (Wiley, 2009).

50. Landau, L. D. & Lifshitz, E. M. *Electrodynamics of continuous media*. (Pergamon Press, 1960).

51. Wunenburger, R., Casner, A. & Delville, J. P. Light-induced deformation and instability of a liquid interface. I. Statics. *Phys. Rev. E* **73** (2006).

52. Wunenburger, R., Casner, A. & Delville, J. P. Light-induced deformation and instability of a liquid interface. II. Dynamics. *Phys. Rev. E* **73** (2006).

53. Casner, A. & Delville, J. P. Laser-induced hydrodynamic instability of fluid interfaces. *Phys Rev Lett* **90** (2003).

54. Brasselet, E. & Delville, J. P. Liquid-core liquid-cladding optical fibers sustained by light radiation pressure: Electromagnetic model and geometrical analog. *Phys. Rev. A* **78** (2008).

55. Brasselet, E., Wunenburger, R. & Delville, J. P. Liquid optical fibers with a multistable core actuated by light radiation pressure. *Physical Review Letters* **101** (2008).

56. Baroud, C. N., de Saint Vincent, M. R. & Delville, J. P. An optical toolbox for total control of droplet microfluidics. *Lab Chip* **7** (2007).

57. Baroud, C. N., Delville, J. P., Gallaire, F. & Wunenburger, R. Thermocapillary valve for droplet production and sorting. *Phys. Rev. E* **75** (2007).

CHAPTER 2

INCREASED ROBUSTNESS FOR FLUIDIC SELF-ASSEMBLY*

2.1 Abstract

Self-assembly methods have been developed at the micro- and nano- scales to create functional structures from sub-elements stochastically dispersed in a fluid. Self-assembly paradigms have limitations in terms of achievable complexity of the final structure, ability to perform error correction and scalability. Fluidic self-assembly attempts to overcome these limitations by incorporating a controlled flow structure and/or complex geometric interactions to improve the assembly rate and the specificity of final positioning. Since the initial position and orientation of a sub-element in a stochastic system is indeterminate, the most robust of these schemes are those for which the dependence on the initial condition will be the weakest. In this paper we develop an analytical/numerical model for the fluid forces and torques on a two dimensional sub-element involved in a Fluidic Self-Assembly process and describe the translational and rotational motion of the element due to these forces. We use this model to determine optimal sub-element shapes and flow conditions that lead to successful assembly over the broadest range of initial conditions. We quantify the degree to which assembly has been successful by introducing two docking parameters

* Reprinted with permission from Krishnan, M., Tolley, M. T., Lipson, H. and Erickson, D., "Increased robustness for fluidic self-assembly", Physics of Fluids, **20** (7), 073304, 2008. Available online at http://pof.aip.org/.

that are descriptive of how close the final sub-element position is to the ideal case. Robust self-assembly schemes were developed for the assembly of different tile shapes. This approach to evaluate a self-assembly process based on final sub-element position can be applied to other Fluidic Self-Assembly techniques.

2.2 Introduction

As an alternative to traditional "top-down" fabrication techniques[1], self-assembly[2,3] is a "bottom-up" method whereby a target structure is constructed from a set of small scale sub-elements with as little external intervention as possible. The sub-elements represent the fundamental building blocks of the final device and can be manufactured or synthesized at any time prior to final assembly. Top down device fabrication approaches based on lithography are essentially two dimensional in nature, and require that the various components of a device be manufactured using compatible fabrication technologies. Self-assembly offers distinct advantages over these top down fabrication techniques in that they enable the fabrication of three dimensional structures[4] from non-uniform sub-elements. This could potentially enable designers to build devices comprising of complex arrays of different materials or functionalities which would be impossible to achieve using traditional microfabrication techniques[5]. These self-assembly techniques also offer potential advantages at the microscale over traditional pick and place methods including: spatial resolution (since very small sub-elements can be synthesized), higher assembly rates (due to increased parallelism), lower device costs (since the amount of infrastructure required can be lower) and fewer problems with undesired adhesion[6].

Various self-assembly paradigms exist that make use of inter-element affinities in scales ranging from the mesoscopic to the macroscopic[7]. These affinities include non-covalent attractions like van der Waals, hydrophobic and Coulomb interactions, as well as covalent interactions[3,8,9]. More recently, fluid based interactions have been studied as the driving mechanism for self-assembly that can be classified under Fluidic

Self-Assembly. Capillary interactions that are based on the minimization of free energies at interfacial areas have been used to carry out assembly of components at fluid interfaces as well as in suspension[10,11]. These interactions have been used to fabricate devices with micro-mirrors[12] and LEDs[13,14]. Fluidic Self-Assembly has also been applied to the assembly of patterned sub-elements on a substrate using shape matching, where a suspension of components is made to flow across a substrate having indentations complementary to the shape of the components, causing the components to fall into and subsequently bind to the indentations[15,16]. Finally, fluid forces have been coupled with other forces such as colloidal interactions[17], magnetic forces[18,19] and optical forces[20] to extend Fluidic Self-Assembly to a broader range of assembly applications.

The self-assembly methods described above are largely stochastic in nature and rely on large component numbers to carry out successful assembly and reduce errors. This approach has certain drawbacks. These techniques lend themselves well to the building of regular structures rather than irregular shapes which reduces the scope of applications for these methods. Additionally, as the complexity of the target structure increases, more distinct types of pieces are needed to carry out assembly, lowering the selectivity of inter component affinities and increasing the probability of error. Finally, since the affinity between two components is often shape dependent, the shape of the assembling components must be carefully designed for each new target structure, which makes these self-assembly procedures less robust and scalable.

We have recently developed a semi-directed deterministic assembly process, Directed Hierarchical Fluidic Self-Assembly (DHFSA), which attempts to address

these shortcomings[21,22]. In this method, the assembly of sub-elements takes place in a microfluidic chamber with directed fluid motion being the driving mechanism for the assembly. The chamber is lined with an array of ports along its sides through which fluid can flow into and out of the chamber. The motion of fluid exerts both a force and torque on an assembling component, resulting in a translational and an angular velocity that move it to the target location. Figure 2.1 is a schematic showing our concept of DHFSA. The assembling components shown here are two dimensional sub-elements (which we refer to as tiles herein), though assembly can be extended to three dimensions. The process begins with fluid flow into one of the substrate ports attracting a tile moving stochastically in the fluid towards it (Figure 2.1a). Once the tile attaches to the substrate, it can draw power from the substrate to activate on-board valves and direct fluid flow through internal channels in the tile (Figure 2.1b). This sink flow creates a local "attraction basin" along one of the tile faces, thus controlling the physical location where the next tile attaches (Figure 2.1b). The tiles join together through a reversible mechanical interaction. This process is continued to yield the desired target structure (Figures 2.1c and 2.1d). We have demonstrated the assembly and manipulation of tiles using DHFSA and have also carried out fabrication work to implement mechanical latches and electronic functionality on silicon tiles[22], as well as a valving mechanism based on on-board microvalves[21]. Using DHFSA, it is possible to implement error correction measures to reject incorrectly assembled components and replace them with new parts, which is difficult to do using traditional self-assembly techniques. Since the tiles are themselves lithographically patterned, it is possible to implement MEMS functionality, chemistry and microfluidics on the

assembling components. These robust, scalable properties allow us to apply DHFSA to the assembly of novel lab-on-chip devices, new materials and autonomously reconfigurable microsystems.

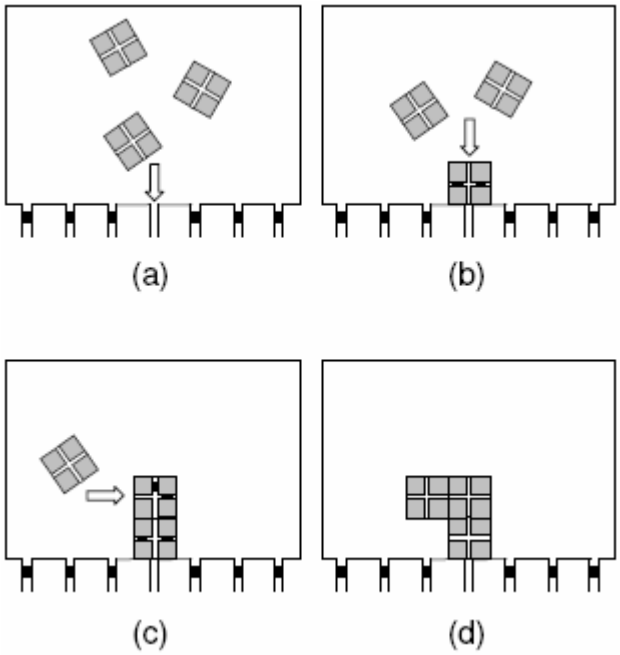

Figure 2.1. Schematic depicting Directed Hierarchical Fluidic Self-Assembly. (a) shows the attraction of a tile, moving stochastically in the fluid, to the substrate (b) – (c) depict the building of the target structure by controlling the attraction basin through on-board valving (d) shows the final assembled structure

In self-assembly methods (including DHFSA) the initial position and orientation of a sub-element involved in an assembly event is stochastic and therefore indeterminate. This complicates the overall process since the localized flow structure which guides the final assembly process (referred to herein as "docking") will be successful only over a narrow range of initial conditions. Sub-elements which enter the attraction basin surrounding the docking position outside of this range will either not assemble or assemble incorrectly resulting in a structural error. As such the most robust and

rapid assembly scheme is one in which a successful assembly event can be assured for the widest range of initial conditions.

In this paper we describe the development of an analytical model describing the motion of a solid tile in a high aspect ratio microchamber (Figure 2.2). Using numerical simulations this tile is subject to a range of different flow conditions and docking geometries with the goal of determining the conditions which maximize the range of initial positions and orientations that result in successful assembly. Previous work on modeling the driving force in a self-assembly process has been carried out for processes driven by magnetic forces[23-25], evaporation induced self-assembly[26] and surface tension or capillary effects[27-29]. However, the effect of modulating fluid motion as an active mechanism for self-assembly has not to our knowledge been previously studied. Authors[27-29] have studied the modeling of capillary effects and the design of suitable binding sites for their assembly procedure based on this model. Their approach to the characterization of successful docking and corresponding binding site design is based on free energy minimization (*i.e.* a good binding site design in one where the free energy of the system on docking has a unique minimum over the broadest range of initial tile orientations and positions). This approach works well for equilibrium driven self-assembly processes, but is difficult to apply to dynamic (i.e. non-equilibrium) processes like DHFSA. Instead, in order to quantitatively evaluate a successful assembly event in DHFSA, we describe two docking parameters that are based on the final position and orientation of the tile rather than the free energy of the system. This approach allows us to design successful assembly schemes for DHFSA, could also be extended to other non-

equilibrium methods of Fluidic Self-Assembly. Our fluidic system is a multiphase system, where the solid tiles in the chamber interact with liquid phase or the fluid in the chamber. Previous work on modeling the interaction between moving solid and liquid phases has been carried out, though mainly for shapes such as solid spheres[30-35], cylinders[36,37] or discs[38] in a fluidic medium where various approximations based on the shape can be applied and for fairly simple flow fields.

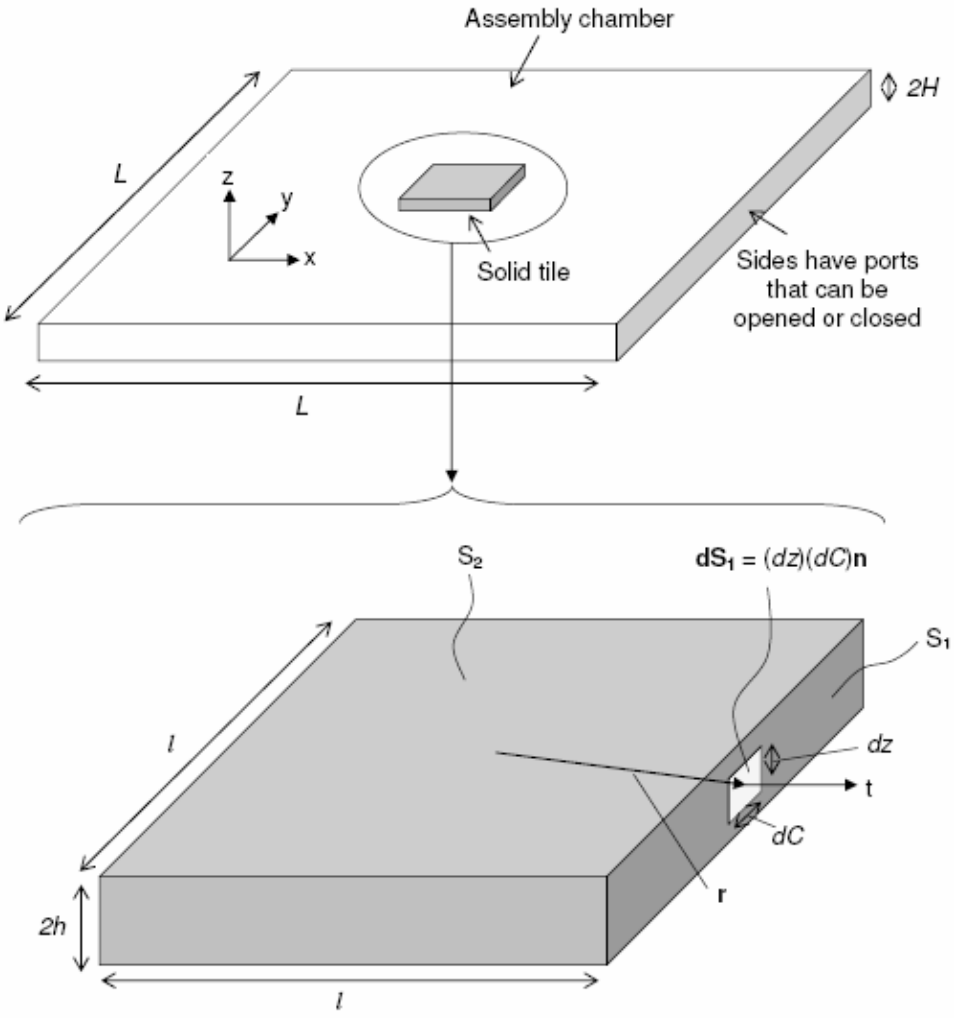

Figure 2.2. Schematic of assembly chamber with magnified view of tile showing area vectors.

In the following section we begin by describing our analytical model and our method for capturing all the relevant three dimensional fluid mechanics with a two dimensional solution. This approach significantly reduces computational time, increases mesh element quality and is therefore more amenable to future extension to a multiparticle system. In the next section the model is validated both through comparison with experimental results and full 3D simulations. In the final sections the model is applied to a series of different tile shapes, chamber geometries and flow conditions to determine the optimal set for assembly. We also introduce a set of "docking parameters" which serve to quantify successful assembly.

2.3 Mathematical Model

A solid body in a fluid medium experiences a translational force and a rotational torque as a result of the shear and pressure forces incident on it. Consider a solid tile in a chamber as shown in Figure 2.2. The x and y dimensions of the body are l, while the z dimension thickness of the body is $2h$, where $2h<<l$. The x and y dimensions of the chamber are ~ L while the z dimension is $2H$, where again $2H<<L$. The chamber has fluid inlet ports along its sides which can be opened to allow fluid to enter or leave the chamber or closed off to prevent fluid flow through them.

The fluid velocity **v** within the chamber is governed by the continuity and Navier-Stokes equations, which for a constant property Newtonian fluid of density, ρ, and viscosity, μ, are given by Equations 2.1 and 2.2 respectively.

$$\nabla \cdot \mathbf{v} = 0 \qquad (2.1)$$

$$\rho\left(\frac{\partial \mathbf{v}}{\partial t}+\mathbf{v}\cdot\nabla\mathbf{v}\right)=-\nabla p+\mu\nabla^2\mathbf{v} \qquad (2.2)$$

The linear, **a**, and angular, **α**, acceleration of the body within this flow field is calculated using the total stress tensor as

$$\mathbf{a}=\frac{\mathbf{F}}{m_{tile}}=\frac{\mathbf{F_p}+\mathbf{F_v}}{m_{tile}}=\frac{1}{m_{tile}}\left(-\oint_S p\mathbf{I}\cdot\mathbf{dS}+\oint_S \boldsymbol{\tau}\cdot\mathbf{dS}\right) \qquad (2.3a)$$

$$\boldsymbol{\alpha}=\frac{\mathbf{T}}{\mathbf{I}_{tile}}=\frac{\mathbf{T_p}+\mathbf{T_v}}{\mathbf{I}_{tile}}=\frac{1}{\mathbf{I}_{tile}}\left(-\oint_S \mathbf{r}\times p\mathbf{I}\cdot\mathbf{dS}+\oint_S \mathbf{r}\times\boldsymbol{\tau}\cdot\mathbf{dS}\right) \qquad (2.3b)$$

where **F**, **T** are the force and torque on the tile respectively, the subscript, **p**, refers to pressure force or torque and the subscript, **v**, refers to viscous force or torque, p is the pressure, **τ** is the viscous stress tensor, **I** is the identity tensor, **S** is the total surface area of the tile, **r** is a vector from the centre of the tile to the boundary, m_{tile} is the mass of the tile and $\mathbf{I}_{tile}$ is the moment of inertia tensor of the tile. The translational velocity, **u** and angular velocity **ω** of the body can be found from **a** and **α** using a first order scheme as

$$\mathbf{u}^{t+\Delta t}=\mathbf{u}^{t}+\mathbf{a}^{t}\Delta t \qquad (2.4a)$$

$$\boldsymbol{\omega}^{t+\Delta t}=\boldsymbol{\omega}^{t}+\boldsymbol{\alpha}^{t}\Delta t \qquad (2.4b)$$

The superscript, t, in the above equations refers to the time at which these quantities are evaluated and *Δt* is the timestep. By extension then, the new position, $\mathbf{x_{cg}}$ and orientation **θ** of the tile are found using a similar first order scheme as

$$\mathbf{x}_{cg}^{t+\Delta t}=\mathbf{x}_{cg}^{t+\Delta t}+\mathbf{u}^{t+\Delta t}\Delta t \qquad (2.5a)$$

$$\boldsymbol{\theta}_{cg}^{t+\Delta t}=\boldsymbol{\theta}_{cg}^{t+\Delta t}+\mathbf{u}^{t+\Delta t}\Delta t \qquad (2.5b)$$

With the above set of equations, the motion of the tile in a moving fluid is determined as follows. At a given time step, the flow field in the chamber is solved using Equation 2.1 and 2.2 and the resulting linear and angular acceleration of the tile are calculated by integrating the total stress tensor over the tile surface via Equation 2.3. The spatial and angular position of the tile is then updated using Equations 2.4 and 2.5. With the updated tile position the mesh surrounding the tile is updated and the process repeated until the tile reaches the target assembly site.

For the purpose of these simulations, we ignore the effect of gravity. As mentioned before, the chamber is such that $2H<<L$, hence we can ignore flow in the z direction (*i.e.* $v_z = 0$). Given the large aspect ratio it is reasonable to assume that the flow within the chamber is parabolic with respect to the z direction (Poiseuille flow) and that any obstacles in the path of the flow will deflect it but not change this fundamental shape. There is flow above and below the tile; however we can assume that this does not affect the flow along the sides of the tile, and that the parabolic flow assumption is valid here.

For this system, the variation of flow with the z direction can be described as

$$v_x = v_x'\left(1-\frac{z^2}{H^2}\right)$$
$$v_y = v_y'\left(1-\frac{z^2}{H^2}\right) \qquad (2.6)$$

where v_x' and v_y' are the peak velocities of the parabolic flow at the z = 0 midplane. Since $v_z' = 0$, the z momentum equation reduces to $\partial p/\partial z = 0$ and hence pressure does not vary with z.

With the above assumptions we can revise the x momentum equation by substituting Equation 2.6 into Equation 2.2 such that

$$\rho\left[\left(\frac{\partial v_x'}{\partial t}\left(1-\frac{z^2}{H^2}\right)\right)+\left(v_x'\frac{\partial v_x'}{\partial x}+v_y'\frac{\partial v_x'}{\partial y}\right)\left(1-\frac{z^2}{H^2}\right)^2\right]=$$

$$-\frac{\partial p}{\partial x}+\mu\left(\frac{\partial^2 v_x'}{\partial x^2}+\frac{\partial^2 v_x'}{\partial y^2}\right)\left(1-\frac{z^2}{H^2}\right)-2\mu\frac{v_x'}{H^2} \qquad (2.7)$$

which at z = 0 reduces to

$$\rho\left(\frac{\partial v_x'}{\partial t}+v_x'\frac{\partial v_x'}{\partial x}+v_y'\frac{\partial v_x'}{\partial y}\right)=-\frac{\partial p}{\partial x}+\mu\left(\frac{\partial^2 v_x'}{\partial x^2}+\frac{\partial^2 v_x'}{\partial y^2}\right)-2\mu\frac{v_x'}{H^2} \qquad (2.8a)$$

Similarly the y momentum equation can be written as

$$\rho\left(\frac{\partial v_y'}{\partial t}+v_x'\frac{\partial v_y'}{\partial x}+v_y'\frac{\partial v_y'}{\partial y}\right)=-\frac{\partial p}{\partial y}+\mu\left(\frac{\partial^2 v_y'}{\partial x^2}+\frac{\partial^2 v_y'}{\partial y^2}\right)-2\mu\frac{v_y'}{H^2} \qquad (2.8b)$$

Equations 2.8a and 2.8b represent the modified momentum equations that describe the flow in the midplane of the chamber. The flow structure specified by these equations is essentially two dimensional in nature, although the flow varies in all three dimensions. Solving for the full three dimensional Navier-Stokes equations described by Equation 2.2 is computationally expensive, especially since our process of simulation requires the mesh to be updated at each time step as the tile moves through the fluid. Equation 2.8 on the other hand, describes our system in two dimensions, while capturing the relevant three dimensional effects and reducing computational time in the process. The approach used to derive the above equations is similar to that

used in classical lubrication theory[39] and in the modeling of flow in a Hele Shaw cell[40].

Subject to the assumptions outlined above, it can be shown that the total linear force on the tile, **F**, comprises of the summation of the pressure and shear forces acting on its sides (surface $\mathbf{S_1}$), $\mathbf{F_{p,S_1}}$ and $\mathbf{F_{v,S_1}}$ respectively, and the shear forces on the upper and lower faces (surface $\mathbf{S_2}$), $\mathbf{F_{v,S_2}}$, resulting from the flow over and under the tile. Figure 2.2 shows the tile and its surfaces in detail. There is no pressure force on surface $\mathbf{S_2}$ since the pressure is invariant in the z direction. The torque on the tile can be expressed similarly, such that

$$\mathbf{F} = \mathbf{F}_{\mathbf{p},\mathbf{S}_1} + \mathbf{F}_{\mathbf{v},\mathbf{S}_1} + \mathbf{F}_{\mathbf{v},\mathbf{S}_2} \qquad (2.9a)$$

$$\mathbf{T} = \mathbf{T}_{\mathbf{p},\mathbf{S}_1} + \mathbf{T}_{\mathbf{v},\mathbf{S}_1} + \mathbf{T}_{\mathbf{v},\mathbf{S}_2} \qquad (2.9b)$$

The pressure force, $\mathbf{F_{p,S_1}}$ is given by the integral of the pressure about the circumference of the tile via Equation 2.10a

$$\mathbf{F}_{\mathbf{p},\mathbf{S}_1} = -\oint_{S_1} p(x,y)\mathbf{dS_1} = -\oint_{C} p(x,y)\mathbf{n}\,dC\int_{-h}^{h} dz = -2h\oint_{C} p(x,y)\mathbf{n}\,dC \qquad (2.10a)$$

where S_1 is the surface area along the sides of the tile, $\mathbf{dS_1}$ is an area vector element on the side of the tile, $|\mathbf{dS_1}| = (dz)(dC)$ where dC is a length element along the circumference of the tile, dz is a length element along the z axis, **n** is the normal along $\mathbf{dS_1}$ (Figure 2.2) and p(x,y) is the x-y pressure field. Similarly, the torque due to pressure, $\mathbf{T_{p,S_1}}$ on the sides of the tile is given by

$$\mathbf{T}_{\mathbf{p},\mathbf{S}_1} = -\oint_{S_1} \mathbf{r}\times p(x,y)\mathbf{dS_1} = -\oint_{C} \mathbf{r}\times p(x,y)\mathbf{n}\,dC\int_{-h}^{h} dz = -2h\oint_{C} \mathbf{r}\times p(x,y)\mathbf{n}\,dC \qquad (2.10b)$$

The viscous force, $\mathbf{F}_{\mathbf{v},\mathbf{S_1}}$ on the sides of the tile is given by

$$\mathbf{F}_{\mathbf{v},\mathbf{S}_1} = \oint_{S_1} \boldsymbol{\tau} \cdot \mathbf{dS}_1 = \oint_{S_1} \mu\left(\nabla \mathbf{v} + \nabla \mathbf{v}^T\right) \cdot \mathbf{n} \left|\mathbf{dS}_1\right| \qquad (2.11a)$$

Substituting Equation 2.6 in the above equation, we have

$$\mathbf{F}_{\mathbf{v},\mathbf{S}_1} = \mu \oint_{S_1} \left(\left(\nabla \mathbf{v}' + \nabla \mathbf{v}'^T\right) \cdot \mathbf{n}\right)\left(1 - \frac{z^2}{H^2}\right)\left|\mathbf{dS}_1\right| =$$

$$\mu \oint_C \left(\left(\nabla \mathbf{v}' + \nabla \mathbf{v}'^T\right) \cdot \mathbf{n}\right) dC \int_{-h}^{h} \left(1 - \frac{z^2}{H^2}\right) dz = \beta\left(\mu \oint_C \left(\left(\nabla \mathbf{v}' + \nabla \mathbf{v}'^T\right) \cdot \mathbf{n}\right) dC\right)$$

(2.11b)

where

$$\beta = \int_{-h}^{h} \left(1 - \frac{z^2}{H^2}\right) dz \qquad (2.11c)$$

For instance, for a 30μm tile (h = 15μm) in a 50μm chamber (H = 25μm), β = 26.4μm.

Similarly, the viscous torque, $\mathbf{T}_{\mathbf{v},\mathbf{S_1}}$ on the sides of the tile is given by

$$\mathbf{T}_{\mathbf{v},\mathbf{S}_1} = \beta\left(\mu \oint_C \mathbf{r} \times \left(\left(\nabla \mathbf{v}' + \nabla \mathbf{v}'^T\right) \cdot \mathbf{n}\right) dC\right) \qquad (2.11d)$$

As mentioned above, in addition to the force and torque on the sides of the tile, the flow above and below the tile exerts an additional shear force. We can separate the flow field above and below the tile into two independent components. Firstly, the flow field is affected by the fluid motion in the chamber which causes a flow velocity $\mathbf{v_f}$ above and below the tile. Secondly, it is affected by the motion of the tile itself, which cause a flow velocity $\mathbf{v_t}$ above and below the tile. Figure 2.3 is a schematic

showing these velocities. Let $b = H\text{-}h$ be the free fluid space above or below the tile in the chamber and z be the co-ordinate denoting distance from the tile surface to the chamber wall.

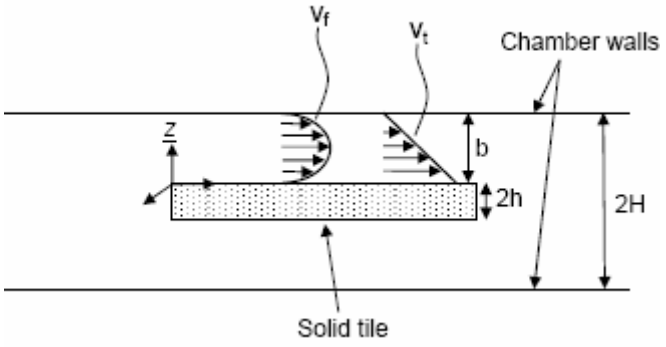

Figure 2.3. Schematic showing flow above the tile and the co-ordinate system used to describe the flow.

The $\mathbf{v_f}$ component of fluid velocity will assume a parabolic shape because it is due to the pressure difference between the upstream and downstream ends to the tile. Let ∇p_t be the pressure drop per unit length across the top of the tile. Then the fluid flow is given by

$$\mathbf{v_f} = -\frac{b^2}{2\mu}\left(\frac{z}{b} - \frac{z^2}{b^2}\right)\nabla p_t \qquad (2.12a)$$

Similarly the $\mathbf{v_t}$ component of fluid velocity can be expressed as a Couette flow profile, with

$$\mathbf{v_t} = \mathbf{u_{tile}}\left(1 - \frac{z}{b}\right) \qquad (2.12b)$$

where $\mathbf{u_{tile}}$ is the tile velocity. The net viscous force on the top and bottom tile due to $\mathbf{v_f}$, $\mathbf{F_{v,S_{2a}}}$ is given by

$$\begin{aligned}\mathbf{F}_{\mathbf{v,S_{2a}}} &= 2\mu\int_{S_2}\left.\frac{\partial \mathbf{v_f}}{\partial \underline{z}}\right|_{\underline{z}=0}\left|\mathbf{dS_2}\right| = -b^2\int_{S_2}\left.\frac{\partial}{\partial \underline{z}}\left(\frac{\underline{z}}{b}-\frac{\underline{z}^2}{b^2}\right)\right|_{\underline{z}=0}\nabla p_t\left|\mathbf{dS_2}\right| \\ &= -b\int_{S_2}\nabla p_t\left|\mathbf{dS_2}\right| \\ &= \left(\frac{b}{2h}\right)\left(-2h\oint_C p(x,y)\mathbf{n}dC\right) \\ &= \mathbf{F}_{\mathbf{p,S_1}}\left(\frac{b}{2h}\right)\end{aligned} \tag{2.13a}$$

where we have used the definition of $\mathbf{F_{p,S_1}}$ Equation 2.10a. We have used the divergence theorem here to convert the surface integral to an integral over the circumference of the tile.

Similarly, the net viscous force on the top and bottom tile due to $\mathbf{u_{tile}}$, $\mathbf{F_{v,S_{2b}}}$ is given by

$$\mathbf{F}_{\mathbf{v,S_{2b}}} = 2\mu\int_{S_2}\left.\frac{\partial \mathbf{v_t}}{\partial \underline{z}}\right|_{\underline{z}=0}\left|\mathbf{dS_2}\right| = -\frac{2\mu l^2\mathbf{u}_{\mathbf{tile}}}{b} \tag{2.13b}$$

To calculate the viscous torque on the top and bottom of the tile, we use a slightly different approach. We consider the torque to be due to the fluid velocity, $\mathbf{v_f}$ (similar to our previous approach) and due to the rotation of the tile $\boldsymbol{\omega_t}$. The torque on the tile due to $\mathbf{v_f}$, $\mathbf{T_{v,S_{2a}}}$ is given by

$$\begin{aligned}\mathbf{T}_{\mathbf{v,S_{2a}}} &= 2\mu\int_{S_2}\mathbf{r}\times\left.\frac{\partial \mathbf{v_f}}{\partial \underline{z}}\right|_{\underline{z}=0}\left|dS_2\right| = -b\int_{S_2}\mathbf{r}\times\nabla p_t\left|dS_2\right| \\ &= \mathbf{T}_{\mathbf{p,S_1}}\left(\frac{b}{2h}\right)\end{aligned} \tag{2.14a}$$

where $\mathbf{T_{p,S_1}}$ is defined in Equation 2.10b. Again, we have used the divergence theorem to convert the surface integral to an integral over the tile boundary.

The torque due to the rotation of the tile can be found by assuming the tile is a disc of radius R ($R = l/\sqrt{\pi}$). The velocity profile at a point on the tile with radius r is given by

$$\mathbf{v_t} = \boldsymbol{\omega}_{\mathbf{tile}} \times \mathbf{r}\left(1 - \frac{z}{b}\right) \qquad (2.14b)$$

The torque due to the rotation of the tile, $\mathbf{T_{v,S_{2b}}}$ is therefore given by

$$\begin{aligned}\mathbf{T}_{\mathbf{v,S_{2b}}} &= 2\mu \int_{S_2} \mathbf{r} \times \frac{\partial \mathbf{v_t}}{\partial z}\bigg|_{z=0} \left|\mathbf{dS_2}\right| = -\frac{2\mu}{b} \int_0^{2\pi} \int_0^R \mathbf{r} \times (\boldsymbol{\omega}_{\mathbf{tile}} \times \mathbf{r}) r dr d\theta \\ &= -\frac{4\mu\pi}{b} \int_0^R \mathbf{r} \times (\boldsymbol{\omega}_{\mathbf{tile}} \times \mathbf{r}) r dr \qquad (2.14c) \\ &= -\frac{\mu\pi\boldsymbol{\omega}_{\mathbf{tile}} R^4}{b}\end{aligned}$$

Finally, the net force and torque on the tile are given by

$$\mathbf{F} = -2h \oint_C p(x,y)\mathbf{n} dC + \mu\beta \oint_C \left(\left(\nabla \mathbf{v}' + \nabla \mathbf{v}'^{\mathbf{T}}\right) \cdot \mathbf{n}\right) dC + \mathbf{F}_{\mathbf{p,S_1}}\left(\frac{b}{2h}\right) - \frac{2\mu l^2 \mathbf{u}_{\mathbf{tile}}}{b} \qquad (2.15a)$$

$$\mathbf{T} = -2h \oint_C \mathbf{r} \times p(x,y)\mathbf{n} dC + \mu\beta \oint_C \mathbf{r} \times \left(\left(\nabla \mathbf{v}' + \nabla \mathbf{v}'^{T}\right) \cdot \mathbf{n}\right) dC + \mathbf{T}_{\mathbf{p,S_1}}\left(\frac{b}{2h}\right) - \frac{\mu\pi\boldsymbol{\omega}_{\mathbf{tile}} R^4}{b}$$

(2.15b)

In order to model our system in 2d simulations, we solve the modified Navier-Stokes equations, Equations 2.8a and 2.8b. Instead of using Equations 2.3a and 2.3b to update the tile position, we use Equations 2.15a and 2.15b. The rest of the simulation procedure remains the same as previously discussed. The forces on the tile have been summarized in Table 2.1.

2.4 Validation of 2D Model

In order to validate the above 2d model, we compared the results of our 2d simulations with 3d simulations, as well as with experimental results. For the numerical validation we carried out steady 2d and 3d simulations for different tile thicknesses, positions, inlet velocities and tile velocities and compared the pressure and viscous force exerted on the tile. The simulations were carried out using the commercial software FLUENT, with the modified x and y momentum equations given by Equation 2.8 and the modified force and torque terms on the tile given by Equation 2.15. In all cases grid independence studies were performed to ensure that mesh density was sufficient.

Table 2.1. Summary of forces and torque experienced by a solid tile in a fluidic chamber.

		Force	Torque
Tile sides	Due to pressure	$\mathbf{F}_{\mathbf{p},\mathbf{S}_1} = -2h\oint_C p(x,y)\mathbf{n}dC$	$\mathbf{T}_{\mathbf{p},\mathbf{S}_1} = -2h\oint_C \mathbf{r}\times p(x,y)\mathbf{n}dC$
	Due to viscosity	$\mathbf{F}_{\mathbf{v},\mathbf{S}_1} = \mu\beta\oint_C \left(\left(\nabla\mathbf{v}' + \nabla\mathbf{v}'^T\right)\cdot\mathbf{n}\right)dC$	$\mathbf{T}_{\mathbf{v},\mathbf{S}_1} = \mu\beta\oint_C \mathbf{r}\times\left(\left(\nabla\mathbf{v}' + \nabla\mathbf{v}'^T\right)\cdot\mathbf{n}\right)dC$
Top and bottom of tile	Due to fluid velocity	$\mathbf{F}_{\mathbf{v},\mathbf{S}_{2a}} = \mathbf{F}_{\mathbf{p},\mathbf{S}_1}\left(\frac{b}{2h}\right)$	$\mathbf{T}_{\mathbf{v},\mathbf{S}_{2a}} = \mathbf{T}_{\mathbf{p},\mathbf{S}_1}\left(\frac{b}{2h}\right)$
	Due to tile velocity	$\mathbf{F}_{\mathbf{v},\mathbf{S}_{2b}} = -\frac{2\mu l^2\mathbf{u}_{\mathbf{tile}}}{b}$	$\mathbf{T}_{\mathbf{v},\mathbf{S}_{2b}} = -\frac{\mu\pi\boldsymbol{\omega}_{\mathbf{tile}}R^4}{b}$

In these simulations tiles with l = 500µm and $2h$ = 30µm, 45µm, and 50µm were used in a chamber of dimension 3 mm X 5 mm X 50 µm. The fluid flow was such that the upper part of the chamber acted as an inlet, while the lower part of the

chamber acted as an outlet as shown in Figure 2.4a and 2.4c. Three cases were considered with midplane inlet velocities of V_{2d} = -1.5x10^{-2} m/s, -1.5x10^{-3} m/s and -1.5 x10^{-4}m/s, which corresponded to the peak velocities for the corresponding 3d simulations which had a parabolic inlet profile.

Simulations were carried out with no tile velocity, as well as an ascribed translational and rotational tile velocity. In the case of translational velocity, we ascribed a tile velocity $\mathbf{u}_{\mathbf{tile}}$ = 10^{-3} m/s in the y direction and positioned the tile as shown in Figure 2.4a (Scheme I), while for the rotating tile, we set the tile angular velocity $\omega_{\mathbf{tile}}$ = 10^{-2} rad/s **z**, and the position of the tile to that in Figure 2.4c (Scheme II). Figures 2.4b and 2.4d show the results of our simulations for the translational and rotational velocity cases, where we have compared the force and torque on the tile for the 2d and 3d simulations. The results of our 2d and 3d simulations were found to match within 1 - 7 % validating the two dimensional model.

The quantitative matching between our 2d and 3d simulations indicates that our model is physically accurate. A comparison of our 2d model with the experiments described in Tolley *et al*[22] also allowed us to obtain qualitative matching with experimental results. The assembling components were 500 μm X 500 μm X 30 μm silicon tiles with a passive latch on each side. Our simulations modeled the tile motion in the microchamber, and we compared the path of a tile brought down from the top of the chamber to the bottom in experiment and in simulation.

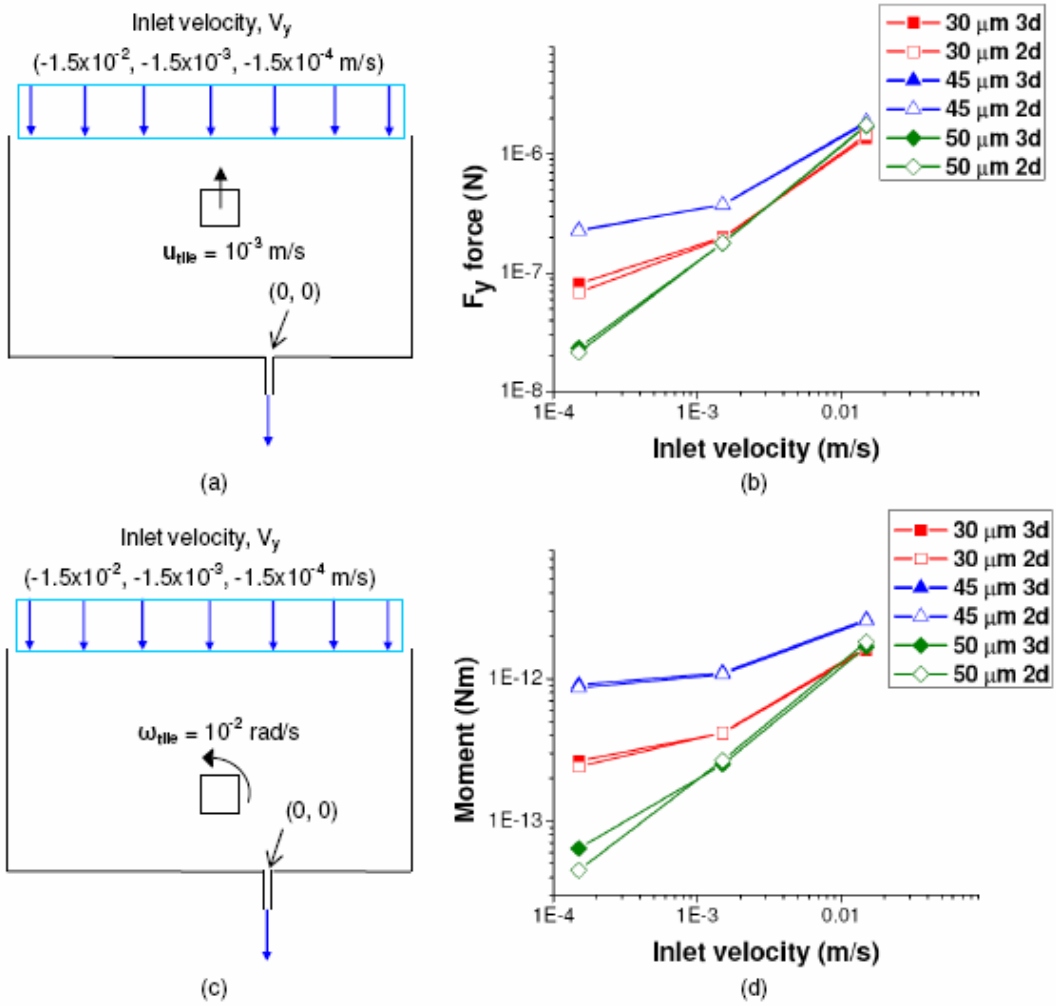

Figure 2.4. Comparison of two dimensional and three dimensional steady state simulations. (a) Scheme I: Tile position is (-250 µm, 2500 µm), and a translational velocity, $u_{tile} = 10^{-3}$ m/s was added to the tile. (b) shows the variation of Fy force with fluid velocity for Scheme I. (c) Scheme II: Tile position is (-250 µm, 1000 µm), and a rotational velocity, $\omega_t = 10^{-2}$ rad/s was added to the tile. (d) shows the variation of torque with fluid velocity for Scheme II.

Figure 2.5 shows the results of this comparison. The images show the passage of the tile from the top left part of the chamber to the bottom. The results from the experiments show a smaller field of view than the whole assembly chamber because of the magnification used while imaging the experiment. The arrows in the figure indicate regions where flow enters and leaves the chamber. Comparison of the path of

the tile in experiment and simulation visually indicates a rough qualitative matching between the two results. Given the quantitative agreement between the 2d and 3d numerical results and the qualitative matching between the 2d model and the experimental results, the model was considered physically accurate and used for the remaining simulations.

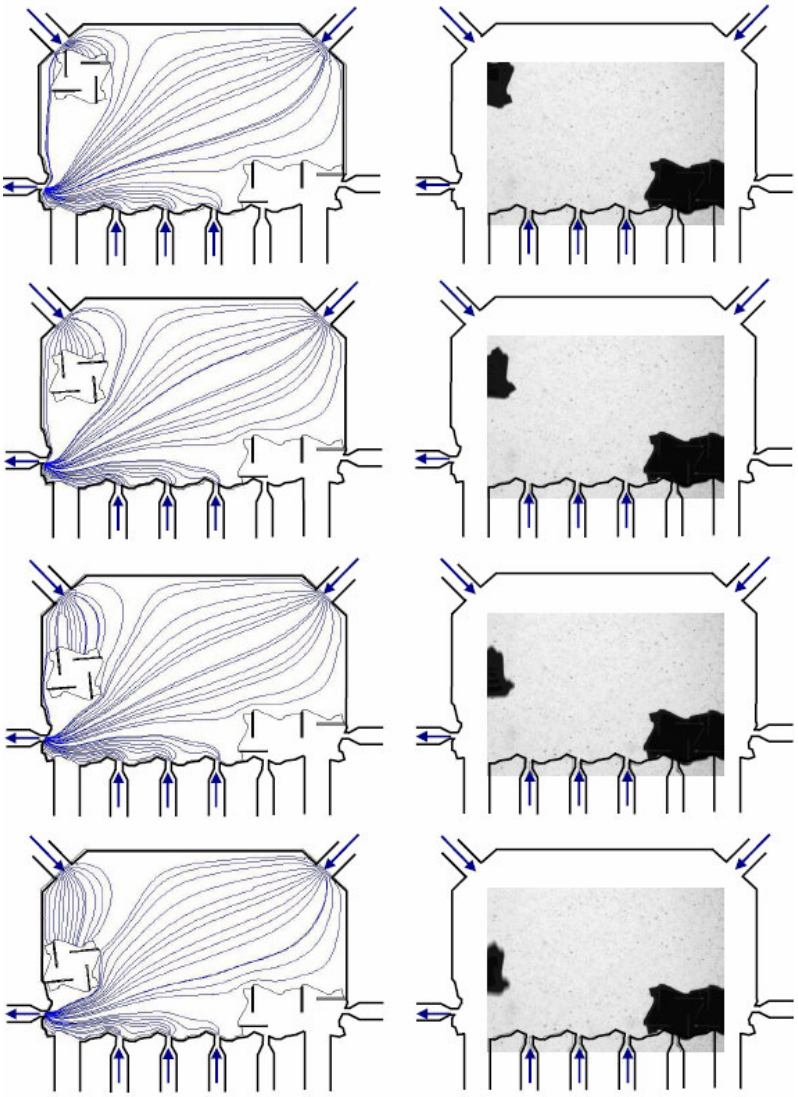

Figure 2.5. Comparison of 2d simulations and experiments. The left column shows tile movement through a microfluidic chamber in simulation and the right in experiment. The arrows indicate the fluid inlets and outlets in the system.

2.5 Results and Discussion

The goal of this paper was to use the model developed above to study the effect of tile shape, chamber geometry and flow conditions on the efficiency of the assembly process. As mentioned previously, in an actual system we assume that tile motion far away from the attraction point is stochastic and hence the initial position and orientation of a tile is not determinable prior to assembly. We would therefore like to design an assembly scheme where successful assembly events occur over the broadest range of initial tile conditions. In order to do this, we considered numerous different assembly schemes and quantitatively evaluated them over a range of initial tile conditions using two docking parameters, as described below.

2.5.1 Simulation conditions

Figure 2.5 shows the assembly chamber used in our experimental system. The experimental assembly chamber had inlets along the bottom and sides of the chamber, a single outlet port and a shape matched, angled substrate where assembly occurred. The chamber design and flow patterns examined in simulation were different from those used in experiments though the overall chamber and tile dimensions were similar. For our simulations, we consider the different tile shapes, assembly chamber designs and flow fields listed in Table 2.2. The simulation assembly schemes were chosen to study different aspects of the DHFSA process including the design of inlet and outlet ports, substrate design and tile shapes. The arrows in the assembly scheme figures indicate regions where flow enters and leaves the assembly chamber. We considered two tile shapes namely squares (Table 2.2, Schemes A1, A2, B1, B2, C1

and C2) and regular hexagons (Table 2.2, Schemes D1 and D2) with channels through them.

Table 2.2. Different assembly schemes used for simulations.

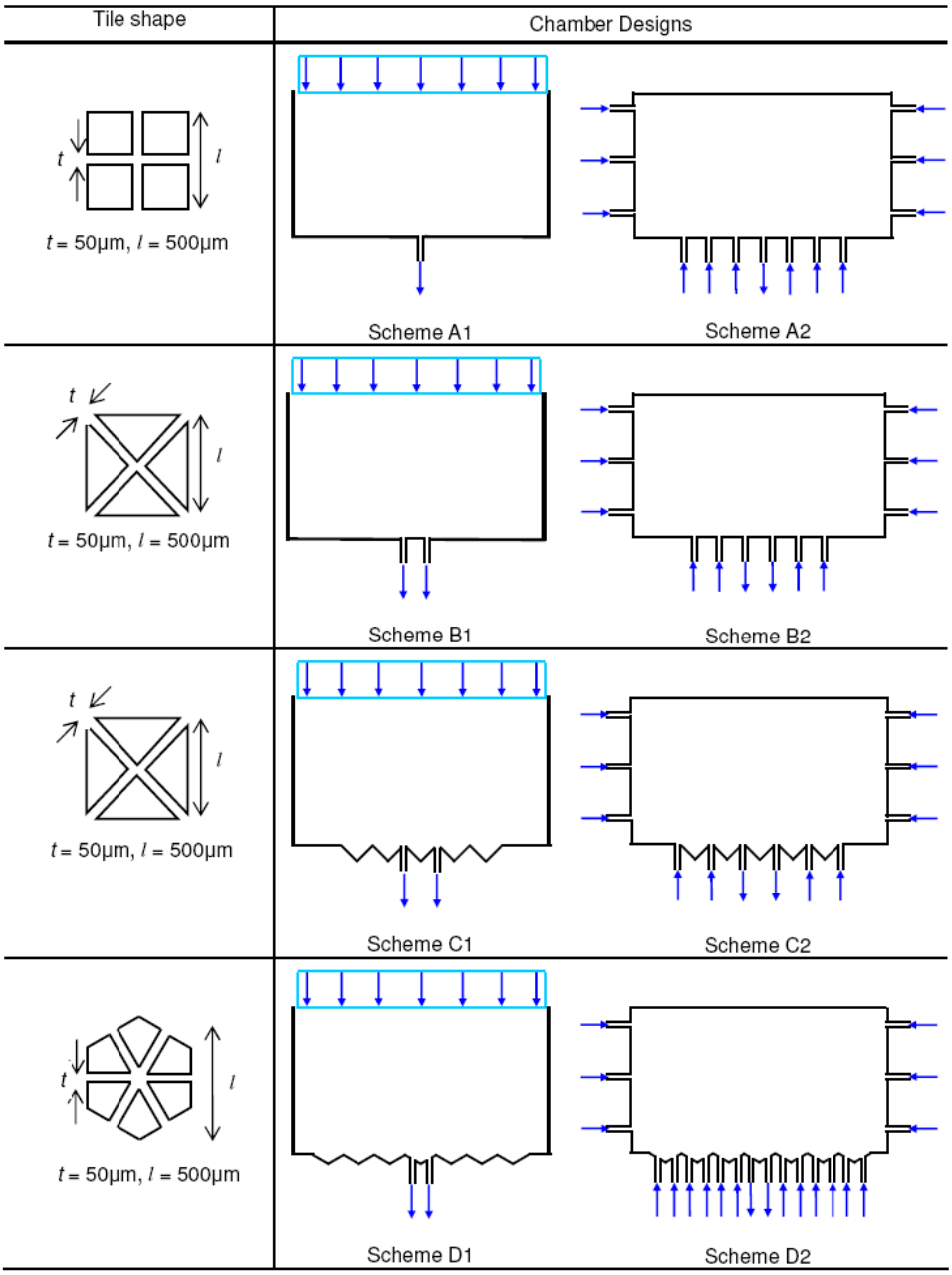

The pattern of channels in the tile is based on the outlet configuration in the chamber to allow for subsequent assembly around a tile that has previously been assembled on the substrate. The final position of the tile will depend on flow conditions such as the inlet flow pattern in the chamber and the configuration of the outlet. We looked at two different inlet flow configurations in our simulations. The first consisted of flow entering the chamber from a single large inlet directly above the flow outlet in the chamber (Table 2.2, Schemes A1, B1, C1 and D1). The second consisted of flow entering the chamber from numerous side inlets located orthogonal as well as in line with the main flow outlet (Table 2.2, Schemes A2, B2, C2 and D2). The reason for considering these two inlet schemes was to examine the effects of both a vertical inlet configuration and a horizontal inlet configuration. Additionally, we also looked at different outlet configurations namely a single port outlet on a flat substrate (Table 2.2, Schemes A1, A2), a dual port outlet on a flat substrate (Table 2.2, Schemes B1, B2) and a dual port outlet on an angled, shape-matched substrate (Table 2.2, Schemes C1, C2, D1 and D2).

In all the cases, the tile being assembled was a silicon tile in water, with length l ~ 500 μm and thickness $2h$ = 30 μm in a chamber of dimension $6l$ X $10l$ X $0.1l$ (3 mm X 5 mm X 50 μm). The peak inlet velocity into the large single inlet port used in Schemes A1, B1, C1 and D1 was $V = 1.5\text{x}10^{-3}$ m/s, while the inlet velocity used in Schemes A2, B2, C2 and D2 was $V = 1.5\text{x}10^{-2}$ m/s. These values were chosen to minimize the time needed to carry out the simulations, but the velocity did not affect the path of the tile since the fluid regime is Stokesian for the velocities we considered.

In order to evaluate the assembly schemes, we considered a range of initial tile conditions which were defined by two angles of rotation, φ and ψ (Figure 2.6). The angle φ refers to different tile positions spaced radially from the center of the chamber at angles of 0°, 15° and 30°. The angle ψ refers to initial tile orientation, given by the rotation of the tile about its own center of gravity. We looked at initial tile angles ranging from θ_{lower} = - 45° to θ_{upper} = 45° for square shaped tiles and from θ_{lower} = - 30° to θ_{upper} = 30° for hexagonal shaped tiles, which represent the range of unique tile orientations for these tile shapes.

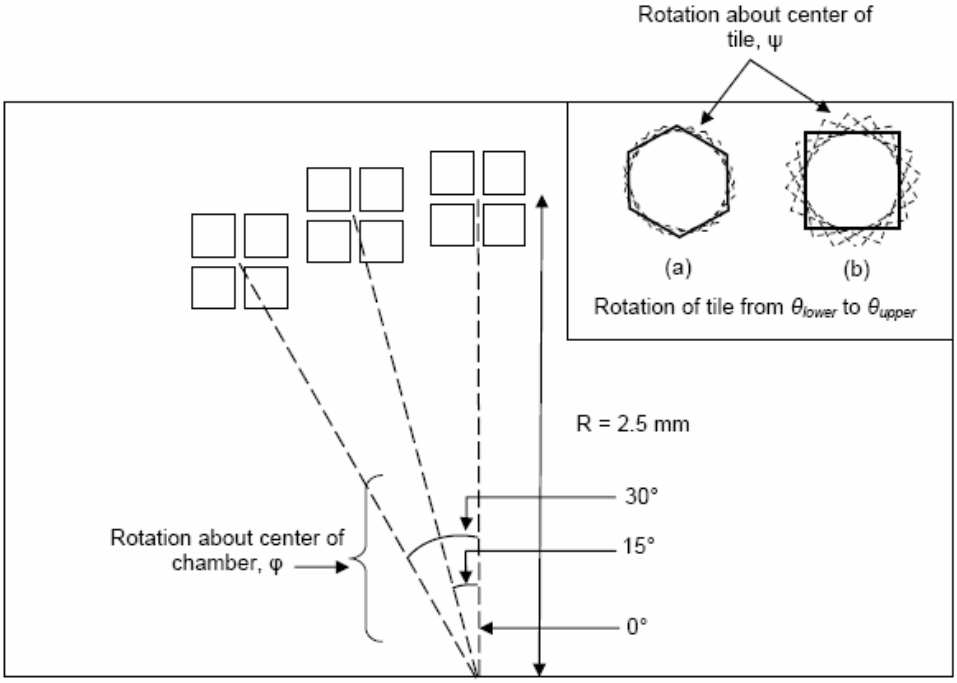

Figure 2.6. Schematic showing different tile positions and orientations used for simulations. The chamber and tile shapes are representative of all the shapes listed in Table 2.2.

A tile positioned directly above the outlet (φ = 0°) is expected to show the same assembly patterns for tile orientations symmetric with respect to the ψ = 0° tile

orientation. This is because the tile experiences a symmetric flow field at this position for all the assembly schemes studied. As the tile position moves away from the outlet though ($\varphi = 15°, 30°$), the tile experiences an asymmetric flow field with changing ψ, and hence assembly patterns are not expected to be symmetric with respect to the $\psi = 0°$ orientation. Therefore, although the target locations studied here were always along the centerline of the assembly chamber, the range of tile orientations and positions examined introduced asymmetric assembly patterns in our system, that could otherwise have been obtained by using target locations that were asymmetric with respect to the centerline of the chamber.

2.5.2 Docking Parameter

Successful assembly of a tile on the substrate requires the orientation and position of the tile to match with the target substrate on assembly. In order to quantify the successful assembly of the tile, we have defined two docking parameters, $D_{x,y}$ which is the "Translational Docking Parameter" and D_θ which is the "Rotational Docking Parameter". The assembly schemes considered here deal with the fluidic aspect of assembly, and our simulations do not account for any shape matching or collisions that can occur at the time of assembly. The docking parameters are therefore evaluated when the tile first touches the substrate, after which shape matching and collisions would control the final assembly process. If x and y are the positions of the center of gravity of the tile at the time of assembly and θ is the orientation of the tile, then we define the docking parameters as

$$D_{x,y} = \frac{\sqrt{(x - x_o)^2 + (y - y_o)^2}}{l} \qquad (2.16a)$$

$$D_{\theta} = \frac{\left|\,|\theta| - \theta_o\,\right|}{\theta_{upper} - \theta_{lower}} \qquad (2.16b)$$

where x_0 and y_0 are the co-ordinates of the center of gravity of the tile at the intended assembly position, θ_0 is the final orientation of the tile at this position, and l is the tile dimension. The docking parameter $D_{x,y}$ represents the translation a tile needs to undergo in order for it to be seated at the correct target location while the docking parameter D_θ represents the rotation the tile needs to undergo for it to be correctly docked. $D_{x,y}$ has been non-dimensionalized with respect to the tile length l, while D_θ has been non-dimensionalized with respect to the maximum rotation a tile needs to undergo to return to its initial orientation(*i.e.* (θ_{upper} - θ_{lower})). This is dependent on the tile shape: for instance, for a square tile, this angle is 90°, for a hexagonal tile it is 60°, and for an irregularly shaped tile, it could be 360°.

In the limit of successful assembly, the final positions and orientations of the tile match that of the intended tile position and orientation (i.e. $x = x_0$, $y = y_0$ and $\theta = \theta_0$) and hence we have

$$\lim_{D_{x,y} \to D_{x_o, y_o}} D_{x,y} = \lim_{\substack{x \to x_o \\ y \to y_o}} \frac{\sqrt{(x - x_o)^2 + (y - y_o)^2}}{l} = 0 \qquad (2.17a)$$

$$\lim_{D_\theta \to D_{\theta_o}} D_\theta = \lim_{\theta \to \theta_o} \frac{\left|\,|\theta| - \theta_o\,\right|}{\theta_{upper} - \theta_{lower}} = 0 \qquad (2.17b)$$

For all other cases, $D_{x,y} > 0$ and $D_\theta > 0$, since $x \neq x_0$, $y \neq y_0$ and $\theta \neq \theta_0$. A theoretical upper bound can be obtained for $D_{x,y}$ and D_θ in the following manner. For $D_{x,y}$, the maximum value of the numerator is given by the maximum chamber dimension which is ~ L. Therefore $max(D_{x,y}) \sim L/l >> 0$. For D_θ, the maximum value of the numerator is $(\theta_{upper} - \theta_{lower})/2$, and hence $max(D_\theta) = 0.5$.

Figure 2.7 compares the final tile location of a successfully assembled tile with those of tiles assembled by two other schemes, Assembly A and Assembly B. From the figure we see that the tile location at the end of assembly B is closer to the tile location at successful assembly as compared to the tile in assembly A. As a result, the docking parameter values for the tile in assembly B are closer to zero in value than for the tile in assembly A. The docking parameters are thus a means by which to compare different assembly schemes, though the comparison must take place across different initial tile conditions rather than for a single case of assembly. A scheme which gives $D_{x,y} \sim 0$ and $D_\theta \sim 0$ for most initial tile positions is better than a scheme where $D_{x,y}$, $D_\theta >> 0$ for most cases of assembly. The docking parameters do not give us an absolute measure of successful assembly, and it is not possible to predict the range of docking parameter values that indicate successful assembly. This is because other factors such as final shape matching between tile and substrate and the nature of the collision occurring also have an effect on the final assembly process. Rather, the docking parameters serve as a means of comparing the probability of successful assembly occurring for different assembly schemes. To summarize, the lower the docking parameter values for a given assembly process across different initial tile conditions, the more likely it is that the process leads to successful assembly. The above docking

parameters were used to compare the different assembly procedures listed in Table 2.2 for various initial tile configurations as discussed below.

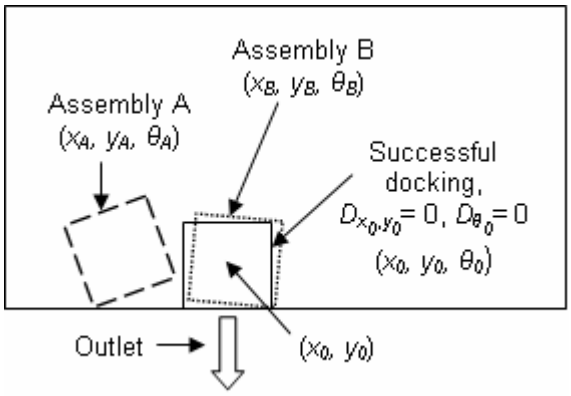

Figure 2.7. Schematic showing different tile positions and orientations (x, y, θ) at the end of assembly. Assembly B shows better tile docking compared to Assembly A, therefore $D_{xB,yB} \rightarrow D_{x0,y0}$ (= 0) and $D_{\theta B} \rightarrow D_{\theta 0}$ (= 0), while $D_{xA,yA}$, $D_{\theta A} > 0$.

The results of our simulations for the different assembly schemes considered are shown in Figures 2.8, 2.9, 2.10 and 2.11. The graphs in these figures show the variation of $D_{x,y}$ and D_θ with initial tile angles for the different assembly schemes. Figure 2.8 shows the results for assembly schemes A1 and A2, Figure 2.9 shows the results for schemes B1 and B2, Figure 2.10 shows the results for schemes C1 and C2, while Figure 2.11 shows the results for schemes D1 and D2. The variation in the two docking parameters is shown as a function of initial tile orientation ψ, for each of the three tile positions given by angle φ. The effect of the inlet flow patterns and the different outlet configurations on tile assembly is discussed in more detail in the following subsections.

2.5.3 Effect of inlet flow patterns

As mentioned previously, we considered two different inlet flow patterns as shown in Table 2.2, the first consisting of flow entering the chamber from a single top inlet directly above the flow outlet in the chamber (Schemes A1, B1, C1 and D1) and the second consisting of flow entering the chamber from numerous side inlets (Schemes A2, B2, C2 and D2). For a tile positioned directly above the outlet ($\varphi = 0°$), it is seen that the two docking parameters are symmetric about a 0° initial tile orientation ($\psi = 0°$) for all the assembly schemes, as expected.

More generally though, the schemes which had flow coming in from multiple side inlets (Schemes A2, B2, C2 and D2) were found to have significantly lower values of the Translational Docking Parameter $D_{x,y}$ (Figures 2.8c, 2.9c, 2.10c and 2.11c) for different tile positions, as compared to the other schemes where flow only entered the chamber from a single top inlet (Schemes A1, B1, C1 and D1) which had much higher values of $D_{x,y}$ (Figures 2.8a, 2.9a, 2.10a and 2.11a). Although the latter schemes showed low values of $D_{x,y}$ when the tile was positioned directly above the outlet, the $D_{x,y}$ values were found to dramatically increase with increasing φ, indicating deteriorating assembly as the tile moved its position away from the center of the chamber. For instance, the $D_{x,y}$ parameter had a maximum value of 0.25 for the A2 assembly scheme with the side inlets (Figure 2.8c), while it had a maximum value as high as 0.74 for the A1 assembly scheme with the single top inlet (Figure 2.8a). The effect of the side inlets was, however, more significant on the $D_{x,y}$ docking parameter than on the D_θ parameter. As such, no significant trends were observed for the Rotational Docking Parameter, D_θ for the different inlet flow configurations.

2.5.4 Effect of outlet flow patterns

Different outlet configurations were studied using the assembly schemes listed in Table 2.2, namely a single port outlet on a flat substrate (Schemes A1, A2), a dual port outlet on a flat substrate (Schemes B1, B2) and a dual port outlet on an angled, shape-matched substrate (Schemes C1, C2, D1 and D2). For a tile positioned directly above the outlet, the effect of a dual outlet port on a square tile was to cause a tile having an initial tile orientation close to 0° ($\psi \sim 0°$) to assemble on a substrate at a final angle approaching 0°. This effect is observed in the relatively flat profiles of the D_θ graphs for these schemes near initial tile angles of 0°, for $\varphi = 0°$ (Figures 2.9b, 2.9d, 2.10b, 2.10d). The effect of the single outlet port however was to cause a square tile having an initial tile orientation close to 45° ($\psi \sim 45°$) to assemble on a substrate at a final angle approaching 45°, which can be seen in the relatively flat profiles of the relevant D_θ graphs near initial tile angles of 45°, for $\varphi = 0°$ (Figures 2.8b and 2.8d). Hence it was found that a single port outlet configuration tended to rotate a square tile to a 45° final angle when possible, while a dual port outlet configuration tended to rotate a tile to a 0° final angle. This indicates that a single port outlet is useful for assembly of a square tile on an angled substrate, while a dual port outlet is useful for assembly on a flat substrate.

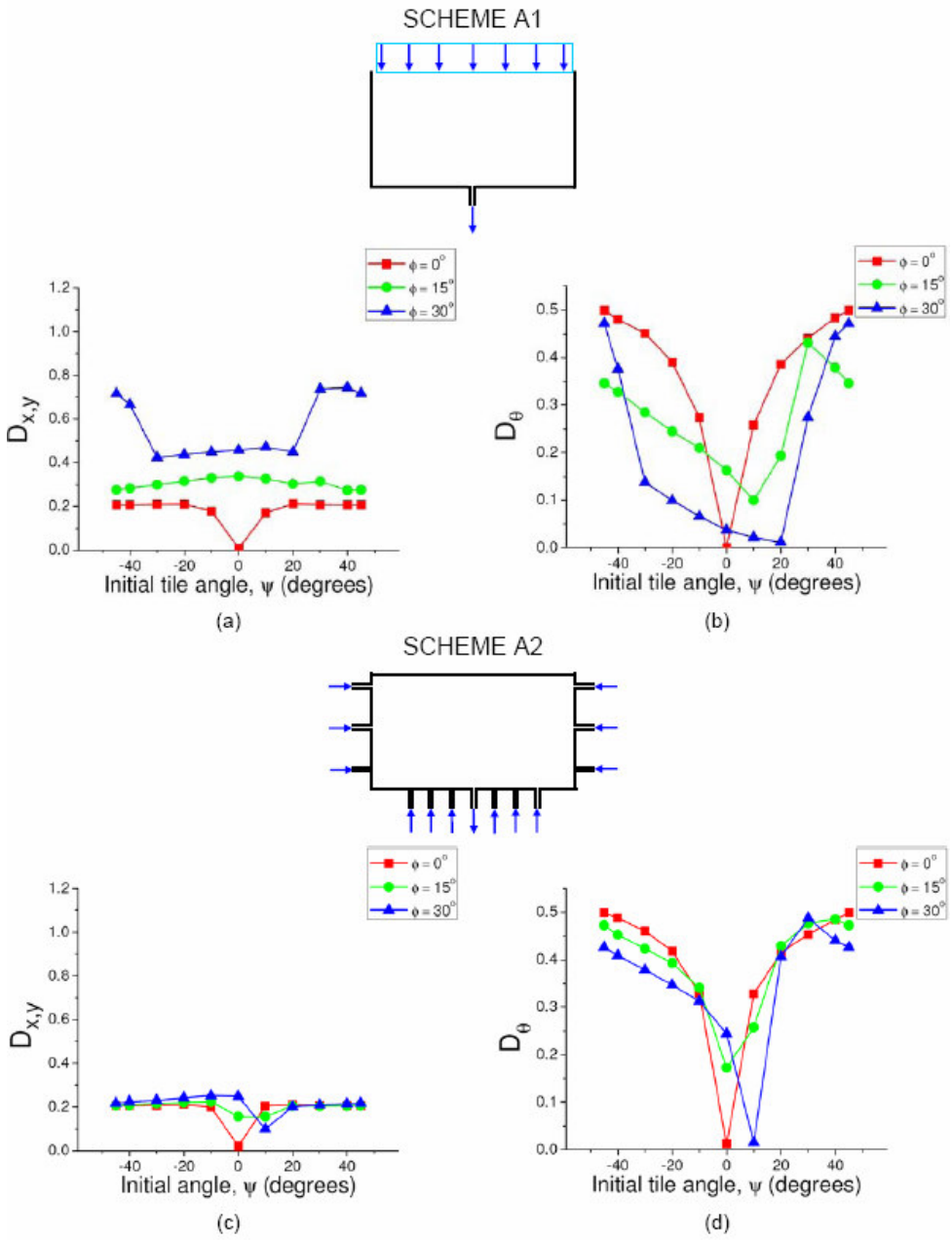

Figure 2.8. $D_{x,y}$ and D_{θ} for schemes A1 and A2. (a) – (b) Scheme A1 (c) – (d) Scheme A2

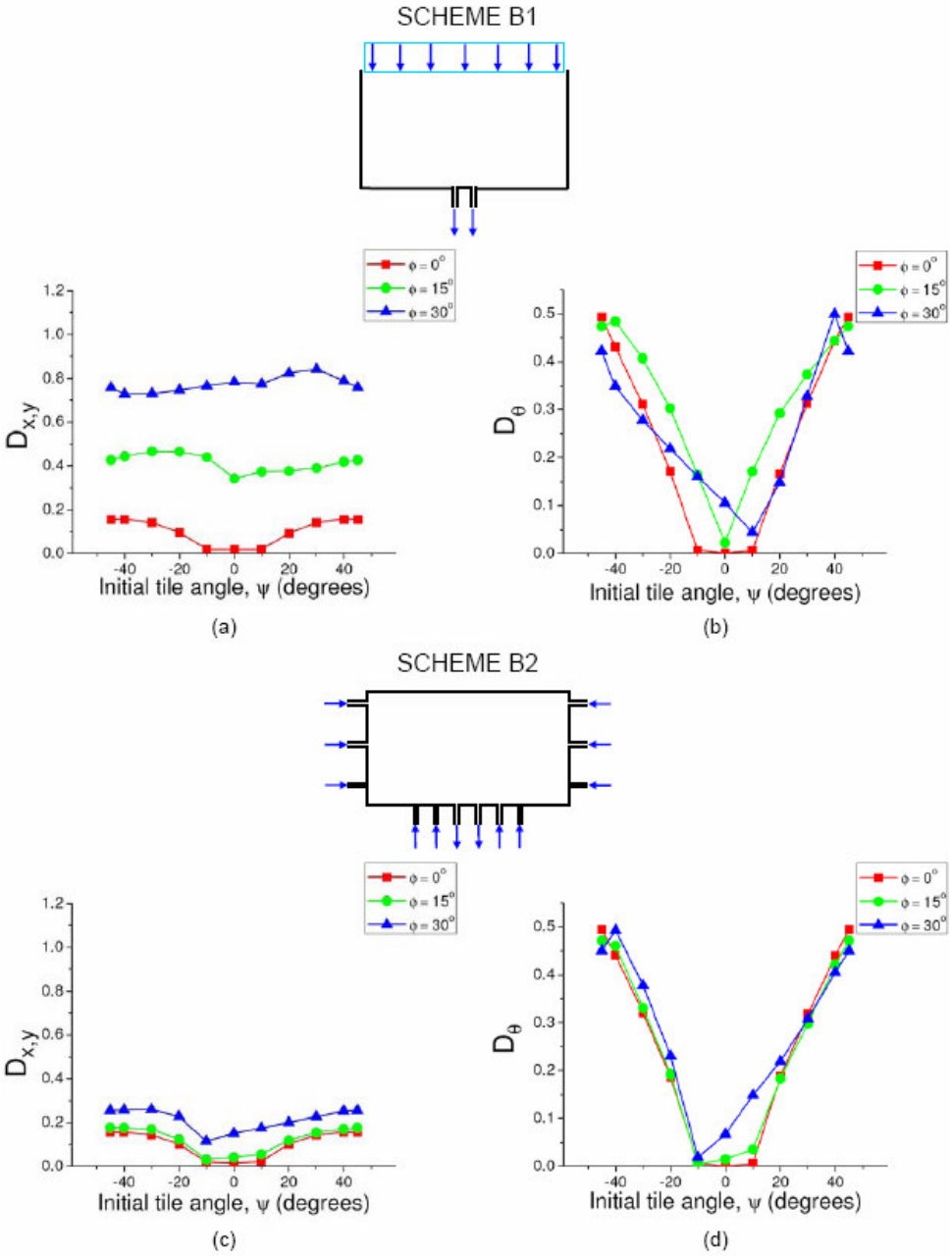

Figure 2.9. $D_{x,y}$ and D_θ for schemes B1 and B2. (a) – (b) Scheme B1 (c) – (d) Scheme B2

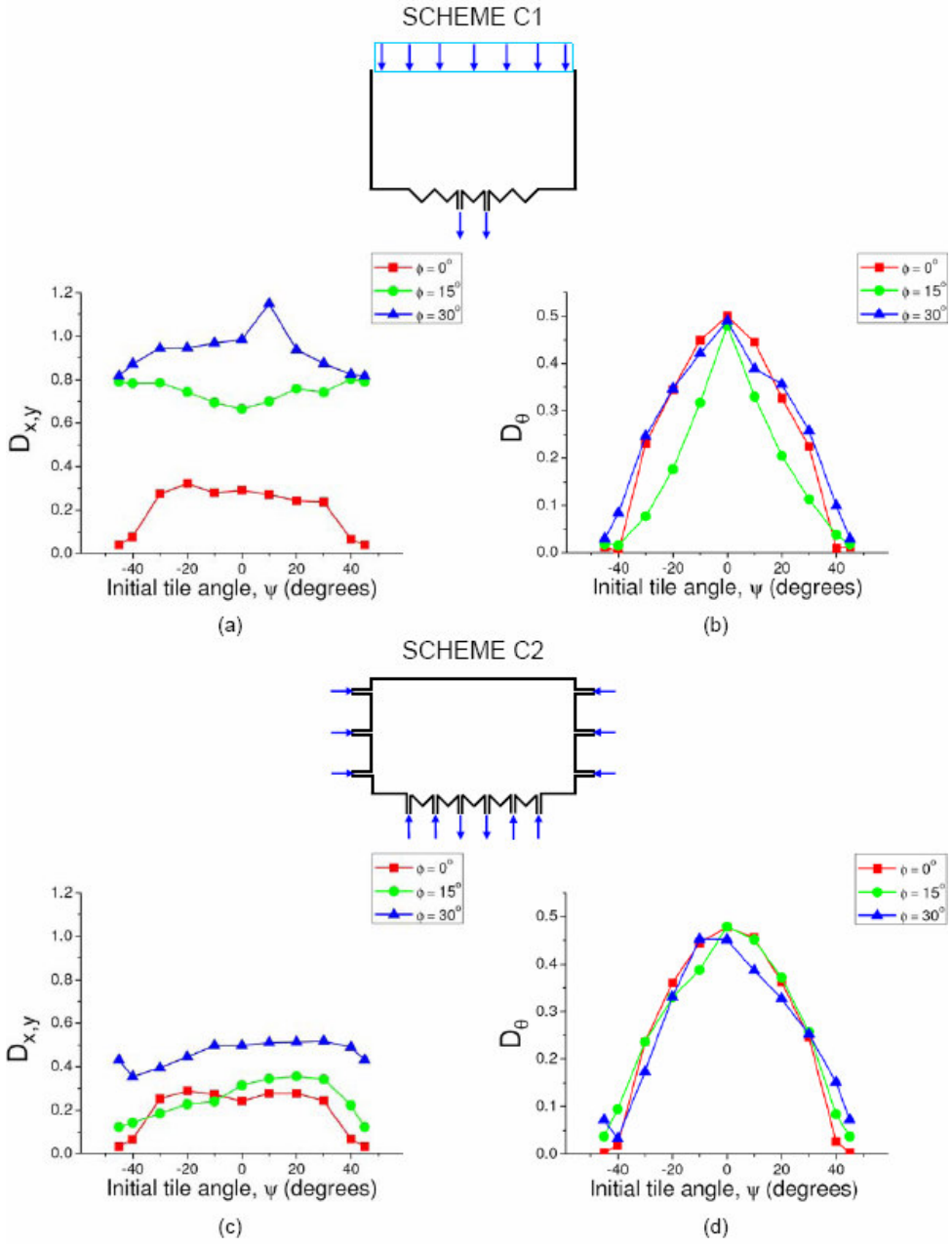

Figure 2.10. $D_{x,y}$ and D_θ for schemes C1 and C2. (a) – (b) Scheme C1 (c) – (d) Scheme C2

By contrast, for the hexagonal tile, the strongly linear profiles of the D_θ graphs indicates that the fluid flow does not significantly rotate the tile as it moves towards the outlet. Thus the tile orientation at assembly is similar to the initial orientation of

the tile (Figures 2.11b and 2.11d). Therefore the dual outlet configuration only has a significant effect on the rotation of a square tile, while it does not tend to change the orientation of a hexagonal tile.

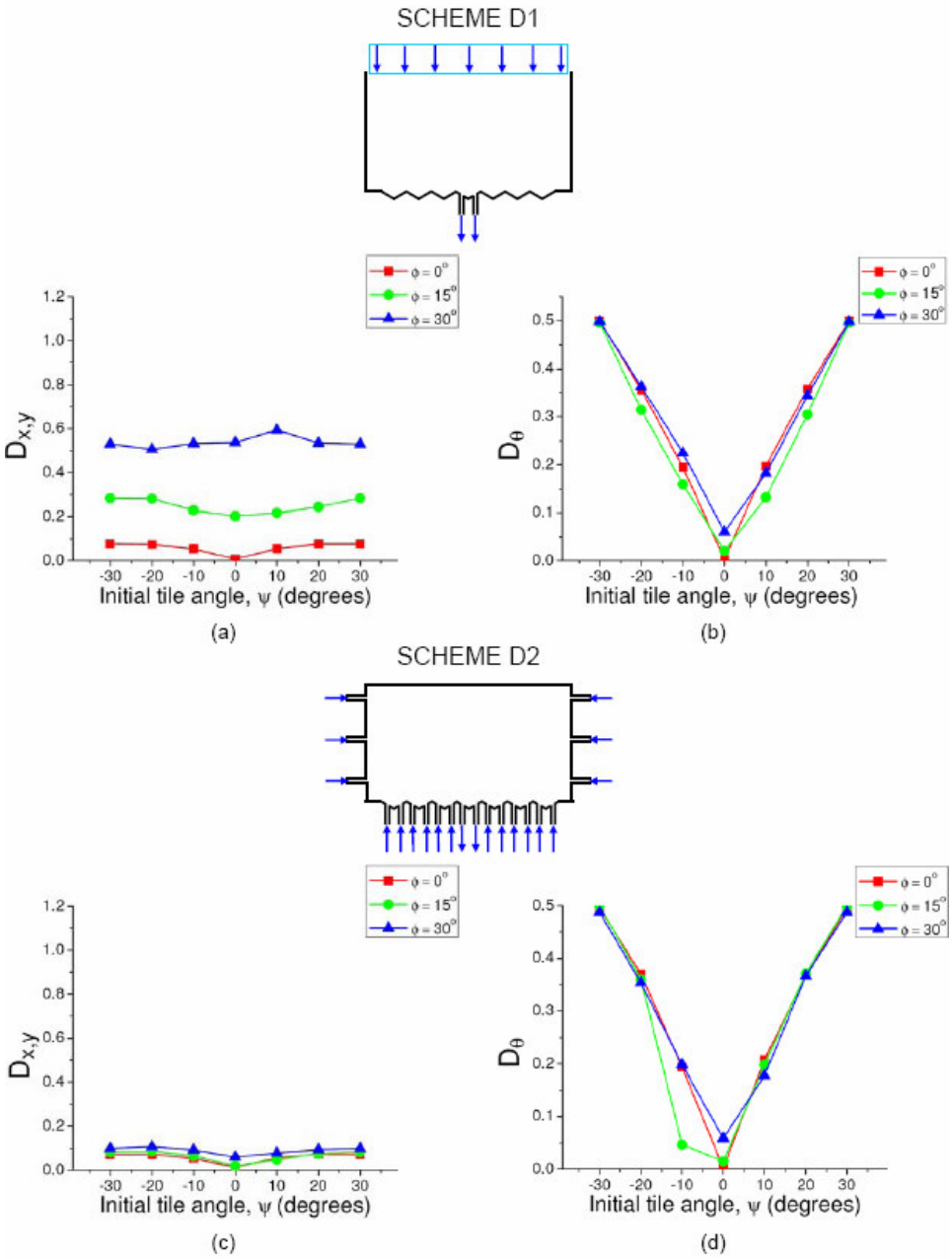

Figure 2.11. $D_{x,y}$ and D_θ for schemes D1 and D2. (a) – (b) Scheme D1 (c) – (d) Scheme D2.

2.5.5 Effect of tile shape

Two different tile shapes were studied in these simulations, namely a square tile shape (Schemes A1, A2, B1, B2, C1 and C2) and a hexagonal tile shape (Schemes D1 and D2). By comparing Figures 2.8, 2.9 and 2.10 which show the variation of the docking parameters for square tiles, with Figure 2.11 which shows the same for hexagonal tiles, the following results may be observed. Firstly, the values of the Translational Docking parameter, $D_{x,y}$, for different initial tile positions and orientations tended to be lower for the hexagonal tile shape indicating that the hexagonal tile performed better than the square tile in terms of translational docking. However, on comparing the Rotational Docking parameter, D_{θ}, it was found that the hexagonal tile did not undergo significant rotation due to the flow field, as discussed previously. This lack of rotation is probably due to the increased number of sides in a hexagonal tile as compared to a square tile, and could be useful in designing future assembly schemes where an alternative method that does not directly involve the use of fluid motion (such as using the shape of the hexagon) is used to deterministically control the initial orientation of a hexagonal tile upstream of the assembly site. Subsequently, fluid flow can be used to transport and assemble the tile at the desired location without changing its orientation.

Figure 2.12 and 2.13 show tile locations as a function of time for tiles having initial orientation $\psi = 45°$ (for square tiles) and $\psi = 30°$ (for hexagonal tiles), and initial position $\varphi = 30°$. The black outlines squares and hexagons indicate the target tile locations while the arrows indicate fluid outlets. The flow lines shown here are pathlines, and the effect of multiple side inlets on the final tile position and orientation

can be clearly seen here. Figure 2.12 shows the path of a tile moving through the chamber with a single top inlet (Schemes A1, B1, C1 and D1), while Figure 2.13 shows the path of a tile moving through the chamber with multiple side inlets (Schemes A2, B2, C2 and D2), with the images showing the variation of the tile position with time as the assembly process progresses.

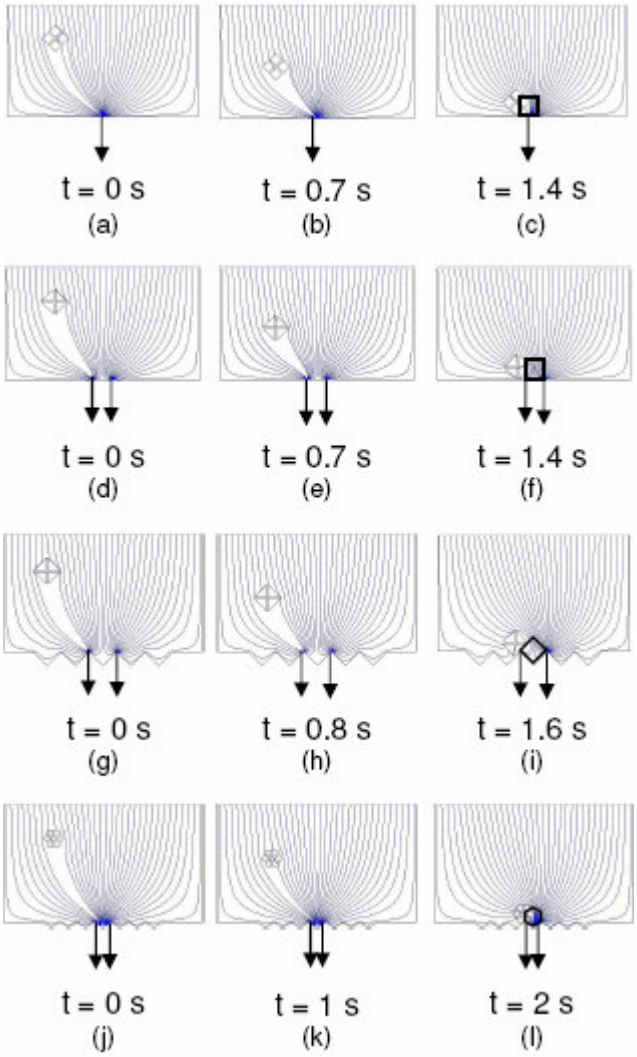

Figure 2.12. Time elapse images showing tile locations for tiles with initial tile orientation $\psi = 45°/30°$, and initial position $\varphi = 30°$. (a) – (c) Scheme A1 (d) – (f) Scheme B1 (g) – (i) Scheme C1 (j) – (l) Scheme D1. The black outlined squares and hexagons indicate the target tile locations, while the arrows indicate fluid outlets.

We can characterize the time taken for a tile to assemble by defining a non-dimensional time constant for the assembly process as $t_0 = l/V$. Then, the time taken for tiles to assemble was found to be between $4t_0$ to $6t_0$ for the schemes with a single top inlet (Schemes A1, B1, C1 and D1) with $t_0 = 0.333$ s. Similarly for the schemes with multiple side inlets (Schemes A2, B2, C2 and D2) with $t_0 = 0.0333$ s, assembly time was found to be between $40t_0$ to $60t_0$.

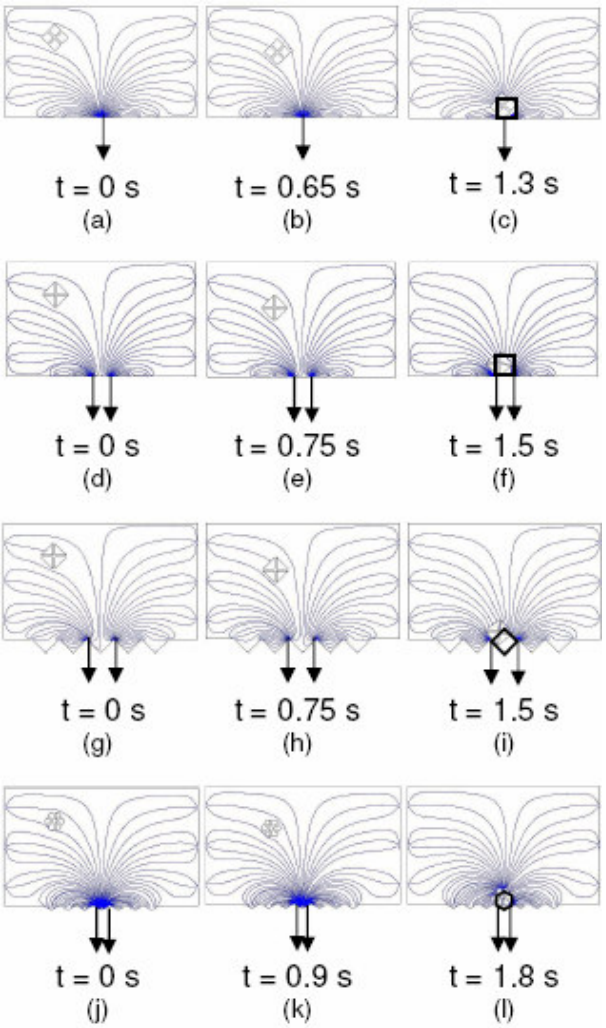

Figure 2.13. Time elapse images showing tile locations for tiles with initial tile orientation $\psi = 45°/30°$, and initial position $\varphi = 30°$. (a) – (c) Scheme A2 (d) – (f) Scheme B2 (g) – (i) Scheme C2 (j) – (l) Scheme D2. The black outlined squares and hexagons indicate the target tile locations, while the arrows indicate fluid outlets.

The images in the above figures show the tile position at the beginning, halfway through and at the end of the assembly. Multiple side inlets are seen to improve the translational docking of the tile, placing the tile nearer the final target location as compared to a single top inlet. Similar trends in terms of rotation docking are not seen though, and the side inlets do not pose a clear advantage over the top inlet in terms of rotational docking ability.

2.5.6 Quantitative comparison of assembly schemes

In order to evaluate which scheme led to the most number of successful assemblies, a histogram showing the mean values of the two docking parameters for all initial tile conditions (both position and orientation) was plotted for the different assembly schemes studied (Figure 2.14). The error bars in the histogram plot indicate the standard deviation in the docking parameter values for these schemes. This figure shows that Schemes A2, B2, C2 and D2 have lower values of both $D_{x,y}$ as well as the standard deviation of $D_{x,y}$ as compared to Schemes A1, B1, C1 and D1 respectively. This indicates, as previously discussed, that assembly schemes with multiple side inlets (Schemes A2, B2, C2 and D2) led to more successful translational docking, both in terms of number of successful docking events as well as degree of success, compared to assembly schemes where there was a single top inlet directly above the outlet. Also, on comparing the different assemblies, we found that Scheme D2 had the lowest mean value of $D_{x,y}$, making it the most successful scheme of the various schemes considered in terms of the Translational Docking Parameter. Scheme A2 and B2 were also found to work well, with a low mean value of the $D_{x,y}$ docking parameter

and low standard deviation. Thus, the use of inlet jets orthogonal to the direction of desired tile motion worked well to direct the tile to the target location.

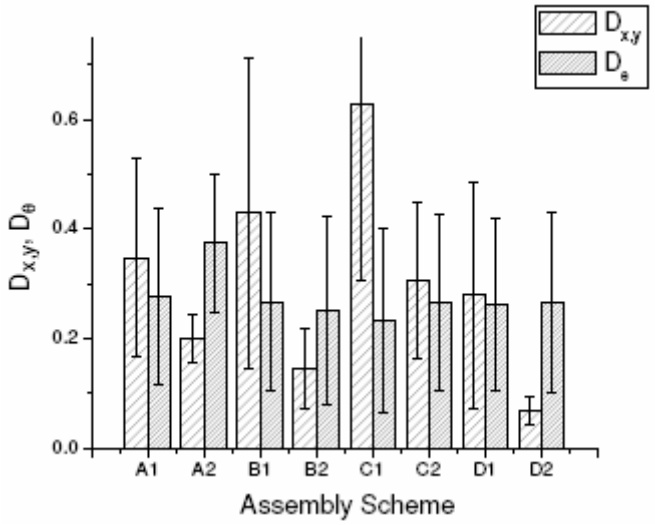

Figure 2.14. Histogram comparing different assembly schemes based on docking parameters.

There was, however, a large amount of scatter in the D_θ values for all the assembly schemes considered, indicated by the large values of standard deviation in the D_θ histogram, and there was no clear indication of which scheme had the best rotational docking capabilities. A good trend did emerge when the assembly schemes were judged based on both the Translational and Rotational Docking parameters though. It is clear from Figure 2.14 that schemes B2 and D2 were amongst the most successful assembly schemes, combining good translational docking and rotational docking properties. As mentioned previously though, the hexagonal tile in scheme D2 did not undergo significant rotation due to the flow field, while scheme B2 showed a definite tendency to rotate the square tile to a 0° angle. Thus scheme D2 can be used to successful assemble a hexagonal tile provided an alternate scheme exists to initially

orient the hexagonal tile. Similarly, scheme B2 can be used as a successful assembly scheme for square tiles.

2.6 Conclusions

The work we have presented here describes a two-dimensional fluid mechanics model that predicts the motion of a tile through a fluidic chamber due to translational forces and rotational torques on the tile, while capturing relevant three dimensional effects, as was seen by comparison with three dimensional simulations and experimental results. This two dimensional approach serves to significantly reduce computational time and resources, and as such is more amenable for extension to a multi-tile environment. The model was also used to quantitatively compare different assembly schemes using two docking parameters. Since initial tile position and orientation in an assembly chamber is stochastic, we attempted to arrive at an assembly procedure that led to successful assembly over the broadest range of initial tile conditions. On comparing different assembly schemes, it was found that the use of side ports in a chamber, with inlet jets orthogonal to the direction of tile motion gave the most successful tile assembly results. Additionally, it was found that these jets were successful in correcting the initial orientation of a square tile, and the use of a dual outlet configuration served to align the square tile on a flat substrate. It was also found that the flow field did not significantly affect the initial orientation of a hexagonal tile which docked at angles similar to the initial angle of the tile.

2.7 Acknowledgements

This work was supported by the National Science Foundation under Grant CMMI-0634652 “Hierarchical Microfabrication: Actively Programmable Multi-level Fluidic Self-Assembly”.

2.8 Additional Comments

In this section, I will further elaborate on some details on the analytical and simulation work performed here.

The boundary conditions at the inlets were handled as velocity boundary conditions, with the outlet velocity being obtained as a result of the simulation. We expect realistic solutions to the flow equations till the tile is close to the outlet. To minimize the error close to the outlet, we ensured good mesh quality and a large number of mesh elements when the tile came close to the outlet, though error is expected when the tile is closer than a distance of the order of the outlet dimension. In the qualitative comparison carried out between simulations and experiments in Figure 2.5, the non-dimensionalized time, $t^* = tV/l$, between successive frames was kept the same for simulation and experimental results to ensure a good comparison. As described in Section 2.5.1, the actual velocity of the flow did not affect the path of the tile, since the fluid regime is Stokesian for the velocities considered, and thus the absolute time between frames was not considered relevant. Regarding the Translational Docking Parameter, $D_{x,y}$, Section 2.5.2 describes the upper bound as being $\max(D_{x,y}) \sim L/l$. The term L/l can have a minimum value of O(1), when $L \sim l$, and thus based on this description, the $max(D_{x,y}) >> 1$. However, based on the

description of the minimum value of $D_{x,y}$ provided in Equation 2.17a, the lower bound for $D_{x,y}$ is 0 and thus $max(D_{x,y})$ can also be thought of as being described as $max(D_{x,y}) >> 0$. Finally, regarding the simulation space of initial tile conditions we explored, we did not specifically consider the effect of initial tile distance from the target position. This parameter was not considered since we would only expect it to affect assembly time, but not the success of assembly. The success of assembly would however be affected by the tile orientation with respect to the flow field which was something we explored through our simulations. For all the assembly cases described here, the target position of the tile in the x direction, x_0 was located directly above the outlet (for the case of a single outlet), or in between the outlets (for the case of dual outlets), while the target position in the y direction, y_0 was such that the tile docked to sit on the substrate.

REFERENCES

1. Madou, M. J. *Fundamentals of microfabrication : the science of miniaturization*. (CRC Press, 2002).

2. Whitesides, G. M. & Grzybowski, B. Self-Assembly at all scales. *Science* **295** (2002).

3. Philp, D. & Stoddart, J. F. Self-assembly in natural and unnatural systems. *Angew. Chem.* **35** (1996).

4. Jackman, R. J., Brittain, S. T., Adams, A., Prentiss, M. G. & Whitesides, G. M. Design and fabrication of topologically complex, three-dimensional microstructures. *Science* **280** (1998).

5. Cohn, M. B. *et al.* in *Proc. SPIE Micromachining and Microfabrication, Conference on Micromachining and Microfabrication Process Technology IV* 2-16 (SPIE, Santa Clara, CA, USA, 1998).

6. Böhringer, K. F., Fearing, R. S. & Goldberg, K. Y., Ch. 55, (J. Wiley, 1999).

7. Whitesides, G. M. & Boncheva, M. Beyond molecules: Self-assembly of mesoscopic and macroscopic components. *PNAS* **99** (2002).

8. Winfree, E., Liu, F. R., Wenzler, L. A. & Seeman, N. C. Design and self-assembly of two-dimensional DNA crystals. *Nature* **394** (1998).

9. Olenyuk, B., Whiteford, J. A., Fechtenkötter, A. & Stang, P. J. Self-assembly of nanoscale cuboctahedra by coordination chemistry. *Nature* **398** (1999).

10. Bowden, N., Terfort, A., Carbeck, J. & Whitesides, G. M. Self-assembly of mesoscale objects into ordered two-dimensional arrays. *Science* **276** (1997).

11. Srinivasan, U., Liepmann, D. & Howe, R. T. Microstructure to substrate self-assembly using capillary forces. *J. MEMS* **10** (2001).

12. Srinivasan, U., Helmbrecht, M. A., Rembe, C., Muller, R. S. & Howe, R. T. Fluidic self-assembly of micromirrors onto microactuators using capillary forces. *IEEE J. Sel. Top. in Quantum Elec.* **8** (2002).

13. Xiong, X. *et al.* Controlled multibatch self-assembly of microdevices. *J. MEMS* **12** (2003).

14. Chung, J., Zheng, W., Hatch, T. J. & Jacobs, H. O. Programmable reconfigurable self-assembly: Parallel heterogeneous integration of chip-scale components on planar and nonplanar surfaces. *J. MEMS* **15** (2006).

15. Yeh, H. J. & Smith, J. S. Fluidic Self-Assembly for the integration of GaAs Light-Emitting Diodes on Si substrates. *IEEE Photon. Technol. Lett.* **6** (1994).

16. Zheng, W. & Jacobs, H. O. Shape-and-solder-directed self-assembly to package semiconductor device segments. *Appl. Phys. Lett.* **85** (2004).

17. Ye, Y. H., Badilescu, S., Truong, V. V., Rochon, P. & Natansohn, A. Self-assembly of colloidal spheres on patterned substrates. *Appl. Phys. Lett.* **79** (2001).

18. Golosovsky, M., Saado, Y. & Davidov, D. Self-assembly of floating magnetic particles into ordered structures: A promising route for the fabrication of tunable photonic band gap materials. *Appl. Phys. Lett.* **75** (1999).

19. Tanase, M. *et al.* Magnetic trapping and self-assembly of multicomponent nanowires. *J. App. Phys.* **91** (2002).

20. Higuchi, Y. *et al.* in *Proc. 21st IEEE Int. Conf. Micro Electro Mechanical Systems (MEMS).* (eds O. Brand & Y. Zohar) 836-839.

21. Krishnan, M., Tolley, M. T., Lipson, H. & Erickson, D. in *Proc. ASME Int. Mech. Engg. Cong. Exp. (IMECE)* 41784 41781-41786 (ASME Press, Seattle, Washington, USA, 2007).

22. Tolley, M. T., Baisch, A., Krishnan, M., Erickson, D. & Lipson, H. in *Proc. 21st IEEE Int. Conf. Micro Electro Mechanical Systems (MEMS).* (eds O. Brand & Y. Zohar) 1073-1076.

23. Ganguly, R., Gaind, A. P. & Puri, I. K. A strategy for the assembly of three-dimensional mesoscopic structures using a ferrofluid. *Phys. Fluids* **17** (2005).

24. Ganguly, R., Zellmer, B. & Puri, I. K. Field-induced self-assembled ferrofluid aggregation in pulsatile flow. *Phys. Fluids* **17** (2005).

25. Liu, D., Maxey, M. R. & Karniadakis, G. E. Simulations of dynamic self-assembly of paramagnetic microspheres in confined microgeometries. *J. Micromech. Microeng.* **15** (2005).

26. Lee, C. H., Lu, Y. & Shen, A. Q. Evaporation induced self assembly and rheology change during sol-gel coating. *Phys. Fluids* **18** (2006).

27. Böhringer, K. F., Srinivasan, U. & Howe, R. T. in *Proc. 14th IEEE Int. Conf. Micro Electro Mechanical Systems (MEMS).* 369-374.

28. Abbasi, S., Zhou, A. X., Baskaran, R. & Böhringer, K. F. in *Proc. 21st IEEE Int. Conf. Micro Electro Mechanical Systems (MEMS).* (eds O. Brand & Y. Zohar) 1060-1063.

29. Onoe, H., Matsumoto, K. & Shimoyama, I. Three-dimensional micro-self-assembly using hydrophobic interaction controlled by self-assembled monolayers. *J. MEMS* **13** (2004).

30. Aidun, C. K., Lu, Y. N. & Ding, E. J. Direct analysis of particulate suspensions with inertia using the discrete Boltzmann equation. *J. Fluid Mech.* **373** (1998).

31. Cherukat, P. & McLaughlin, J. B. The intertial lift on a rigid sphere in a linear shear-flow field near a flat wall. *J. Fluid Mech.* **263** (1994).

32. Feng, J., Hu, H. H. & Joseph, D. D. Direct simulation of initial value problems for the motion of solid bodies in a Newtonian fluid. Part 2: Couette and Poiseuille flows. *J. Fluid Mech.* **277** (1994).

33. Feng, J., Hu, H. H. & Joseph, D. D. Direct simulation of initial value problems for the motion of solid bodies in a Newtonian fluid. Part 1: sedimentation. *J. Fluid Mech.* **261** (1994).

34. Kim, I., Elghobashi, S. & Sirignano, W. A. On the equation for spherical-particle motion: effect of Reynolds and acceleration numbers. *J. Fluid Mech.* **367** (1998).

35. Maxey, M. R. & Riley, J. J. Equation of motion for a small rigid sphere in a nonuniform flow. *Phys. Fluids* **26** (1983).

36. Blackburn, H. M. & Henderson, R. D. A study of two-dimensional flow past an oscillating cylinder. *J. Fluid Mech.* **385** (1999).

37. Kang, S. M., Choi, H. C. & Lee, S. Laminar flow past a rotating circular cylinder. *Phys. Fluids* **11** (1999).

38. Sherwood, J. D. & Stone, H. A. Added mass of a disc accelerating within a pipe. *Phys. Fluids* **9** (1997).

39. Panton, R. L. in *Incompressible Flow*, Ch. 22, (J. Wiley, 2005).

40. Batchelor, G. K. in *An Introduction to Fluid Dynamics*, Ch. 4, (Cambridge University Press, 2000).

CHAPTER 3

HYDRODYNAMICALLY TUNABLE AFFINITIES FOR FLUIDIC ASSEMBLY*

3.1 Abstract

Most current micro- and nanoscale self-assembly methods rely on static, preprogrammed assembly affinities between the assembling components such as capillarity, DNA base pair matching and geometric interactions. While these techniques have proven successful at creating relatively simple and regular structures, it is difficult to adapt these methods to enable dynamic reconfiguration of the structure or on-the-fly error correction. Here we demonstrate a technique to hydrodynamically tune affinities between assembling components by direct thermal modulation of the local viscosity field surrounding them. This approach is shown here for two dimensional silicon elements of 500 μm length using a thermorheological fluid that undergoes reversible sol-gel transition on heating. Using this system we demonstrate the ability to dynamically change the assembly point in a fluidic self-assembly process and selectively attract and reject elements from a larger structure. Although this technique is demonstrated here for a small number of passive mobile components around a fixed structure, it has the potential to overcome the some limitations of current static affinity based self-assembly.

---

* Reprinted with permission from Krishnan, M., Tolley, M. T., Lipson, H. and Erickson, D., "Hydrodynamically tunable affinities for fluidic assembly", Langmuir, **25** (6), 3769, 2009. Available online at http://pubs.acs.org.

3.2 Introduction

Self-assembly[1,2] has been used to create structures at the micro- and nanoscales using techniques such as chemical bonding[3-5], fluid and surface tension based attraction[6-10], geometric interactions[11,12] and magnetic fields[13,14] as the assembly driving mechanism. Most of these self-assembly processes create either highly regular structures such as colloidal crystals[15], or small scale complex structures comprised of, for example, DNA polymers[16]. Recently Chung *et al.*[10] have developed a guided fluidic self-assembly process that allows for the assembly of relatively large irregular structures. Using this technique, the authors were able to design the assembling components on-the-fly and transport them on a railed network to the assembly site. While this technique is very flexible in the shape of the components, their motion is confined by the pre-defined rail networks on which these components move.

A hurdle to exploiting the potential of self-assembly is the inability of current techniques to assemble complex structures comprising large numbers of particles in non-regular, non-predefined geometries. One of the reasons for this is the use of static interactions, or *affinities* between the assembling components to drive the assembly process. For example, in nucleic-acid driven assembly, the final structure is governed by the predefined base-pair sequence[3,17]. As a result, the assembling components and their affinities need to be specifically designed *a priori* for a given target structure. Since each affinity sequence corresponds to a specific target structure, assembled structures are also not generally reconfigurable. Similar arguments can be made for many hydrophobic/hydrophilic[7,8,18] and geometric/surface tension interactions[11,12]. In addition, static affinities also limit the complexity of the final target structure. This is

because the number of patterns needed to uniquely specify any non-regular structure increases rapidly with structure size and consequently so does the complexity and number of the affinity patterns required to uniquely specify this structure. However, this increase in the number of required affinity patterns means that the difference between them or the *specificity* decreases. This leads to both slower assembly rates and increasing numbers of assembly errors. Error correction is similarly difficult to implement since the static affinities between components cannot be turned off to remove incorrectly assembled pieces.

One way to address the above issues is to develop a means to dynamically (*i.e.* during assembly) tune affinities between assembling components. The concept of affinity switching has been demonstrated at the centimeter scale using mechanical and magnetic switching[19-23]. These methods however are difficult to implement at the microscale due to fabrication constraints and energy limitations. At the microscale, other researchers have attempted to switch the hydrophobicity of surfaces using electric potentials[24]. Gripping and releasing microstructures using electrowetting based techniques[25] has also been demonstrated. To date however these approaches have not been applied to dynamically modulate affinities during self-assembly, and the binding strength of these bonds are typically low. Directed control over self assembly has been demonstrated both thermorheologically[26] and electrochemically[27] however these methods have not been applied to affinity switching/tuning, assembly error correction or structural reconfiguration. Dynamic self-assembly has been demonstrated through external manipulation of magnetic and electrostatic fields[28].

The resulting systems however are based on stable non-equilibrium configurations that remain ordered only as long as the systems continue to dissipate energy.

In this paper, we present a method to carry out the hydrodynamic tuning of attraction affinities between microscale assembly components using thermal modulation of the local flow field. We demonstrate the affinity tuning technique using a small set of mobile passive silicon components around a fixed structure and illustrate how it could be used to reconfigure structures, create different target structures from the same starting components and carry out error correction. As we describe in detail below, this is done using a thermorheological fluid that undergoes a reversible sol-gel transition on heating. This property of the fluid is used to modulate the local flow field around the mock component and thus tune inter-component affinities. In addition to experimental results with the mobile silicon tiles, we also characterized the affinity switching properties of the system using fluorescent polystyrene particles to visualize the local flow field and Rhodamine B to study the thermal field.

Our process for affinity switching is shown in the schematic in Figure 3.1. In a fluidic self-assembly process, locally restricting the flow near one face of the structure limits the probability of another component being attracted to that face. Hence that part of the structure has no affinity for an approaching component, while other parts of the structure are still positive affinity regions. Figure 3.1 shows the use of affinity switching by flow modulation to create irregular structures, reconfigure structures and carry out error correction.

While it is possible to use active flow control elements like valves on the assembling components to locally modulate flow, this requires significant component

level fabrication. Instead, we employ "smart-fluids" which create self-assembled structures on the application of a suitable stimulus thus increasing the effective viscosity in the stimulated region. Our approach uses thermorheological fluids that undergo reversible sol-gel transition on heating. Other smart-fluids like electro-rheological fluids[29] may also have been used, but we found that the particles were too big (on the order of 25 μm), and the required voltages too large (on the order of kV/mm) for our purposes here.

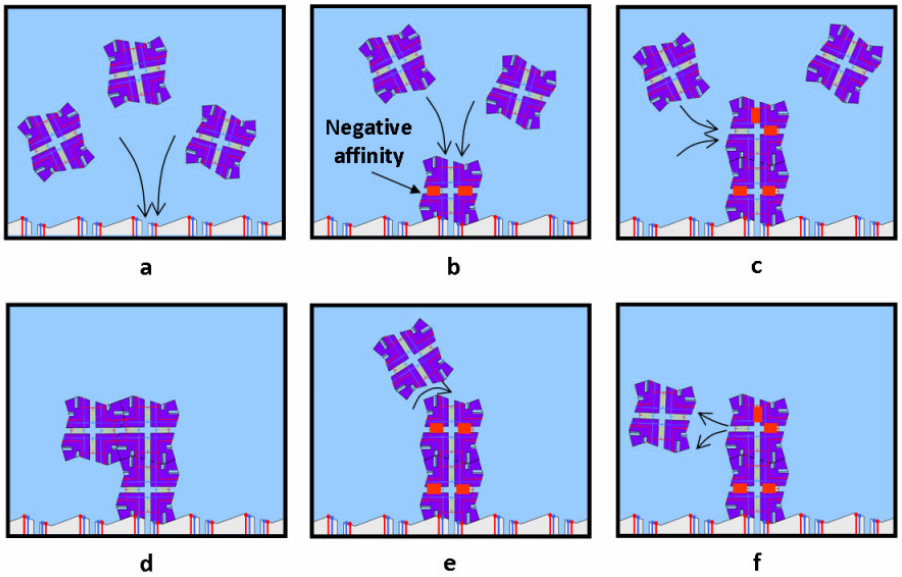

Figure 3.1. Schematic demonstrating the use of dynamically tunable affinities to create arbitrary, programmable and reconfigurable structures. (a) shows the attraction of a sub-element moving stochastically in the fluid to the substrate. The sub-elements are unpowered while in the fluid, but once they are attached to the substrate they can draw power to switch their affinities. (b), (c) depict the building of an arbitrary target structure by dynamically switching the affinities within the structure and controlling the local attraction basin around the structure. (d) shows the final assembled structure. (e) shows reconfiguration of the assembled structure by switching affinities. (f) shows error correction to reject an incorrectly assembled component.

To demonstrate the principle of hydrodynamically tunable affinities, we developed a structure consisting of a "mock" assembling component (or tile) with microchannels

through it that is fixed in the microchamber where assembly is carried out. This represents a target structure that is being populated by further adding on approaching tiles to the existing structure. The mock tile was located in a microfluidic chamber[30] and a "mobile" silicon tile was introduced into the chamber for the experiments which we discuss below. The chamber was filled with a thermorheological fluid made of an aqueous solution of a triblock copolymer, poly(ethylene oxide)$_{106}$ – poly(propylene oxide)$_{70}$ – poly(ethylene oxide)$_{106}$ (see Materials and Methods section for details). Local heating of the thermorheological solution results in a rapid viscosity increase of the solution to reach a gel state, effectively shutting off flow in that region[31,32]. On cooling, the gel returns to liquid state and flow resumes. Affinity tuning by thermal flow modulation can take place by fabricating microheaters on board the assembling components. Here we focus on demonstrating the principle of hydrodynamic affinity tuning and thus pattern platinum microheaters under the channels of the fixed structure to modulate the local temperature field. In section 4.0 we discuss in detail the challenges involved in up scaling the technique to the case where mobile tiles would also contain local heaters. The heaters were designed by performing numerical analysis to ensure that they provided sufficient heating to cause gelation of the fluid (see Supplementary Information, 3.7 for details on the simulations). Flow in the microchamber was driven using a pressure system and each of the microheaters was controlled independently using a voltage source and a relay arrangement.

3.3 Materials and Methods

3.3.1 Materials

We use a 15% (w/w) aqueous solution of Pluronic F127 (BASF) to make the thermorheological fluid. Pluronic F127 is triblock copolymer, poly(ethylene oxide)$_{106}$ – poly(propylene oxide)$_{70}$ – poly(ethylene oxide)$_{106,}$ and a 15% solution has a gelation temperature of approximately 30 °C. The Pluronic F127 particles obtained from BASF were dissolved in DI water and left for 24 hours in the refrigerator to dissolve the particles completely. The solution was brought to room temperature again prior to doing the experiments. We visualize the flow of the thermorheological fluid using suspended particles consisting of green fluorescent polystyrene particles of 0.72 μm diameter (Duke Scientific). Our microfluidic chamber was fabricated using polydimethylsiloxane (PDMS) obtained from Ellsworth Adhesives.

3.3.2 Fabrication

The microfluidic chamber used for our experiments was fabricated using standard photolithography techniques. A pyrex wafer was patterned with 30 nm of titanium and 150 nm of platinum to create the microheaters. This was followed by deposition of 250 nm of silicon nitride using plasma enhanced chemical vapor deposition to electrically insulate the thermorheological fluid from the heaters. The silicon nitride over the contact pads was then etched using reactive ion etching using photoresist as an etch mask for the other regions. The fluid layer was formed by first making a mold on a silicon wafer by deep silicon etching using a Bosch etching tool. PDMS was then poured over this mold and cured to fabricate a microfluidic chamber having a height

of 50 μm. The PDMS layer was finally bonded to the pyrex substrate by plasma cleaning both layers, aligning and leaving them overnight in a convection oven at 80 °C. The assembling tiles were made of 30 μm thick silicon from a silicon-on-insulator wafer using a deep Bosch etch followed by an HF release of the tiles.

3.3.3 Experimental technique

The silicon tiles were stored in the thermorheological fluid and were pipetted into the microchamber. The thermorheological fluid was pumped into the microchamber through Tygon tubing using pressurized air at 0-5 psi. The pressure lines were controlled off-chip by solenoid valves and their controllers obtained from Fluidigm Corporation. Each fluidic port in the chamber was subject to either a positive pressure (resulting in flow into the chamber) or no applied pressure (resulting in flow out of the chamber due to applied pressure at the other ports). The microheaters were controlled off-chip using a relay and data acquisition card obtained from Omega. Power was supplied to the heaters using a voltage supply of 0-30 V range obtained from Hewlett Packard. Flow was visualized where needed using 0.72 μm fluorescent polystyrene beads obtained from Duke Scientific.

3.4 Results and Discussion

Figures 3.2a - d illustrate an experiment where the mobile tile was moved from one face of the mock tile to another by switching the affinity of the first face from positive to negative. The blue arrows in the figure illustrate the direction of flow during the reconfiguration process but not necessarily the relative magnitudes. The flow rates at

each inlet port were equal since the applied pressure was fixed. The same applies at the outlet ports however in general the inlet and outlet velocities were different in magnitude since the relative pressure difference was not the same.

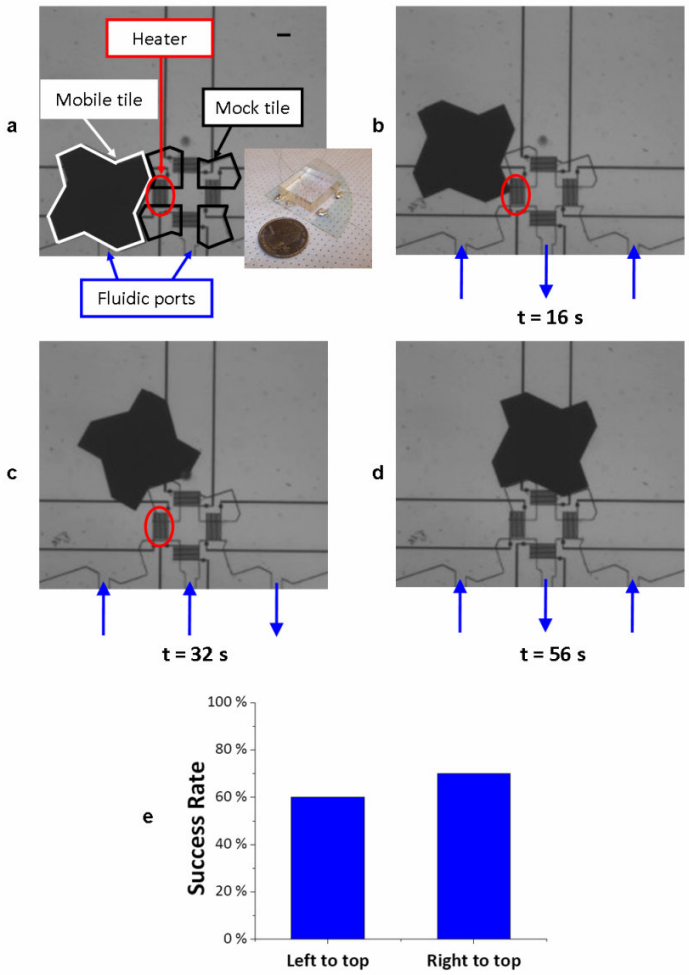

Figure 3.2. Change of assembly location by dynamically tuning affinities. (a) Optical micrograph of microfluidic assembly chamber. The chamber has a mock tile made of PDMS, a mobile tile made of silicon, platinum heaters and fluidic ports. The inset image shows the final chip with electrical leads. The scalebar in the image is 100 μm. (b) – (d) show tile manipulation around the mock tile demonstrating the ability to reconfigure the final structure. A mobile silicon tile was moved around the mock tile by dynamically tuning the affinities at the faces of the mock tile through heater actuation. The blue arrows in the figures represent regions where flow enters or leaves the chamber, while the red circles show the heater being actuated. The blue arrows are representative of the direction of flow but not nessesarily the magnitude. (e) Histogram showing percentage of successful tile assemblies for a mobile tile moving around the mock tile.

By turning the microheaters on (or off), local affinities on each face of the mock tile were disabled (or enabled), increasing the probability of the mobile tile being attracted to one face over the others. The mobile tiles used in these experiments had a tendency to come towards their assembly point at a corner, and thus it was essential to use external flow manipulation (see the reversed flow used in Figure 3.2c) to ensure that the tiles aligned properly in their new position. In all cases, the tile was found to move towards the desired face, though the attraction affinity was not sufficient in all of the cases to cause the tile to completely switch positions to another face on the mock tile. The statistics of successful assembly events resulting from these manipulations are shown in Figure 3.2e for ten consecutive trials of the same experiment. This experiment demonstrated the ability of tunable affinities to change the assembly point on the fly by manipulating the local flow field. This concept could in principle be used to carry out reconfiguration of a self-assembled structure. Supplemental video *erickson_reconfigurable_assembly.mpg* shows a successful trial from this experiment.

We visualized the flow through the mock tile using fluorescent polystyrene beads and characterized the effect of the microheaters on the local flow velocity and gelation within the mock tile at different applied voltages. Figures 3.3a - c and supplemental movie *erickson_flow_modulation.mpg* show these results. These figures show images from experiments where the pressure applied to the flow was 4 psi corresponding to a flow velocity through the channels in the tile of 1725 μm/s and different voltages were applied to the heater. Larger voltages resulted in larger regions of gelation around the heater as can be seen in these images.

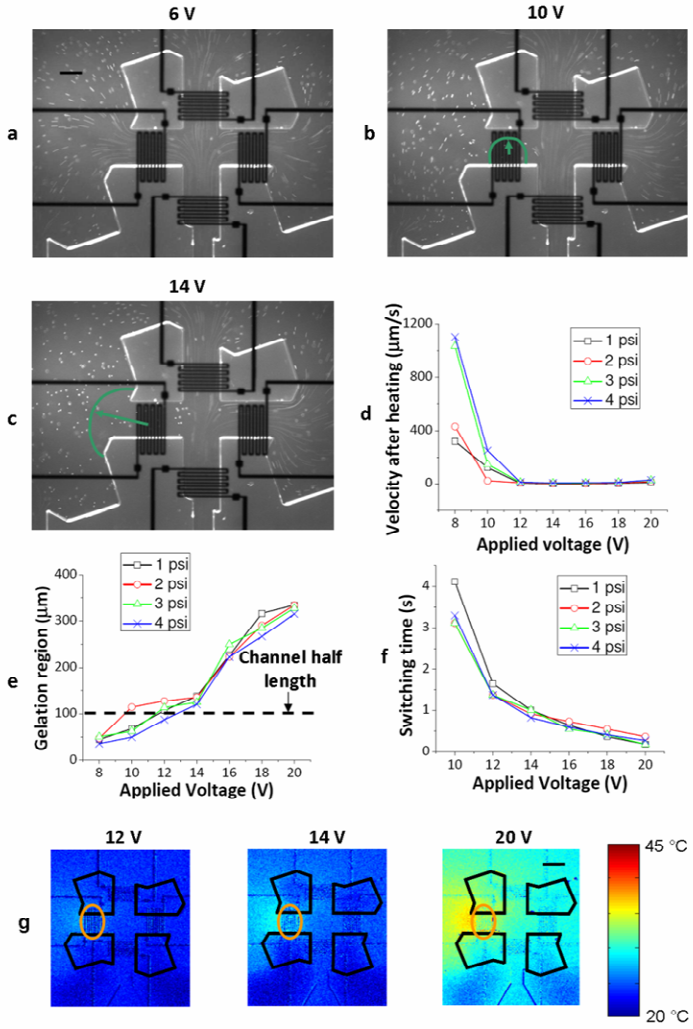

Figure 3.3. Characterization of hydrodynamic affinity tuning. (a) – (c) Images showing the effect of different voltages on the gelation region in the chamber. The scalebar in the image is 100 µm. The green curves show the region in the chamber that is gelled. (d) Graph showing the variation of flow velocity within the mock tile on heating at different heater voltages for different initial flow velocities. A voltage of 10 V and higher was found to stop flow within the channel of the mock tile. (e) Graph showing the characteristic length of the gelled region in the chamber for different heater voltages at different initial flow velocities. Voltages above 12 V were found to gel regions beyond just the channel which is undesirable. (f) Graph showing the response time of the thermorheological fluid for complete switching of flow, at different voltages and different initial flow rates. g, Temperature profile in the microfluidic assembly chamber for different voltages, measured experimentally using Rhodamine B. The legend indicates temperature in °C and the orange circles show the heaters being used. A voltage of 10 V and higher was found to raise the temperature sufficiently to cause gelation and affinity switching.

The variation of flow velocity through the heated channel and the characteristic length of gelation in the channel are shown in the graphs in Figure 3.3d and 3.3e respectively, for different driving pressures. From the graph in Figure 3.3d we see that voltages of 10 V and higher resulted in near zero flow velocity through the channel of the mock tile, thus achieving flow redirection and affinity switching. A voltage of 8 V was found to reduce the flow velocity from its original velocity but not stop flow completely, whereas voltages below 8 V resulted in no change in the flow (not shown in the graph). From Figure 3.3c and the graph in Figure 3.3e we see that at voltages above 12 V, the radius of the gelled region increased well beyond the channel dimension which is undesirable since gelation should occur only in the channel and not in the rest of the chamber. Figure 3.3f shows the time required to carry out complete redirection of flow and affinity switching at different voltages and driving pressures. As expected, the response time was found to decrease with increasing voltage. We also measured the temperature profile within the chamber at different voltages to ensure that the power provided by the heaters was sufficient to carry out gelation of the fluid and that the heat generation was localized. This was done in an aqueous medium, using Rhodamine B dye for the thermal measurements[33]. The temperature measurements were carried out in a purely aqueous medium rather than in the polymer solution since the dye was found to change the gelation properties of the thermorheological fluid. Figure 3.3g shows the results from these experiments. A voltage of 10 V and above was found to locally heat the fluid to a temperature above 30 °C and ensure that gelation takes place, though higher voltages were found to cause non-local heating. Based on these experiments, voltages between 10-12 V were used

for our experiments for heater actuation. We note here that the temperatures shown in Figure 3.3g are at steady state, implying that there is a balance between the energy input by the heaters and the heat loss through the chip.

In this system the majority of the heat loss is through the pyrex substrate, which has a higher conductivity compared to the upper PDMS fluidic layer[33]. Had we used a lower thermal conductivity substrate the heat loss would have been lower and the required input energy would also be less. The higher thermal conductivity substrate however enables much more rapid dissipation of heat during the cooling phase and thus better switching times.

Having successfully demonstrated tile manipulation around the mock tile, we attempted to attract tiles from the far field flow (away from the mock tile structure) to a particular location on this tile depending on which of its faces was tuned to attract the mobile tiles, as can be seen from Figure 3.4. Although the external applied flow field was the same in these experiments, blockage of some of the channels of the mock tile resulted in increased flow rate through the open channels of the tile. We note that the mock structure is not affected by the changes in the flow as it is permanently affixed to the substrate (analogous to being latched on as is demonstrated in Tolley *et al.*[30]). The mobile tile was attracted to different faces on the mock structure depending on which of the microheaters was actuated, even though the same external flow field was applied in all these experiments. We did find that the mobile tile did not align well to the mock structure in all cases since, as mentioned previously, this tile shape was found to inherently come towards its assembly point on a corner. Such a technique could be applied to a fluidic assembly process to create different target

structures from identical initial components and thus allow for programmable assembly. Supplemental video *erickson_programmable_assembly.mpg* contains all the above experimental results.

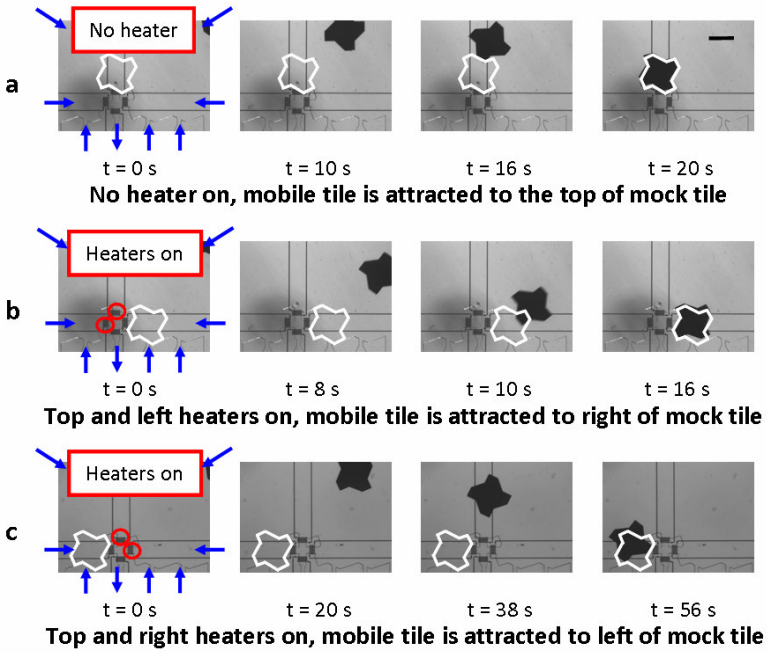

Figure 3.4. Images showing the formation of different final structures by dynamically tuning affinities of the mock tile. The blue arrows show regions where flow enters or leaves the chamber, the red circles show the heaters being actuated and the white tiles show the target position in each case. (a) with no heater action, the mobile tile was attracted to the top of the mock tile forming a vertical column structure. The scalebar in the image is 500 μm. (b) with the top and left heaters on, the mobile tile was attracted to the right of the mock tile forming a horizontal row structure. (c) with the top and right heaters on, the mobile tile was attracted to the left of the mock tile forming a horizontal row structure different from that formed in (b).

As a final experiment, we attempted to assemble non-regular structures with two mobile tiles, and a two tile mock structure as shown in Figure 3.5. Figure 3.5a shows the assembly of such a structure by tuning the affinities of the mock tiles. One mobile tile is first brought in to form a three tile shape (not shown here) followed by the attraction of a second mobile tile to form a non-regular assembly consisting of four

tiles. Other four tile polymorphs were also assembled such as the initial structure in Figure 3.5c. We also studied switching inter-tile affinities to reject assembled tiles from the main structure as shown in Figure 3.5b and c. In these figures we show results from experiments where a mobile tile was rejected from the assembly, keeping the other tile in place, resulting in a new three tile assembly. Although demonstrated here using a fixed mock tile and passive mobile tiles, such an approach could be adapted to carry out error correction in a fluidic assembly process by selectively removing incorrectly assembled units from the main structure. Videos of the above experiments are provided in supplemental video *erickson_error_correction.mpg*.

3.5 Summary and Conclusion

In conclusion, we have demonstrated here the ability to hydrodynamically tune affinities between assembling components using a thermorheological fluid. Unlike self-assembly methods based on static affinities, the technique of tunable affinities presented here has the potential to one day allow the assembly of arbitrary, non-predefined and reconfigurable target structures. Such an assembly method could allow for interesting applications such as self healing structures, tunable electronics and displays.

A challenge to scaling our assembly method to a large number of elements is slow assembly rates due to the need to tune affinities at each stage of the assembly process. This could be overcome by carrying out parallel, hierarchical assembly as well as combining static affinity based assembly approaches (for carrying out coarse

assembly) with dynamic affinity tuning (for fine assembly to describe detailed features on the target structure).

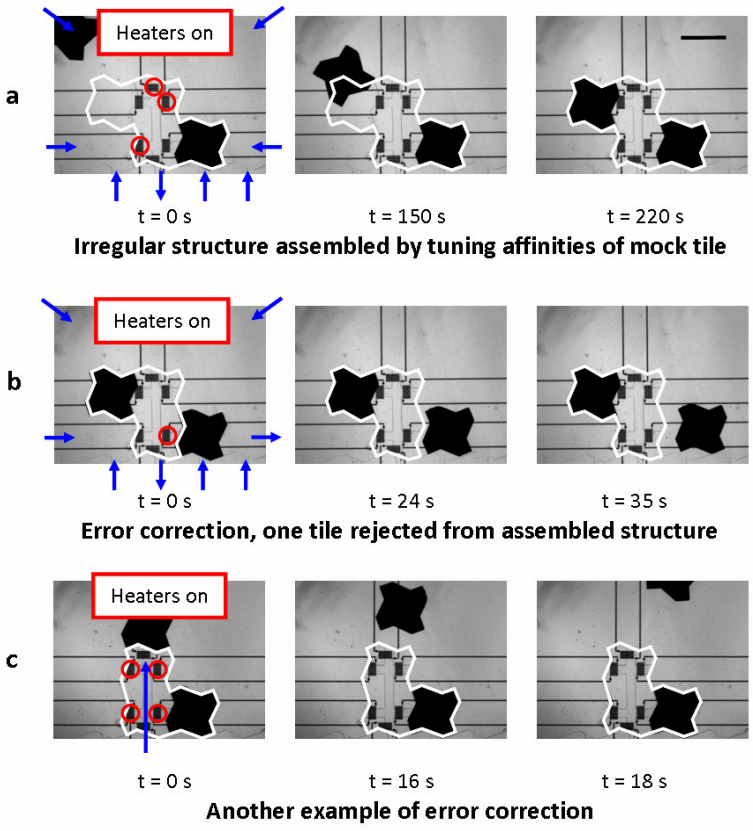

Figure 3.5. Images showing the formation of irregular structures and techniques for error correction. The blue arrows show regions where flow enters or leaves the chamber, the red circles show the heaters being actuated and the white lines show the target structure in each case. (a) An irregular structure consisting of two mobile tiles and a two tile mock structure was formed by selectively tuning affinities. The scalebar in the image is 500 μm. (b) One mobile tile was rejected from this assembled structure while keeping the other tile in place, demonstrating a means to carry out error correction. (c) Another example of error correction showing the rejection of one tile from the assembled structure while keeping the other tile in place.

Although we have demonstrated the ability to fabricate tiles with electrical and mechanical functionality[34], another possible limitation is the complex control schemes needed to operate the heaters for affinity switching during assembly. However, even

though the number of heater control lines scales linearly with the number of elements (with four control lines per two dimensional element), the affinities of only the outer layer of the structure need to be controlled at each level of assembly as new layers are added to the structure. Hence the control scheme for this assembly process does not need to involve all the elements of the assembled structure and can thus be relatively simple. Additionally, combining static and dynamic assembly approaches as mentioned above will further simplify the control schemes required to carry out assembly.

3.6 Acknowledgements

This work was supported by the Defense Advanced Research Projects Agency (DARPA), Defense Sciences Office (DSO) under the Programmable Matter program and the National Science Foundation (NSF) under Grant No. CMMI-0634652, "Hierarchical Microfabrication: Actively Programmable Multi-level Fluidic Self-Assembly."

3.7 Supplementary Information

The heaters were designed by carrying out numerical analysis using the commercial software Comsol Multiphysics to estimate the power required by the microheaters to cause the thermorheological fluid to transition to a gel state. The geometry used for these simulations was the same as that used in the experiments, and we solved for heat flux conditions ranging from 10 W/m^2 to 10^7 W/m^2. Supplemental Figure S1 shows the results from our simulations. It can be seen from Figure 3.6 that for a flux of 10^6

W/m^2, we have an average channel temperature of approximately 50 °C, which is sufficient for gelation. Thus, this was the flux that the heaters were designed to provide.

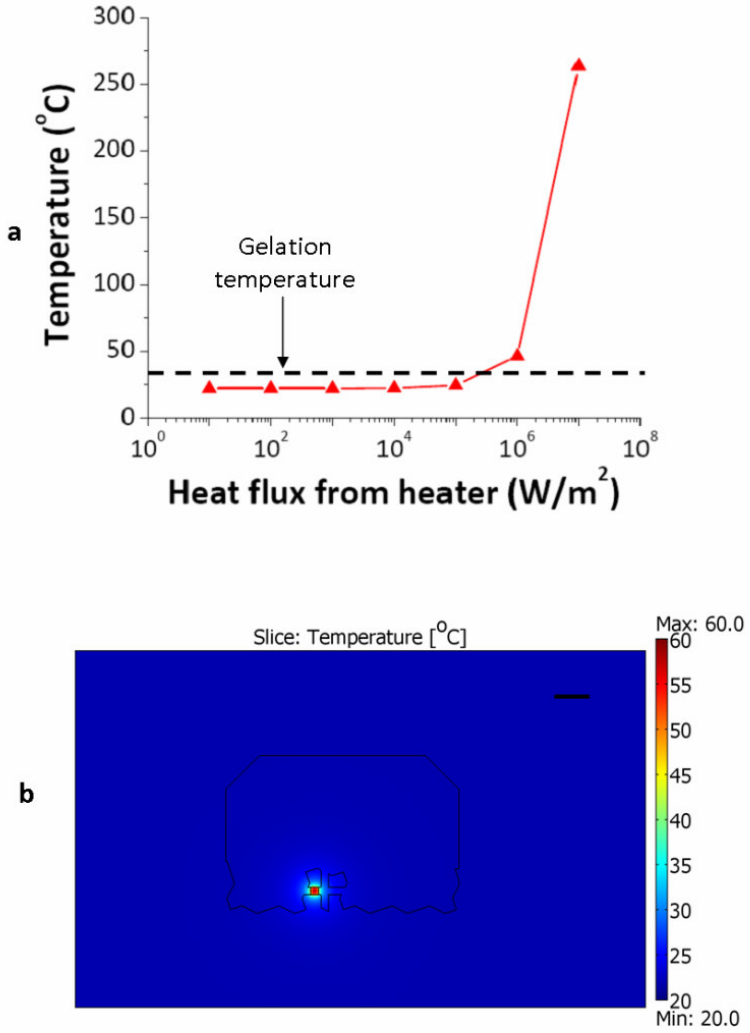

Figure 3.6. Numerical analysis (a) Graph showing the predicted average temperature within a channel in the mock tile for different heat fluxes. It was found that a flux of order 10^6 W/m^2 was needed for successful affinity switching. (b) Simulated temperature profile in the microfluidic assembly chamber for a flux of 10^6 W/m^2. The scalebar in the image is 500 µm. The legend indicates temperature in °C.

REFERENCES

1. Philp, D. & Stoddart, J. F. Self-assembly in natural and unnatural systems. *Angew. Chem.* **35** (1996).

2. Stroock, A. D. *et al.* Chaotic mixer for microchannels. *Science* **295** (2002).

3. Winfree, E., Liu, F. R., Wenzler, L. A. & Seeman, N. C. Design and self-assembly of two-dimensional DNA crystals. *Nature* **394** (1998).

4. Olenyuk, B., Whiteford, J. A., Fechtenkötter, A. & Stang, P. J. Self-assembly of nanoscale cuboctahedra by coordination chemistry. *Nature* **398** (1999).

5. Rothemund, P. W. K. Folding DNA to create nanoscale shapes and patterns. *Nature* **440** (2006).

6. Bowden, N., Terfort, A., Carbeck, J. & Whitesides, G. M. Self-assembly of mesoscale objects into ordered two-dimensional arrays. *Science* **276** (1997).

7. Bowden, N., Arias, F., Deng, T. & Whitesides, G. M. Self-assembly of microscale objects at a liquid/liquid interface through lateral capillary forces. *Langmuir* **17** (2001).

8. Srinivasan, U., Liepmann, D. & Howe, R. T. Microstructure to substrate self-assembly using capillary forces. *J. MEMS* **10** (2001).

9. Chung, J. H., Zheng, W., Hatch, T. J. & Jacobs, H. O. Programmable reconfigurable self-assembly: Parallel heterogeneous integration of chip-scale components on planar and nonplanar surfaces. *J. MEMS* **15** (2006).

10. Chung, S. E., Park, W., Shin, S., Lee, S. A. & Kwon, S. Guided and fluidic self-assembly of microstructures using railed microfluidic channels. *Nature Mater.* **7** (2008).

11. Yeh, H. J. & Smith, J. S. Fluidic Self-Assembly for the integration of GaAs Light-Emitting Diodes on Si substrates. *IEEE Photon. Technol. Lett.* **6** (1994).

12. Zheng, W. & Jacobs, H. O. Shape-and-solder-directed self-assembly to package semiconductor device segments. *Appl. Phys. Lett.* **85** (2004).

13. Golosovsky, M., Saado, Y. & Davidov, D. Self-assembly of floating magnetic particles into ordered structures: A promising route for the fabrication of tunable photonic band gap materials. *Appl. Phys. Lett.* **75** (1999).

14. Tanase, M. *et al.* Magnetic trapping and self-assembly of multicomponent nanowires. *J. App. Phys.* **91** (2002).

15. Glotzer, S. C., Solomon, M. J. & Kotov, N. A. Self-assembly: From nanoscale to microscale colloids. *AIChe Journal* **50** (2004).

16. Li, Y. G. *et al.* Controlled assembly of dendrimer-like DNA. *Nature Mater.* **3** (2004).

17. Yan, H., Park, S. H., Finkelstein, G., Reif, J. H. & LaBean, T. H. DNA-templated self-assembly of protein arrays and highly conductive nanowires. *Science* **301** (2003).

18. Chen, H. L., Schulman, R., Goel, A. & Winfree, E. Reducing facet nucleation during algorithmic self-assembly. *Nano Lett.* **7** (2007).

19. Murata, S., Kurokawa, H. & Kokaji, S. in *Proc. IEEE International Conference on Robotics and Automation (ICRA94).*

20. White, P., Kopanski, K. & Lipson, H. in *Proc. IEEE International Conference on Robotics and Automation (ICRA04).* 2888-2893.

21. Griffith, S., Goldwater, D. & Jacobson, J. M. Robotics - Self-replication from random parts. *Nature* **437** (2005).

22. Goldstein, S. C., Cambell, J. D. & Mowry, T. C. Programmable Matter. *Computer* **38** (2005).

23. Klavins, E. Programmable Self-Assembly. *IEEE Control Systems Magazine* **27** (2007).

24. Lahann, J. *et al.* A reversibly switching surface. *Science* **299** (2003).

25. Vasudev, A. & Zhe, J. A capillary microgripper based on electrowetting. *Appl. Phys. Lett.* **93** (2008).

26. Sharma, R. Thermally controlled fluidic self-assembly. *Langmuir* **23** (2007).

27. Xiong, X. R. *et al.* Controlled multibatch self-assembly of microdevices. *J. MEMS* **12** (2003).

28. Pelesko, J., Ch. Chapter 7, (Chapman & Hall/CRC, 2007).

29. Wen, W. J., Huang, X. X., Yang, S. H., Lu, K. Q. & Sheng, P. The giant electrorheological effect in suspensions of nanoparticles. *Nature Mater.* **2** (2003).

30. Tolley, M. T., Krishnan, M., Erickson, D. & Lipson, H. *Dynamically programmable fluidic assembly* (2008).

31. Wanka, G., Hoffmann, H. & Ulbricht, W. Phase-diagrams and aggregation behavior of poly(oxyethylene)-poly(oxypropylene)-poly(oxyethylene) triblock copolymers in aqueous-solutions. *Macromolecules* **27** (1994).

32. Stoeber, B., Yang, Z. H., Liepmann, D. & Muller, S. J. Flow control in microdevices using thermally responsive triblock copolymers. *J. MEMS* **14** (2005).

33. Erickson, D., Sinton, D. & Li, D. Joule heating and heat transfer in poly(dimethylsiloxane) microfluidic systems. *Lab on a Chip* **3** (2003).

34. Tolley, M. T., Baisch, A., Krishnan, M., Erickson, D. & Lipson, H. in *Proc. 21st IEEE Int. Conf. Micro Electro Mechanical Systems (MEMS).* (eds O. Brand & Y. Zohar) 1073-1076.

CHAPTER 4

OPTO-THERMORHEOLOGICAL FLOW MANIPULATION*

4.1 Abstract

Optical methods for microfluidic flow manipulation offer a flexible, non-contact technique for both fluid actuation and valving. At present however, such techniques are limited by their high laser power requirements, low achieved flow rates or poor valve switching times. Here we demonstrate a microfluidic valving technique based on opto-thermorheological manipulation using a low power, 40 mW laser with switching times on the order of a second at high flow rates of 1 mm/s. In our approach a laser beam incident on an absorbing substrate is used to locally heat a thermorheological fluid flowing in a microfluidic channel. The resulting gelation in the heated region creates a reversible fluid valve.

---

* Reprinted with permission from Krishnan, M., Park, J. and Erickson, D., "Optothermorheological flow manipulation", Optics Letters, **34** (13), 1976, 2009. Available online at http://www.opticsinfobase.org.

4.2 Introduction

The ability to dynamically control and manipulate flow in microchannels is crucial to the development of viable lab on chip technologies. Various actuation methods based on electrokinetics[1] and pressure driven flow[2] as well as flow valving techniques using pneumatic[2,3], ferrofluid[4,5] and polymer gel[6-8] based valves have been explored. A major issue with all these approaches is that the valving structures need to be designed, fabricated and placed on the microchip *a priori*. As such the microchannel network is essentially fixed and on-the-fly flow reconfiguration is not possible. Fabrication methods are usually fairly complex (such as patterning multilayer soft lithography systems or on chip heaters) and there is need for extensive interfacing with the external environment (for example with pneumatic lines or electrical connections). The issue of reconfigurability has been long addressed in electronic devices with field programmable gate arrays (FPGAs)[9] and even droplet microfluidic systems[10,11], but is largely unexplored in channel based microfluidic systems.

The recent interest in optofluidics[12,13] has resulted in techniques using laser irradiation to manipulate fluids that could offer a solution[14-19]. For example, radiation pressure at the interface of two fluids has been used to deform the interface and produce microjets[14] of up to 100 μm length, though the power requirement for this was high (~ 1 Watt). Laser induced heating has been used to drive the motion of droplets by thermocapillary actuation[16,17], though this is restricted to two phase flow systems. Photothermal nanoparticles at a fluid air interface have been used to drive flow by optical to hydrodynamic energy conversion[15] with flow rates on the order of ten to five hundred microns per second in 10 - 100 μm wide channels. Recently, a laser scanning

microscope has been used for fluidic actuation[18], where the repetitive motion of an infrared laser results in heating and a subsequent viscosity change in water, driving flows with a velocity of 150 μm/s in channels of height 10 μm with a resolution of 2 μm. These optical manipulation techniques have advantages over more traditional methods being non-contact methods of actuation, flexible with minimum requirements for predefined geometries and allowing independent simultaneous actuation at multiple locations. At present however they are largely limited by the slow flow rates achieved (about a few hundred microns per second) and/or their high power requirements (~ 1 Watt).

One method to improve these results is through the use of light-actuated polymer gels[20-23]. Polymer gels that undergo light induced phase change, either due to laser heating or a photoreaction in the gel, have been used to develop microfluidic valves. Although these techniques overcome some of the interfacing issues of pneumatic and electronic based valves, many of these techniques still require fixed, prefabricated geometries. To address this, Shirasaki et al.[21] have developed a technique that uses laser induced infrared heating to directly gel and rapidly valve a thermally responsive polymer solution in a 30 μm wide, 5 μm tall channel, though with high power requirements (~ 1 Watt). Sugiura et al.[23] have developed a technique that utilizes light irradiation of a photoresponsive hydrogel sheet to dynamically define channel geometries and valves on-the-fly having a resolution of 10 μm. This robust and flexible fluid manipulation method is however limited by the poor switching times of their structures (taking minutes to open and an hour to close).

In our work here, we present a rapid, low power technique to carry out flexible fluid manipulation by light irradiation. This technique relies on the use of a thermorheological fluid that undergoes a reversible sol-gel transition on heating. A schematic describing our approach is shown in Figure 4.1. Our chip consists of an upper part with a patterned microchannel bonded to a substrate with a coating that absorbs light at specific wavelengths. Thus by selectively illuminating the absorbing substrate with laser light at these wavelengths, optical energy is converted to thermal energy to gel the thermorheological fluid flowing in the channel. A similar approach has been demonstrated by Boyd *et al*[24] where the plasmon resonance of a metallic substrate is used to transfer optical energy to thermal energy. This opto-thermorheological method offers the flexibility to manipulate fluids without predefined valve geometries. We show switching times on the order of a second using a low power 40 mW laser.

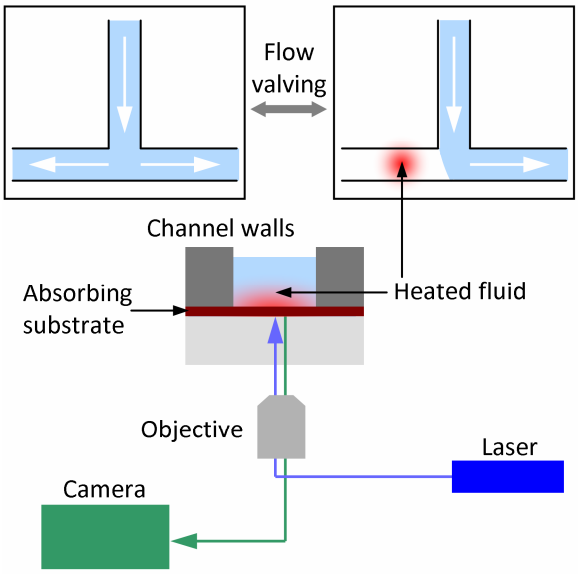

Figure 4.1. Schematic demonstrating valving technique with a laser and a microfluidic chip with an absorbing substrate.

4.3 Methods

Opto-thermorheological valving is demonstrated here in a T-shaped microfluidic channel as shown in Figure 4.2a (Media 1). Initially, the flow rate through each of the bifurcating channels was the same. On illuminating one of the channels with laser light through a 20X objective (405 nm, 40 mW power, spot size ~ 10 μm), we were able to reduce and eventually stop the flow in this channel and redirect it to the other one. The same objective was used to image the sample, and flow was visualized using 1.5 μm silica particles (Duke Scientific). As shown in Figure 4.2b (Media 1), when a non-absorbing plain glass substrate was used no such valving was observed. The thermorheological fluid used here is a 15% (w/w) aqueous solution of Pluronic F127 (BASF) with a gelation temperature of approximately 30 °C[25]. The microfluidic channels were fabricated using standard soft lithography techniques with poly(dimethylsiloxane) (PDMS) (Ellsworth Adhesives). We used two different absorbing substrates; a plain glass substrate with gold sputter deposited on it (10 - 20 nm) and a cover slip coated with indium tin oxide (ITO) (120 – 160 nm, SPI Supplies) as well as a non-absorbing plain glass substrate for control experiments. The transmission of the sputtered gold substrate was measured to be 0.25 (transmission of 56%), for the ITO coated substrate was 0.34 (transmission of 46%) and for the plain glass substrate was 0.13 (transmission of 74%) at 405 nm, indicating that the ITO had the best absorption of the three substrates. Two channels widths of 25 and 50 μm were used with the height constant at 25 μm. The results in Figure 4.2a (Media 1) are for an ITO coated substrate with a channel width of 50 μm.

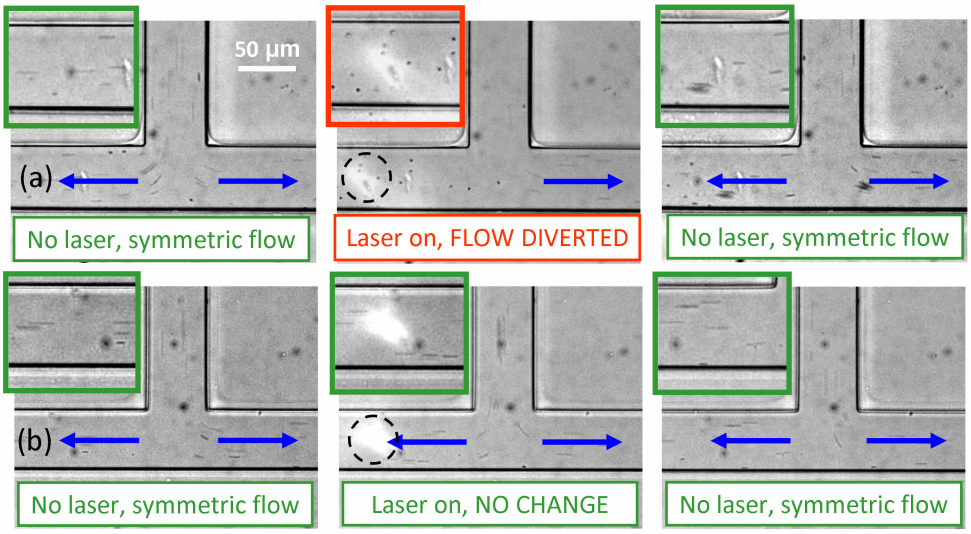

Figure 4.2. Demonstration of valving in a microfluidic channel (Media 1) (a) ITO coated substrate (valving occurs). (b) Plain glass substrate (no valving). The insets show a zoomed up view of the flow in the valved channel. The black dashed circles indicate the position of the laser spot.

4.4 Results

The results from characterization experiments are shown in Figure 4.3. We varied the inlet flow velocity into a bifurcating channel and measured the final velocity in the valved channel after turning the laser on as shown in Figure 4.3a. The control experiment here was with a glass substrate which showed no valving. The low Peclet number in our experiments (about 0.2) means that conductive heat transfer tends to dominate over convective or flow effects. Thus flow rate is not expected to affect the valving efficiency, resulting in the near linear response of valved velocity to inlet flow rate seen here. In general we found that better valving was achieved for the wider channels. We also measured the time response as shown in Figure 4.3b and were able to both turn the valve on and off at timescales on the order of a second. The relaxation time for the formation and dissociation of the gel itself is on the order of

milliseconds[26]; thus the time required for heat transfer is the important time scale here. The flow measurements were carried out by analyzing the paths of the silica beads in the pluronic solution using ImageJ.

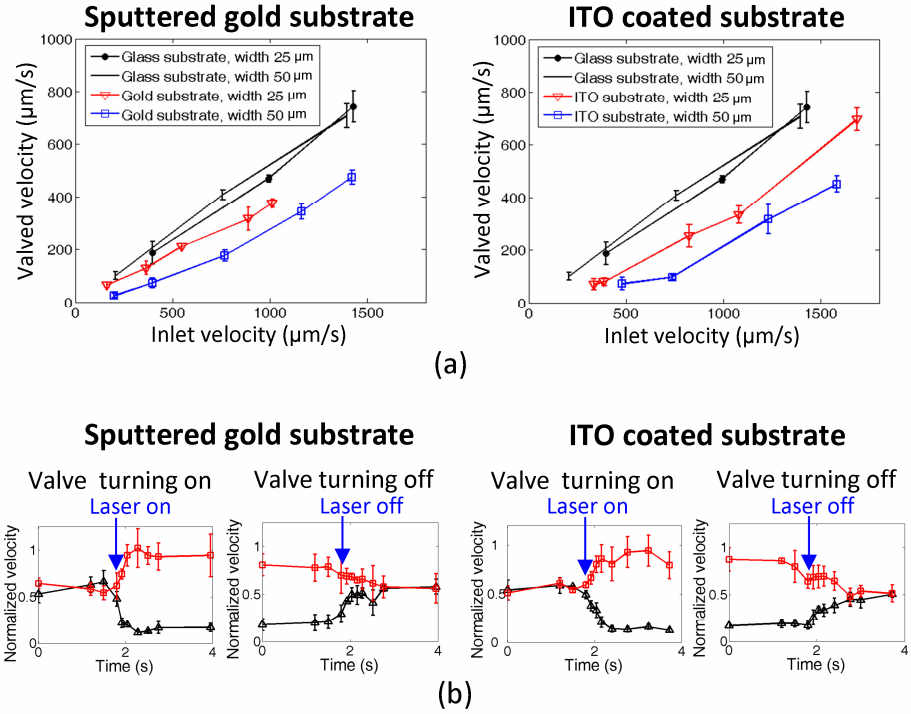

Figure 4.3. Flow measurements in channel (a) Valved flow velocity as a function of inlet velocity for sputtered gold and ITO coated substrates. (b) Time response of valving for sputtered gold and ITO coated substrates (triangles indicate valved channel, squares indicate other channel). The results shown here are 50 µm for wide channels.

Finally, in situ temperature measurements using Rhodamine B[27] were also carried out as shown in Figure 4.4. We used Y-shaped channels here instead of T-shaped channels due to experimental convenience at the time though this makes little difference at these low Reynolds numbers where the effect of bend angle on pressure drop (head loss) is negligible. These results do show channel temperatures on the order of the sol-gel transition temperature; however, as was seen in Figure 4.3a, flow

in the valved channel was not completely stopped. We expect this is because the yield stress of the gel in the channel is not sufficient to withstand the applied pressure. We attempted to improve valving by increasing the beam power and also changing the beam waist by using different magnification objectives. This resulted in either too much heating and bubble formation due to evaporation or too little heating and no subsequent gelation. These temperature measurements also show that the ITO coated substrate had slightly higher temperatures over a wider region of the channel compared to the gold coated substrate as expected. The 25 µm channel with the ITO coated substrate had a higher temperature compared to the corresponding 50 µm channel which is due to the lower thermal conductivity of the PDMS sidewalls (~ 0.18 W/mK) compared to the aqueous pluronic solution in the channel (~ 0.6 W/mK)[27]).

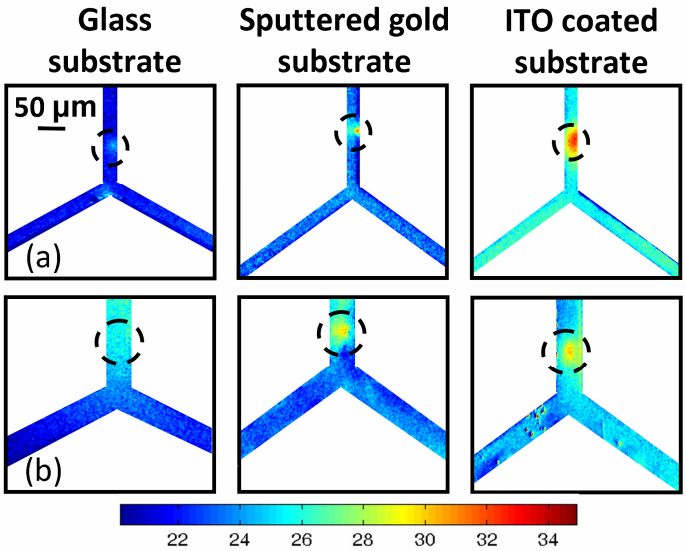

Figure 4.4. Temperature measurements (a) Channel width of 25 µm. (b) Channel width of 50 µm. The region of heating by the laser is indicated by black dashed circles.

Here we have shown the use of an opto-thermorheological technique to carry out valving in a microfluidic channel. We used a low power 40 mW laser and obtained valve switching times on the order of a second. Such a technique could be extended from simple valving to reconfiguring entire channel geometries by illuminating larger regions of the chip either using a mask or a digital micromirror display.

4.5 Acknowledgements

This work was supported by the Defense Advanced Research Projects Agency (DARPA), Defense Sciences Office (DSO) under the Programmable Matter program.

REFERENCES

1. Li, D. Q. *Electrokinetics in Microfluidics*. (Elsevier Academic, 2004).

2. Unger, M. A., Chou, H. P., Thorsen, T., Scherer, A. & Quake, S. R. Monolithic microfabricated valves and pumps by multilayer soft lithography. *Science* **288** (2000).

3. Thorsen, T., Maerkl, S. J. & Quake, S. R. Microfluidic large-scale integration. *Science* **298** (2002).

4. Hartshorne, H., Backhouse, C. J. & Lee, W. E. Ferrofluid-based microchip pump and valve. *Sensors and Actuators B-Chemical* **99** (2004).

5. Yamahata, C. *et al.* Plastic micropump with ferrofluidic actuation. *J. Microelectromech. Syst.* **14** (2005).

6. Beebe, D. J. *et al.* Functional hydrogel structures for autonomous flow control inside microfluidic channels. *Nature* **404** (2000).

7. Niu, X. Z., Wen, W. J. & Lee, Y. K. Electrorheological-fluid-based microvalves. *Appl. Phys. Lett.* **87** (2005).

8. Stoeber, B., Yang, Z. H., Liepmann, D. & Muller, S. J. Flow control in microdevices using thermally responsive triblock copolymers. *J. Microelectromech. Syst.* **14** (2005).

9. Rose, J., Elgamal, A. & Sangiovannivincentelli, A. in *Proc. IEEE.* 1013-1029 (IEEE).

10. Joanicot, M. & Ajdari, A. Applied physics - Droplet control for microfluidics. *Science* **309** (2005).

11. Pollack, M. G., Shenderov, A. D. & Fair, R. B. Electrowetting-based actuation of droplets for integrated microfluidics. *Lab Chip* **2** (2002).

12. Monat, C., Domachuk, P. & Eggleton, B. J. Integrated optofluidics: A new river of light. *Nat. Photonics* **1** (2007).

13. Psaltis, D., Quake, S. R. & Yang, C. H. Developing optofluidic technology through the fusion of microfluidics and optics. *Nature* **442** (2006).

14. Casner, A. & Delville, J. P. Laser-induced hydrodynamic instability of fluid interfaces. *Phys Rev Lett* **90** (2003).

15. Liu, G. L., Kim, J., Lu, Y. & Lee, L. P. Optofluidic control using photothermal nanoparticles. *Nature Materials* **5** (2006).

16. Baroud, C. N., de Saint Vincent, M. R. & Delville, J. P. An optical toolbox for total control of droplet microfluidics. *Lab Chip* **7** (2007).

17. Ohta, A. T., Jamshidi, A., Valley, J. K., Hsu, H. Y. & Wu, M. C. Optically actuated thermocapillary movement of gas bubbles on an absorbing substrate. *Appl. Phys. Lett.* **91** (2007).

18. Weinert, F. M. & Braun, D. Optically driven fluid flow along arbitrary microscale patterns using thermoviscous expansion. *J. Appl. Phys.* **104** (2008).

19. Delville, J. P. *et al.* Laser microfluidics: fluid actuation by light. *J. Opt. A-Pure Appl. Opt.* **11** (2009).

20. Sershen, S. R. *et al.* Independent optical control of microfluidic valves formed from optomechanically responsive nanocomposite hydrogels. *Adv. Mater.* **17** (2005).

21. Shirasaki, Y. *et al.* On-chip cell sorting system using laser-induced heating of a thermoreversible gelation polymer to control flow. *Analytical Chemistry* **78** (2006).

22. Sugiura, S. *et al.* Photoresponsive polymer gel microvalves controlled by local light irradiation. *Sens. Actuator A-Phys.* **140** (2007).

23. Sugiura, S. *et al.* On-demand microfluidic control by micropatterned light irradiation of a photoresponsive hydrogel sheet. *Lab Chip* **9** (2009).

24. Boyd, D. A., Adleman, J. R., Goodwin, D. G. & Psaltis, D. Chemical separations by bubble-assisted interphase mass-transfer. *Analytical Chemistry* **80** (2008).

25. Wanka, G., Hoffmann, H. & Ulbricht, W. Phase-diagrams and aggregation behavior of poly(oxyethylene)-poly(oxypropylene)-poly(oxyethylene) triblock copolymers in aqueous-solutions. *Macromolecules* **27** (1994).

26. Prudhomme, R. K., Wu, G. W. & Schneider, D. K. Structure and rheology studies of poly(oxyethylene-oxypropylene-oxyethylene) aqueous solution. *Langmuir* **12** (1996).

27. Erickson, D., Sinton, D. & Li, D. Q. Joule heating and heat transfer in poly(dimethylsiloxane) microfluidic systems. *Lab Chip* **3** (2003).

CHAPTER 5

OPTICAL IMAGE GUIDED MICROFLUIDIC RECONFIGURATION*

5.1 Abstract

Reconfigurable systems, like the field-programmable gate array in electronics, have numerous advantages including cost, adaptability, robustness, and security. Despite this, few other chip-based technologies have developed equivalently ubiquitous reconfiguration methods. As a first step to applying this paradigm to channel-based microfluidics, we present here a rapid optofluidic technique to create, move, and remove arbitrary solid regions in a microfluidic flow simply by illumination with an optical pattern. While other techniques have shown the ability to manipulate individual particles using spatial light modulation, we demonstrate here the ability to create reconfigurable flow pathways and build morphable channel structures. These structures can be modified on the order of seconds using a combined photothermal and thermo-rheological effect. In addition to characterizing the effect, we also apply this technique to create dynamic traps for biomolecules, and demonstrate trapping of λ-DNA molecules and nanoparticles, with a 25 fold suppression of diffusion.

---

* Submitted for publication to Proceedings of the National Academy of Sciences of the USA by Krishnan, M. and Erickson, D., "Optical image guided microfluidic reconfiguration", June 3 2011.

5.2 Introduction

The ability to dynamically control and manipulate fluid flow is crucial to the development of nearly all lab-on-chip technologies[1]. Although the implementation can vary dramatically, these devices can broadly be categorized as being either microchannel based, in which micro- and nanoscale fluidic networks are used to transport and process ultra-small sample volumes[2,3], or discrete droplet translocation based, whereby electric fields or thermal gradients are used to transport relatively large volume droplets through an arbitrary path[4-6]. Discrete droplet based microfluidic systems are fundamentally reconfigurable as it is relatively straightforward to fabricate a chip with an array of electrodes that enables one to move the droplet along any arbitrary path. These reconfigurable transport pathways allow one to change the analysis performed on the droplet based on upstream results, correct for manufacturing flaws by routing droplets along alternate paths, and lower overall costs since chips are versatile and can perform a number of different applications.

At present however the vast majority of microfluidics is done using traditional "channel" based chips. This is because most of the analysis techniques of interest are specifically suited to such systems (*e.g.* chromatographic separations, electrokinetic concentration and molecular filtering) and due to additional thermal-fluid transport advantages (*e.g.* confinement enhanced diffusive transport to molecular sensors and greater surface area to volume ratio for enhanced heat transfer). Despite these advantages channel based approaches have a significant limitation in that all the flow control structures need to be designed, fabricated and placed on the microchip *a priori*. As such the microchannel network is essentially fixed and the advantages of on-the-fly

flow reconfiguration cannot be exploited as with droplet methods. Additionally the fabrication methods involved are usually somewhat complex and extensive interfacing is needed between the chip and the external environment (*e.g.* pneumatic lines or electrical connections for flow valving).

The field of optofluidics[7,8] offers a potential solution to these issues. Various optofluidic manipulation techniques have been recently developed that could enable reconfigurable microfluidic systems[9-13]. For instance, Chiou *et al.*[11] used a spatial light modulator to manipulate cells using optical images. Their approach used optically induced dielectrophoresis to move objects within a fluid but did not carry out flow manipulation or channel reconfiguration. Photothermal nanoparticles at a fluid air interface have been used to actuate fluid motion via optical to thermal to hydrodynamic energy conversion[12] achieving flow velocities on the order of 10 - 500 μm/s. Fluidic actuation has also been achieved using a laser scanning microscope[14] where the repetitive motion of an infrared laser resulted in heating and a subsequent viscosity change in water, driving flows with a velocity of about 150 μm/s. Polymer gels that undergo a light induced phase change, either directly through a photoreaction occurring in the gel or due to heating by a laser, have also been used to develop microfluidic valves and reconfigurable microchannels[15-18]. For example, Sugiura *et al.*[18] developed a technique that utilizes light irradiation of a photoresponsive hydrogel sheet to dynamically define and reconfigure channel geometries and valves on-the-fly. These optofluidic manipulation techniques have many advantages in that they are non-contact in nature, require little on-chip infrastructure, and take advantage of the relative ease with which light patterns can be spatially modulated. At present however

these approaches are either unable to fundamentally reconfigure the flow systems or have engineering limitations such as slow flow rates (on the order of a few hundred micrometers per second) and/or poor switching times (on the order of tens of minutes to hours).

5.3 Technique

Here we demonstrate the use of light to trigger reversible structural changes in a fluid contained within a microfluidic environment. This effect consists of two coupled processes, as shown in Figure 5.1a: (1) *Photothermal Conversion*, where optical energy from a patterned light source is converted to a local thermal field on chip, through the use of an absorbing substrate and (2) *Thermo-rheological Conversion*, where the localized thermal field triggers a reversible change in the rheology of a polymer solution flowing through the microfluidic device, resulting in the creation of local regions of high yield strength that behave as wall-like structures. The polymer solution chosen for our purposes undergoes a reversible sol-gel conversion upon being heated to a critical temperature, transitioning from a low viscosity fluid to a high yield strength gel. The particular class of gels we use for our experiments are aqueous solutions of triblock copolymers of the form poly(ethylene oxide)$_x$ – poly(propylene oxide)$_y$ – poly(ethylene oxide)$_x$[19,20]. The optical and subsequently the thermal field on chip can be modulated through dynamic photomasking (See Figure 5.6 for a picture of the experimental setup); thus it is possible to arbitrarily create and reconfigure higher temperature regions that behave as channel walls, and lower temperature regions that form microchannel networks having low viscosity fluid flow.

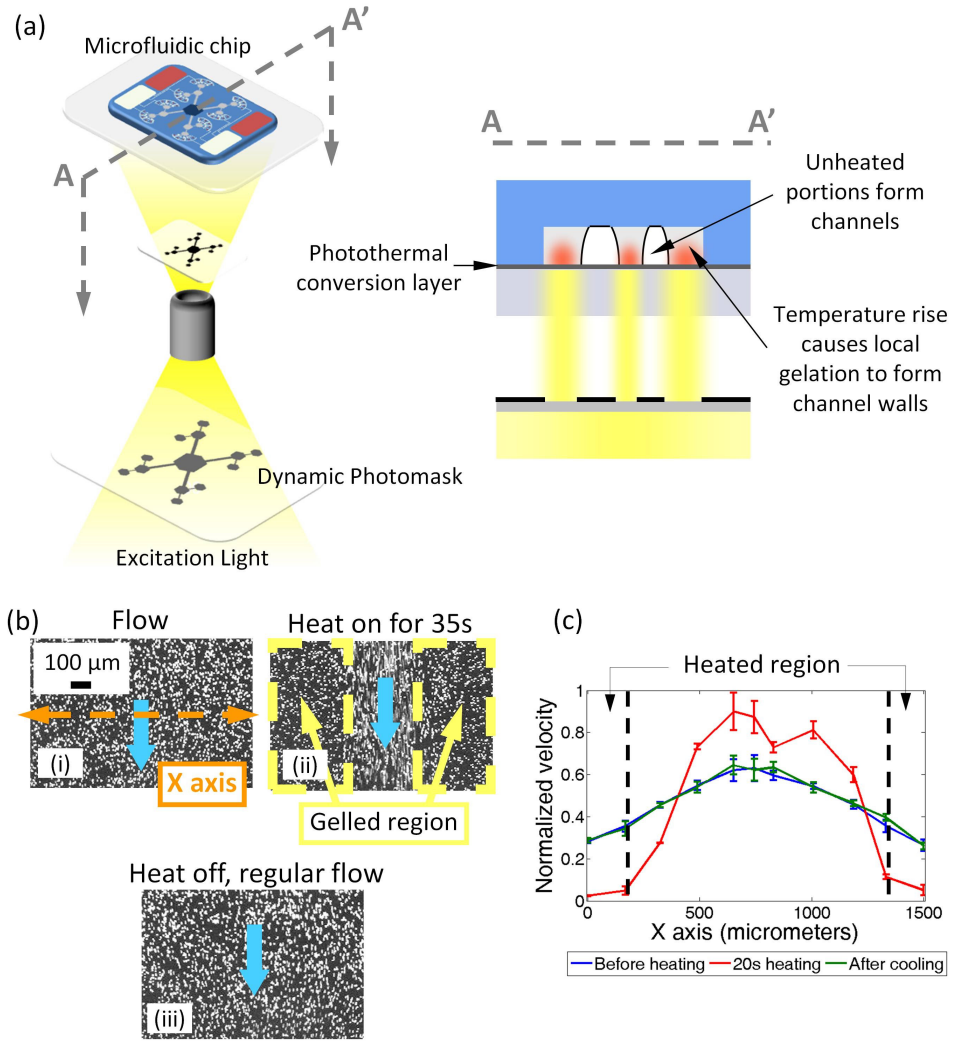

Figure 5.1. Optical image guided microfluidic reconfiguration (a) Schematic demonstrating our technique. (b) Creation of narrow straight channel within a larger microfluidic chamber using this approach. (c) The resulting velocity profile shows gelation along the sides of the chamber that have been heated. The original flow profile is accurately recreated on turning the illumination off. Error bars in the figure indicate sample standard deviation.

5.4 Methods

5.4.1 Materials

The Pluronic F127 particles (BASF) were added to DI water to make the 14.8% (w/w) pluronic solution, followed by gentle agitation, and left overnight in the

refrigerator. For trapping experiments with 210 nm nanoparticles (red fluorescent, Duke Scientific), a 30% (w/w) solution of ethanol (Reagent Alcohol, BDH) in DI water used to make up a 12% (w/w) solution of pluronic, while for the experiments with λ-DNA, the 30% (w/w) solution of ethanol was made in Tris-EDTA buffer instead of DI water. The buffer consisted of 10 mM Tris Base (J.T. Baker), 1 mM EDTA (Fisher), and 10 mM sodium chloride (Mallinckrodt) at a pH of 7.8. For the flow experiments, visualization was carried out using 3.2 μm red fluorescent polystyrene particles (Duke Scientific). For trapping experiments with DNA, the λ-DNA molecules (New England BioLabs) were stained with YOYO-1 intercalating dye (Molecular Probes) for observation using traditional fluorescence microscopy. For temperature measurements, Rhodamine B was dissolved in DI water at a concentration of 1mM and refrigerated. The dye was diluted to a 50 μM concentration using 50 mM of carbonate buffer at a pH of 9.6 (Sigma Aldrich) prior to use. Pluronic F127 was then added to this solution to make a 14.8% (w/w) solution. Microfluidic chips were fabricated using PDMS (Ellsworth Adhesives). The photothermal absorbing layer was made with a mixture of PDMS and carbon black (Vulcan XC72-R, Cabot Corp).

5.4.2 Fabrication

The fluid layer of the microfluidic device was formed by making a silicon master by silicon etching using a Bosch etching tool. A 5:1 ratio by weight of PDMS A and PDMS B was poured over this mold and cured for 2 hours in an 80 °C convection oven. The photothermal absorption layer consisted of a mixture of carbon black, PDMS A and PDMS B in the ratio 0.01:1:0.05 by weight. (See Supplementary

Information, 5.8.1 for details). The fluidic layer was bonded to the substrate by plasma cleaning both layers, bonding them and leaving them overnight in a convection oven at 80 °C.

5.4.3 Experimental Setup

The experimental setup consisted of a modified off-the-shelf projector system (InFocus LP435z) from which we removed the projection lens, and a lens and mirror system (components obtained from Thorlabs,Inc.) to relay the image to the chip. The light pattern was created using Microsoft PowerPoint, and usually consisted of white images. The chip was placed upside down on an inverted microscope (Olympus IX71) and data recorded using a CCD camera (Hamamatsu, ORCA-ER). Fluidic flow was driven with a syringe pump (Model NE-1000, New Era Pump Systems, Inc.).

5.5 Results

Figures 5.1b demonstrates the creation of a channel within a larger microfluidic chamber using this technique. A narrow straight channel was created within the larger chamber by shining an image along the sides of the chamber. Although timescales will be better quantified later on in this paper, it can be seen that the initial flow pattern was regained within a few seconds of turning the optical image off demonstrating the ability to rapidly reconfigure the flow system (See Supplementary Information, Movie S1 for a video of such an experiment). The velocity profile across the centerline of the chamber before heating, after 20s of heating, and on cooling is shown in Figure 5.1c. As can be seen the flow is stopped in the heated regions and the

original flow profile is completely reproduced upon turning the thermal field off. Flow analysis was done using the software ImageJ. The microfluidic chip used in these experiments was fabricated using poly(dimethylsiloxane) or PDMS with standard soft lithography techniques[21]. The absorbing substrate was created using carbon black, which acts as an efficient photothermal conversion layer, dispersed in a PDMS solution and spun on a glass substrate coated with a thin layer of PDMS to enhance the heat transfer characteristics of the chip (See Supplementary Information, 5.8.1 and Figures 5.7 and 5.8 for a description of the fabrication process and characterization studies of the absorber layer). The polymer solution used in most of our experiments was a 14.8 % (w/w) aqueous solution of Pluronic F127 (BASF) with a composition of poly(ethylene oxide) $_{106}$ – poly(propylene oxide) $_{70}$ – poly(ethylene oxide) $_{106}$, which has been used in the past to create fluidic microvalves[17,22] and has a gelation temperature close to 30°C[20] and a gel yield stress on the order of a few hundred pascals[19].

Figure 5.2a shows results from heat transfer simulations carried out in order to determine the optimal conditions for triggering this effect (See Supplementary Information, 5.8.2 for details of the numerical simulations). We considered absorbing substrates of varying thickness from 25 - 200 μm and absorption coefficients, α of 0.04 μm^{-1}, 0.07 μm^{-1} and 0.18 μm^{-1} which could be obtained by varying the concentration of carbon black in our substrates. The heated region of the chip consisted of a 100 μm X 100 μm central region within the fluidic chamber. In general, the peak temperature was found to decrease with absorber thickness, though some variation was observed at 50 μm and below. This can be explained from the inset in

Figure 5.2a(ii) which shows the volumetric heat rate generated across the thickness of the absorber (See Supplementary Information, 5.8.2 for details on calculating the volumetric heat rate). For α = 0.04 μm^{-1}, the characteristic decay length of the exponential describing the volumetric heat rate is 25 μm while for α = 0.07 μm^{-1}, the characteristic length is 15 μm and α = 0.18 μm^{-1} it is 5.5 μm. Thus, for absorber thicknesses on the order of or less than the decay length, the corresponding peak temperatures are lower. Figures 5.2a(iii) and 5.2a(iv) show typical temperature profiles obtained from these simulations. The temperature profile along the x-axis shows peak temperatures in the heated regions, but has strong diffusive tails that extend beyond the heated regions which correspond well to the temperatures needed for gelation. Additionally, the temperature profile is not observed to vary significantly along the z-axis indicating fairly uniform heating across the height of the chamber.

To characterize the opto-thermal behavior of this system, we carried out temperature measurements using Rhodamine B which belongs to a class of fluorescent dyes whose quantum yield is strongly dependent on temperature. It is possible to carry out *in situ* temperature measurements by observing the relative spatial and temporal changes in the local intensity of the dye using fluorescence based imaging[23,24]. Figure 5.2b shows results from such a set of temperature measurements which is a spatial map of the temperature rise in a microfluidic chamber as part of the chamber is heated, showing an increase in the peak temperature with heating time. The thermal profile is slightly offset from the image here due to advection in the flow, as a high flow rate was applied to the system to reduce photobleaching effects of the Rhodamine B solution. The observed temperature rise is consistent with that required

for sol-gel transition as discussed above. The effect of thermal diffusion is also seen through the spatial map of the temperature profile, as the region of elevated temperature is seen to extend beyond the region of actual heating. By plotting the average temperature profile in the heated region as a function of time on turning the image off and fitting an exponential curve to the data, we see that the characteristic heating time of the system is given by $\tau = 1/0.5336$ s ~ 2 s. Finally, the experimental temperature profiles were seen to match qualitatively well to those obtained from numerical simulations in Figure 5.2a.

Figure 5.3a probes the thermal cross-talk between multiple heat sources on a chip. The effect of thermal diffusion is clearly seen in the thermal field between the two sources, where the peak temperature obtained in the system is higher than that of a single source described in Figure 5.2b. Additionally, when the two sources were moved closer to each other and the intensity of the image corresponding to the top circle reduced in comparison to the bottom circle (Configuration 2) we found that the overall chamber temperatures increased in comparison to the case where the sources were equally bright and further apart (Configuration 1) and that the region illuminated by the brighter source had a correspondingly higher peak temperature. This demonstrates the ability to directly tune temperature profiles and correspondingly flow fields within the chamber by modulating the geometry and intensity of projected images.

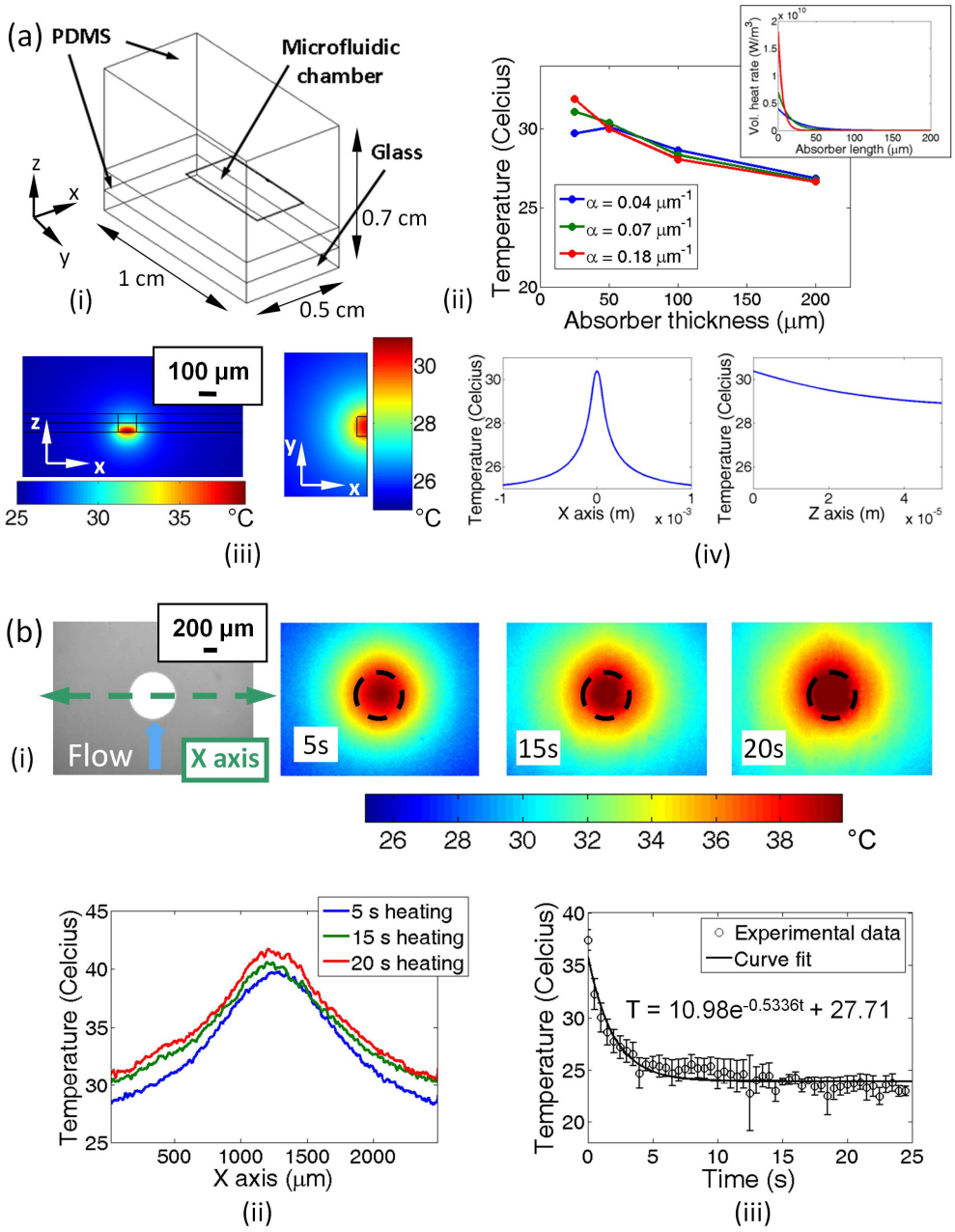

Figure 5.2. Simulations and thermal measurements (a) Simulations showing temperature profile for absorbers of different thicknesses and absorption coefficients. In general, peak chip temperature decreases with absorber thickness. The temperature profile does not vary much along the z-axis, indicating fairly uniform heating across the chip. The peak temperature along the x-axis is obtained in the heated zone (100 μm central region) with strong diffusive tails away from this region. (b) Thermal characterization using Rhodamine B. Temperatures in the illuminated region correspond well to the gelation temperatures of the pluronic solution. The characteristic cooling time was found to be ~ 2s. Error bars indicate sample standard deviation.

We also carried out measurements of the flow profile by seeding the polymer solution with fluorescent polystyrene beads to visualize the flow. We illuminated the microfluidic chamber with images of varying size and observed the resulting gelation profile within the chamber as shown in Figure 5.3b (See Supplementary Information, Movie S2 for a video of the experiment). We found that images below a certain size did not sufficiently heat the chamber and there was no corresponding gelation of the illuminated region. Interestingly, we also found that above a certain size of illuminated region, the pluronic solution in the chamber was heated to a higher temperature reaching a secondary transition temperature, at which point it transformed back from a gelled state to being a low viscosity liquid. This can be explained from the above thermal results where a larger heated region, such as for the case with two sources, reached a higher temperature compared to a smaller heated region; the case with a single source.

Using the optimal thermal configurations determined above, we have used this technique to create complex flow networks as shown in Figure 5.4. Figure 5.4a shows an example of creating reconfigurable flow networks with purely optofluidic actuation. Here, the chamber is illuminated with a square image that is moved across different regions of the chamber. The initial flow is balanced such that each of the three exit channels receives the same volume flow rate. Depending on the location of the image, different flow patterns are generated through the chamber (See Supplementary Information, Movie S3 for a video of the experiment). As can be seen, reconfiguration of the flow field takes place on the order of a few seconds and the initial flow pattern is restored once the optical image is switched off.

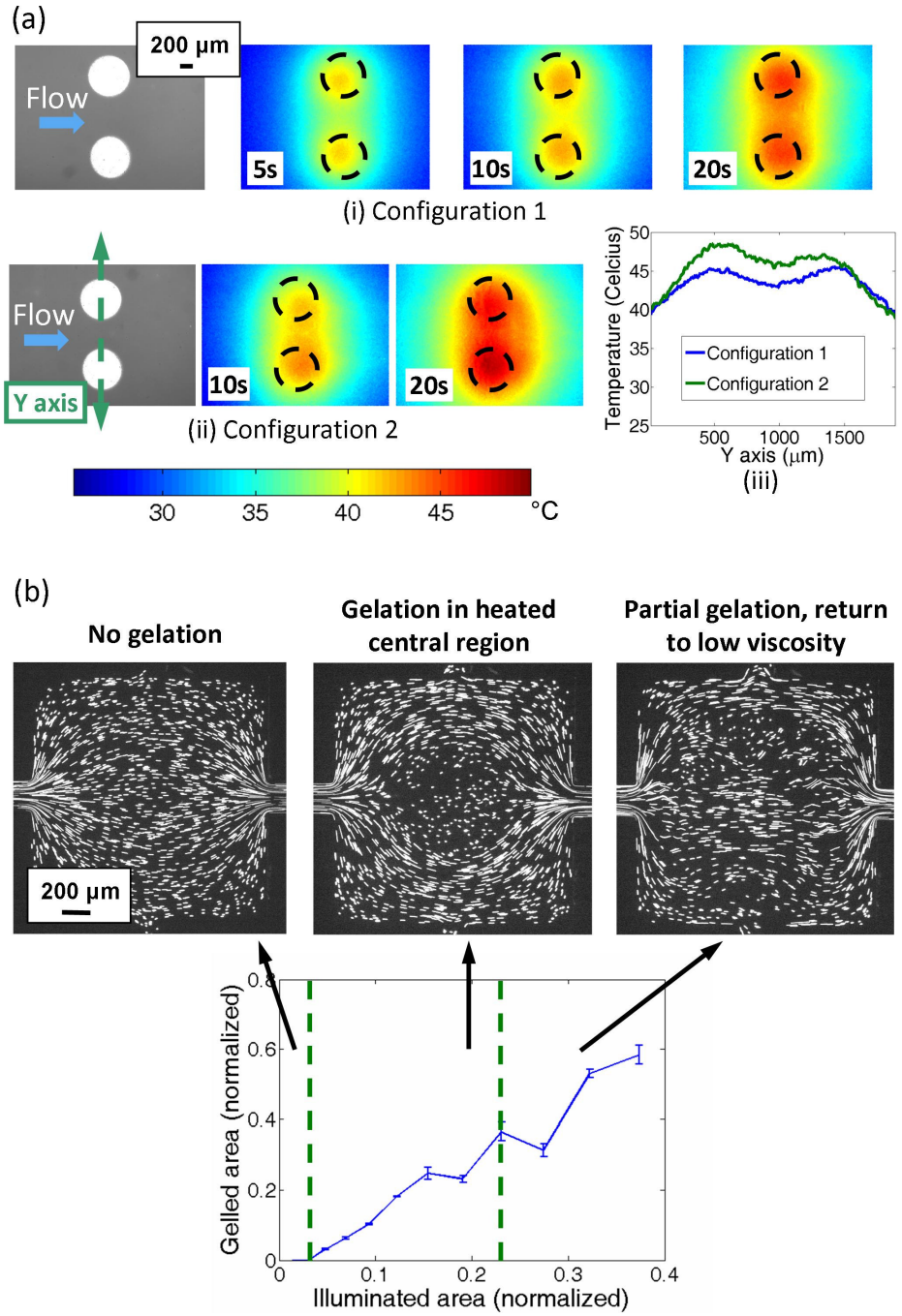

Figure 5.3. Thermal and flow characterization (a) Illumination of microfluidic chip with multiple discrete images. The peak temperatures obtained were higher than for a single image, and were found to be directly related to the geometry and intensity of the images. (b) Flow characterization measurements. Below a certain size of illuminated image, no gelation was seen. On the other hand, images above a threshold (0.23X chip area) heated the chip to a temperature high enough to cause a secondary transition of the pluronic solution back to a low viscosity solution. Error bars in the figure indicate sample standard deviation.

Figure 5.4b shows an experiment where flow is reconfigured using multiple discrete images. Firstly, flow is narrowed using two images on the top and bottom left of the chamber to focus the flow. Secondly, flow is modulated around a rectangular image further downstream of the flow and is directly reconfigured on changing the position of this "obstacle" (See Supplementary Information, Movie S4 for a video of the experiment). We have also used this technique to valve flow through an outlet channel of the chamber (See Supplementary Information, Movie S5 for a video of this experiment).

As an additional application, we demonstrate the ability of this technique to create dynamic traps for biomolecules. A major prohibitive challenge associated with single molecule analysis is the fast diffusion of small molecules in solution making it difficult to observe the target for longer than the time required for it to migrate across a microscope field of view[25]. Depending on the size of the molecule and the numerical aperture of the lens, this can be less than a millisecond. To prolong this observation time, either a physical immobilization technique[26-28] must be used or an external field, such as an optical force[29-32], must be applied. The disadvantage of the former approach is that physical confinement perturbs the natural state of the molecule, while the latter requires either the use of a strong laser beam[29,30] or complex nanofabrication[31,32]. The recently developed opto-electronic tweezer[11] does offer a flexible method to trap and manipulate cells using dielectrophoresis but is difficult to use with smaller species like biomolecules. In contrast to these approaches, our technique directly suppresses biomolecule diffusivity by increasing the local fluid viscosity in the immediate vicinity of the target molecule.

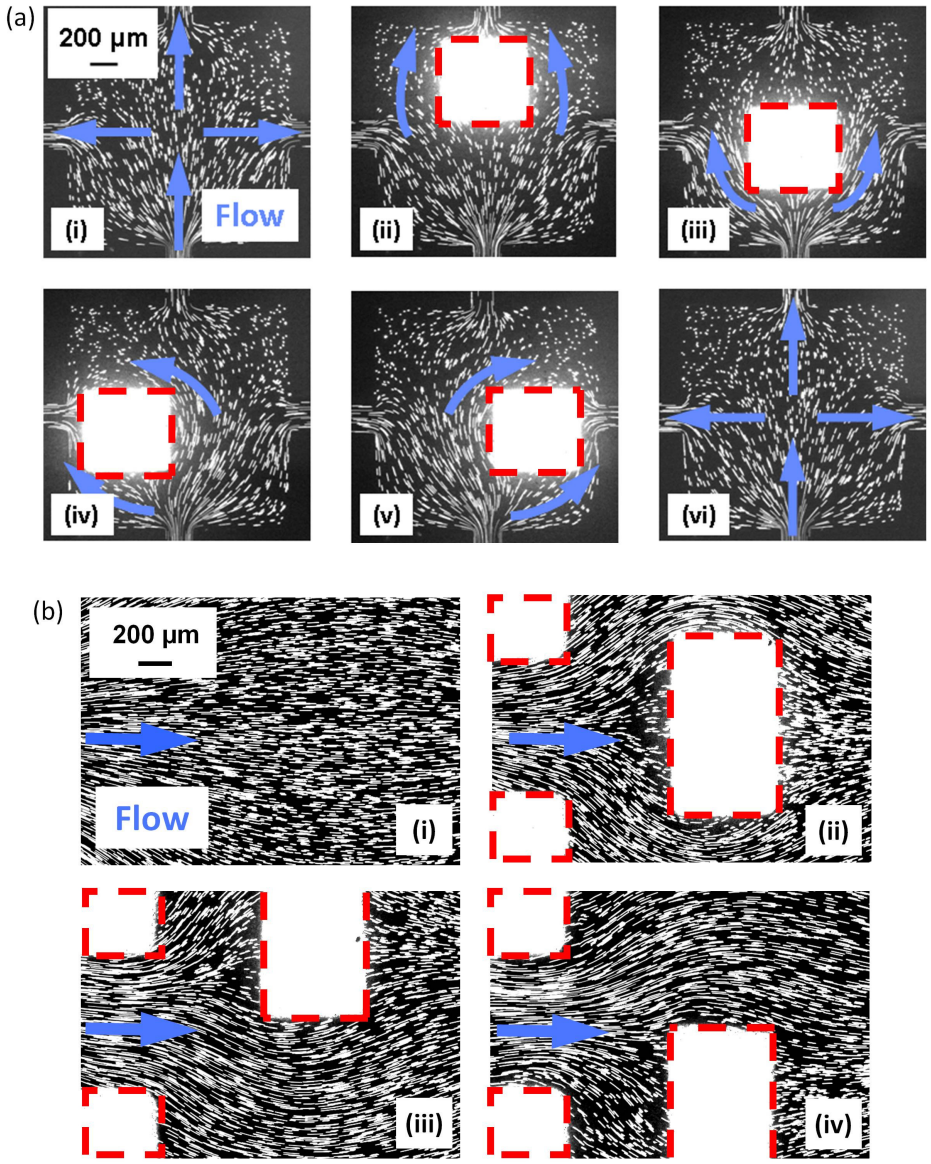

Figure 5.4. Creation of reconfigurable flow patterns (a) Reconfiguration of flow through a microfluidic chamber by manipulation of a square shaped image. (b) Reconfiguration of flow by illumination of multiple discrete images. Flow was reconfigured along the rectangular image in the center of the chamber as it was moved up and down through the chamber. The red dashed lines in the figure indicate the projected images, while the blue arrows show the flow direction.

Figure 5.5a illustrates our approach. As shown, free biomolecules at room temperature undergo significant Brownian motion. Upon illumination with a ring-

shaped image, the solution around the target molecule gels, effectively trapping it. The use of a ring-shaped image facilitates visualization. We modify the pluronic solution used above, so that it forms a soft gel at temperatures above 45°C[33], but has a low viscosity at room temperature, enabling transport of the experimental targets (See Methods section). The temperature of the illuminated region before and after heating was measured to be about 30°C and 65°C respectively. To demonstrate the applicability of this technique to biological species, we carried out experiments with YOYO-1 tagged λ-DNA molecules 48 kilobases long. These experiments were done at a pH where the DNA has been reported to be partially extended[34], which is usually difficult to trap with a tightly focused optical tweezer that can only interrogate a small part of the molecule. The results are shown in Figure 5.5b, where we see the localization of the trajectory of a λ-DNA molecule after heating due to suppression of its diffusivity. We note that it is solely due to the rapidity of the technique that a target molecule of interest can be effectively trapped prior to diffusing away.

To quantify the diffusion suppression, we used fluorescently labeled spherical nanoparticles. The diffusivity of these particles can be calculated by the Stokes-Einstein relation and was found to be about 0.05 $\mu m^2/s$ at room temperature for these types of pluronic solutions[19]. Figure 5.5c shows the suppression of Brownian motion of sample nanoparticle on heating the surrounding region (See Supplementary Information, Movie S6 for a video of this experiment). Figure 5.5d superimposes the trajectory of a sample particle before and after heating, illustrating the localization of the particle, while Figure 5.5e shows the distribution of the incremental displacements of that particle[35] through time intervals of 0.1 s and 0.4 s. The latter figure shows the

broadening with time of the particle displacement away from the center before heating occurred, as expected for a diffusive process, and the localization of the particle around the center after heating.

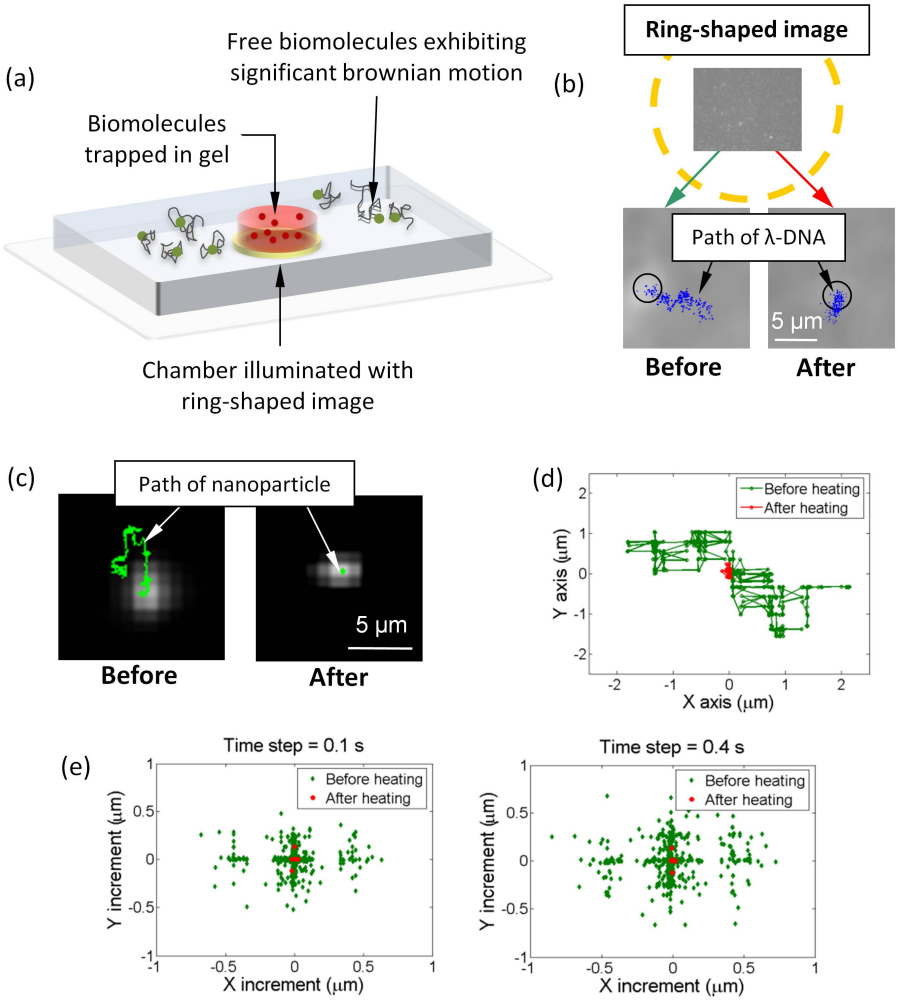

Figure 5.5. Creation of dynamic traps for biomolecules (a) Schematic demonstrating the optical image guided creation of dynamic traps for biomolecules. (b) Trapping of λ-DNA molecules by illuminating the microfluidic chip with a ring-shaped image. The particle trajectory of a λ-DNA molecule is shown before and after heating, indicating a significant suppression of particle diffusion. (c) Trapping of a 210 nm polystyrene nanoparticle. The particle trajectory is shown before and after heating, once again showing significant suppression of particle diffusion. (d) Superimposed particle trajectory of a sample polystyrene nanoparticle, before and after heating. (e) Distribution of the displacement the particle at time intervals of 0.1 s and 0.4 s, showing diffusive broadening with time before heating but no such broadening after heating.

This displacement data was used to characterize the effective particle diffusivity before and after heating[35] (See Supplementary Information, 5.8.3 for details on how particle trajectory information was used to find diffusivity). The diffusivity of the particles before heating was found to be $0.0446 \pm 0.0194\ \mu m^2/s$, and was found to be $0.0019 \pm 0.0096\ \mu m^2/s$ after heating, indicating an approximately 25 fold suppression of diffusion. The reason for the high standard deviation in the results for the "after heating" case is that the particle displacement was often within the range of noise for our readings.

5.6 Conclusions

We have demonstrated here an optofluidic approach to reconfigurable microfluidics using a chip with a photothermal absorbing substrate and a thermo-rheological solution that undergoes reversible sol-gel transition on heating. We have demonstrated the use of this approach to create reconfigurable channels and valves as well as to create dynamic traps for biomolecules. The pluronic solutions used here are biocompatible and have been approved by the FDA and the EPA as direct and indirect food additives, pharmaceutical ingredients and agricultural products[36]. This, along with their reversible gelation properties at temperatures close to physiological temperatures has led to use in a wide range of applications such as drug delivery[36,37] and gel electrophoresis[38]. Our rapid optofluidic approach to creating reconfigurable channel based microfluidic systems along with the strong biocompatibility of these solutions offers tremendous scope for developing versatile and robust microfluidic systems for lab-on-chip applications.

5.7 Acknowledgements

This work was supported by the Defense Advanced Research Projects Agency (DARPA), Defense Sciences Office (DSO) under the Programmable Matter program, and a CAREER grant from the National Science Foundation (NSF) for Optofluidics – Fusing Microfluidics and Photonics.

5.8 Supplementary Information

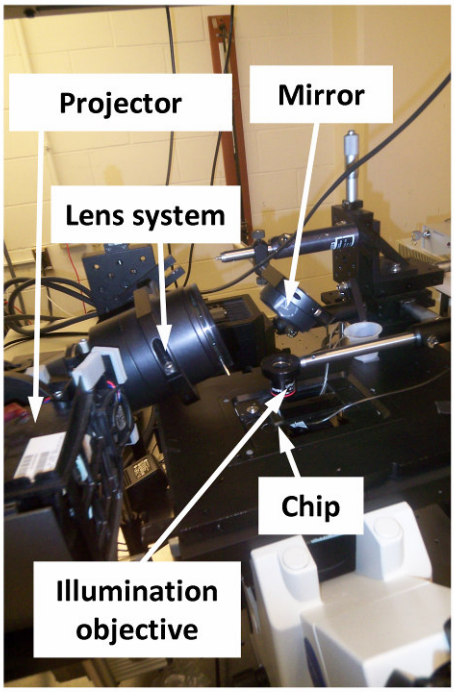

Figure 5.6. Opto-rheological setup. The microfluidic chip is placed upside down on the microscope, illuminated from above with light from the projector and imaged from below with another objective and a camera. Flow is driven through the chip using a syringe pump.

5.8.1 Photothermal absorbption layer

The substrate used in our experiments consists of a glass slide covered with a thin layer of PDMS, followed by an absorbing layer. 60g of PDMS (50g of PDMS A

mixed with 10g of PDMS B) was poured onto three glass slides placed in a petri dish and allowed to cure on a flat surface at room temperature overnight. The dish was then placed in a convection oven set at 80 ºC for 2 hours. This process ensured that the PDMS layer on the glass slide was flat. The reason for using a PDMS rather than glass substrate is to ensure that heat is better contained within the microfluidic chamber since the thermal conductivity of PDMS is less than that of glass (0.18 $Wm^{-1}K^{-1}$ for PDMS as opposed to 1.4 $Wm^{-1}K^{-1}$ for glass[25]). An absorbing layer was then created on top of this PDMS/glass substrate using a mixture of carbon black, PDMS A and PDMS B in the ratio 0.01:1:0.05 by weight. The process of preparing the absorbing layer was as follows. First, PDMS A and carbon black were mixed together and the mixture was sonicated for 2 hours. PDMS B was then added to the above mixture and this was dessicated for 20 minutes, followed by sonication for 30 minutes. The carbon black and PDMS mixture was then immediately spun on the PDMS/glass substrate to prevent the mixture from curing. The spinning was done at 1400 rpm with a ramp of 336 rpm/s. We also investigated the effect of varying spin speed on the thickness and transmission characteristics of the substrate as described below. After spinning, the substrate was once again dessicated for 30 minutes and then baked in a convection oven at 80 ºC for 2 hours.

We characterized the photothermal absorption layer by doing transmission measurements using an optical spectrophotometer. We carried out measurements at different concentrations of carbon black, though we were unable to carry out these measurements at the concentration eventually used for experiments since the transmission through those substrates was too low to be detected by the

spectrophotometer. We present results here for films having 0.4 times (0.4X) and 0.2 times (0.2X) the carbon black concentrations used in our final experiments. We prepared films on plain glass substrates at spin speeds in the range of 1000 – 4000 rpm, and measured both the thickness and the transmission of the films. The results are shown in Figures 5.7 and 5.8. The control here refers to measurements taken with no absorbing film. Two sets of measurements were carried out for each spin speed as indicated in Figure 5.7.

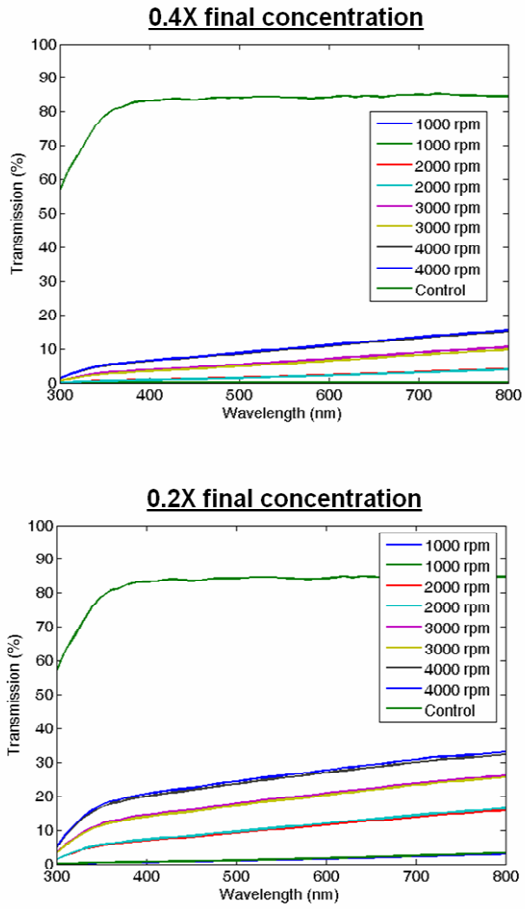

Figure 5.7. Characterization of photothermal absorption layer, transmission vs. wavelength. Transmission through the layer is plotted as a function of wavelength for different spin speeds.

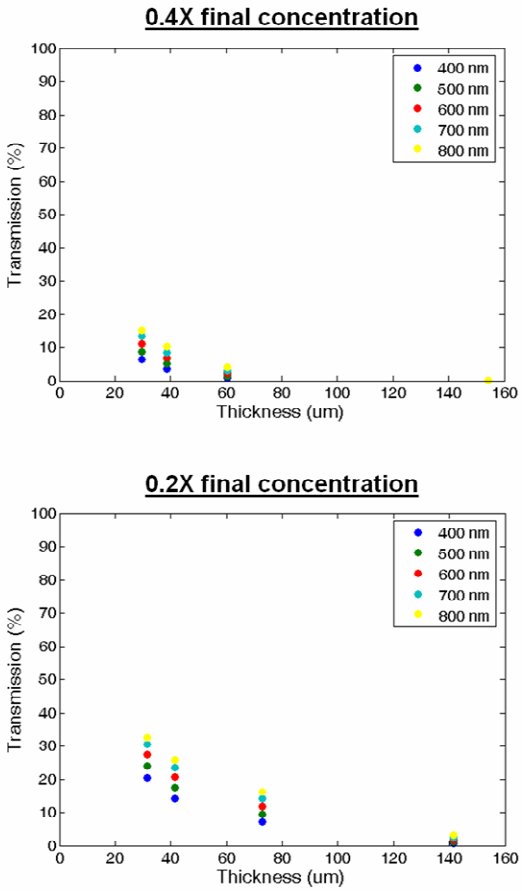

Figure 5.8. Characterization of photothermal absorption layer, transmission vs. absorber thickness. Transmission through the layer is plotted as a function of absorber thickness for different wavelengths.

It is clear through this data that transmission through the absorption layer can be modulated through two variables (a) the concentration of absorber or carbon black used and (b) the thickness of the absorption layer. We used fluidic modeling, and experimental trials to finally pick the concentration and thickness of carbon black used in the results discussed above. We found that spin speeds in the range of 1200 rpm –

1400 rpm, and a carbon black to PDMS A to PDMS B ratio of 0.01:1:0.05 gave us the best heating results, with just enough heat being input to the system to cause gelation but not too much heat to unduly gel the entire fluidic chamber.

5.8.2 Fluid dynamic modeling

Fluidic simulations were carried out using COMSOL. Since the thermal Peclet number characterizing our system is low, we expect diffusion to dominate over convection in the heat transfer. The Peclet number, *Pe* is defined as $Pe = Ul/\alpha$, where U is the characteristic velocity, l the characteristic length and α the thermal diffusivity. Typical values for our system are U = 500 µm/s, l = 50 µm (channel height) and α = 1.4×10^{-7} m^2/s, thus Pe = 0.18. We therefore modeled only the diffusion equation while solving the heat transfer problem. The equation we solved for was

$$\nabla \cdot (k \nabla T) = 0 \qquad (5.1)$$

where k is the thermal conductivity and T is the temperature. While analyzing the effects of the thickness and absorbance of the photothermal absorption layer as discussed below, we solved a modified version of the above equation for the domain containing the absorption layer, to include a volumetric heat source term q such that

$$\nabla \cdot (k \nabla T) + q = 0 \qquad (5.2)$$

We have carried out fluidic simulations using COMSOL in order to investigate the effect of substrate thickness and substrate absorption characteristics on the temperature rise in the fluid in a microfluidic chamber. From the Beer-Lambert law, for light of intensity I_0 incident on an absorbing layer of thickness x, having an

absorption coefficient α, the transmitted light intensity, I (assuming no reflection from the surface) is given by

$$I = I_0 e^{-\alpha x} \qquad (5.3)$$

while the volumetric heat flux generated through the absorber, q is given by

$$q = -\frac{dI}{dx} = \alpha I_0 e^{-\alpha x} \qquad (5.4)$$

We modeled the heat transfer due to this volumetric heating for photothermal absorption layers of different thickness and having different absorption characteristics. Based on the transmission measurements carried described in Section S1, we considered absorber layers having absorption coefficients, α of 0.04 μm^{-1}, 0.07 μm^{-1} and 0.18 μm^{-1}. For each of these values of absorption coefficients, we carried out simulations for substrates having thickness varying from 25 - 200 μm. The microfluidic chip used for the simulations is shown in Figure 2a where the simulated region is half the actual chip since the temperature profile is symmetric across the x axis. The microfluidic chamber modeled in these simulations had dimensions 1mm X 1mm X 50 μm. The region of heating was a rectangle of dimensions 100 μm X 100 μm, located at the center of the chip. Convective flux boundary conditions were applied at all the external interfaces except the plane of symmetry at which a thermal insulation boundary condition ($\nabla T \cdot n = 0$) was applied, and the bottom substrate at which a constant temperature boundary condition was applied.

5.8.3 Calculation of diffusion coefficients

Trajectory data similar to that shown in Figure 5c was used to calculate the diffusion coefficients of the polystyrene beads before and after heating. Trajectory data was obtained using the Video Spot Tracker software developed by the Computer Integrated Systems for Microscopy and Manipulation (CISMM) at UNC Chapel Hill, or the ParticleTracker plugin for ImageJ. To do this, we used a relation described in[35] that helps account for the error in measuring particle variance due to limitations on the spatial and temporal resolution of the system. The details of this analysis are not presented here and the readers are referred to Savin *et al.*[35] for further reference. The trajectory data indicates the (x, y) position of a particle as a function of time. With this data, it was possible to extract incremental displacements, ($\Delta x(t)$, $\Delta y(t)$) of particles at 4 different time intervals t of 0.1 - 0.4s. This was done by measuring the displacement of the particle from an initial position through the desired time interval, for multiple initial positions through the particle trajectory, to create a distribution of particle displacements. As described in Savin *et al.*[35], the variance of the measured displacement in the x direction or Δx, given by $Var(\Delta x)$ is then given by the relation,

$$Var(\Delta x) = 2D(t - \sigma/3) + 2\varepsilon^2 \qquad (5.5)$$

where σ indicates the exposure time of the measurement, ε denotes the spatial resolution of the system and D denotes the diffusion coefficient. The exposure time for our measurements was 0.1 s. We combined the data along the x and y axis to get a better estimate for D, using the relation

$$(Var(\Delta x) + Var(\Delta y))/2 = 2D(t - \sigma/3) + 2\varepsilon^2 \qquad (5.6)$$

The variances were calculated from the measured displacement data for different time intervals as discussed above and plotted against (t – σ/3). A sample data set is shown in Figure 5.9 for a particle before and after heating. The Matlab curve fitting tool box was then used to obtain a linear fit to such data for 10 different particles. The slope of the curve in each case is equal to twice the diffusion coefficient as seen from Equation 6.

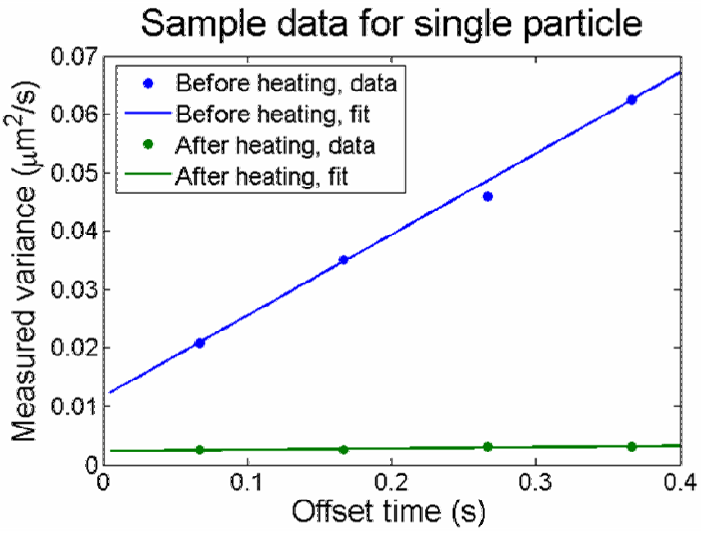

Figure 5.9. Net variance of position vs. time for 210 nm polystyrene bead before and after heating. The slope of the line before heating is 0.139 $\mu m^2/s$ and after is 0.002 $\mu m^2/s$, corresponding to diffusivities of 0.069 $\mu m^2/s$ and 0.001 $\mu m^2/s$ respectively (See Section 3 for details).

REFERENCES

1. Stone, H. A., Stroock, A. D. & Ajdari, A. Engineering flows in small devices: Microfluidics toward a lab-on-a-chip. *Annual Review of Fluid Mechanics* **36** (2004).

2. Duffy, D. C., McDonald, J. C., Schueller, O. J. A. & Whitesides, G. M. Rapid prototyping of microfluidic systems in poly(dimethylsiloxane). *Analytical Chemistry* **70** (1998).

3. Thorsen, T., Maerkl, S. J. & Quake, S. R. Microfluidic large-scale integration. *Science* **298** (2002).

4. Pollack, M. G., Shenderov, A. D. & Fair, R. B. Electrowetting-based actuation of droplets for integrated microfluidics. *Lab on a Chip* **2** (2002).

5. Miller, E. M. & Wheeler, A. R. A digital microfluidic approach to homogeneous enzyme assays. *Analytical Chemistry* **80** (2008).

6. Teh, S. Y., Lin, R., Hung, L. H. & Lee, A. P. Droplet microfluidics. *Lab on a Chip* **8** (2008).

7. Psaltis, D., Quake, S. R. & Yang, C. H. Developing optofluidic technology through the fusion of microfluidics and optics. *Nature* **442** (2006).

8. Monat, C., Domachuk, P. & Eggleton, B. J. Integrated optofluidics: A new river of light. *Nature Photonics* **1** (2007).

9. Casner, A. & Delville, J. P. Laser-induced hydrodynamic instability of fluid interfaces. *Physical Review Letters* **90** (2003).

10. MacDonald, M. P., Spalding, G. C. & Dholakia, K. Microfluidic sorting in an optical lattice. *Nature* **426** (2003).

11. Chiou, P. Y., Ohta, A. T. & Wu, M. C. Massively parallel manipulation of single cells and microparticles using optical images. *Nature* **436** (2005).

12. Liu, G. L., Kim, J., Lu, Y. & Lee, L. P. Optofluidic control using photothermal nanoparticles. *Nat. Mater.* **5** (2006).

13. Ohta, A. T., Jamshidi, A., Valley, J. K., Hsu, H. Y. & Wu, M. C. Optically actuated thermocapillary movement of gas bubbles on an absorbing substrate. *Applied Physics Letters* **91** (2007).

14. Weinert, F. M. & Braun, D. Optically driven fluid flow along arbitrary microscale patterns using thermoviscous expansion. *J. Appl. Phys.* **104** (2008).

15. Sershen, S. R. *et al.* Independent optical control of microfluidic valves formed from optomechanically responsive nanocomposite hydrogels. *Advanced Materials* **17** (2005).

16. Shirasaki, Y. *et al.* On-chip cell sorting system using laser-induced heating of a thermoreversible gelation polymer to control flow. *Analytical Chemistry* **78** (2006).

17. Krishnan, M., Park, J. & Erickson, D. Opto-thermorheological flow manipulation *Optics Letters* **34** (2009).

18. Sugiura, S. *et al.* On-demand microfluidic control by micropatterned light irradiation of a photoresponsive hydrogel sheet. *Lab on a Chip* **9** (2009).

19. Wanka, G., Hoffmann, H. & Ulbricht, W. The aggregation behavior of poly-(oxyethylene)-poly-(oxypropylene)-poly-(oxyethylene)-block-copolymers in aqueous solution. *Colloid and Polymer Science* **268** (1990).

20. Wanka, G., Hoffmann, H. & Ulbricht, W. Phase-Diagrams and Aggregation Behavior of Poly(Oxyethylene)-Poly(Oxypropylene)-Poly(Oxyethylene) Triblock Copolymers in Aqueous-Solutions. *Macromolecules* **27** (1994).

21. McDonald, J. C. *et al.* Fabrication of microfluidic systems in poly(dimethylsiloxane). *Electrophoresis* **21** (2000).

22. Stoeber, B., Yang, Z. H., Liepmann, D. & Muller, S. J. Flow control in microdevices using thermally responsive triblock copolymers. *Journal of Microelectromechanical Systems* **14** (2005).

23. Erickson, D., Sinton, D. & Li, D. Q. Joule heating and heat transfer in poly(dimethylsiloxane) microfluidic systems. *Lab on a Chip* **3** (2003).

24. Samy, R., Glawdel, T. & Ren, C. L. Method for microfluidic whole-chip temperature measurement using thin-film poly(dimethylsiloxane)/Rhodamine B. *Analytical Chemistry* **80** (2008).

25. Moerner, W. E. New directions in single-molecule imaging and analysis. *Proceedings of the National Academy of Sciences of the United States of America* **104** (2007).

26. Xu, X. H. N. & Yeung, E. S. Long-range electrostatic trapping of single-protein molecules at a liquid-solid interface. *Science* **281** (1998).

27. Tegenfeldt, J. O. *et al.* The dynamics of genomic-length DNA molecules in 100-nm channels. *Proceedings of the National Academy of Sciences of the United States of America* **101** (2004).

28. Huh, D. *et al.* Tuneable elastomeric nanochannels for nanofluidic manipulation. *Nature Materials* **6** (2007).

29. Ashkin, A., Dziedzic, J. M., Bjorkholm, J. E. & Chu, S. Observation of a single-beam gradient force optical trap for dielectric particles. *Optics Letters* **11** (1986).

30. Grier, D. G. A revolution in optical manipulation. *Nature* **424** (2003).

31. Yang, A. H. J. *et al.* Optical manipulation of nanoparticles and biomolecules in sub-wavelength slot waveguides. *Nature* **457** (2009).

32. Mandal, S., Serey, X. & Erickson, D. Nanomanipulation Using Silicon Photonic Crystal Resonators. *Nano Lett.* **10** (2009).

33. Chaibundit, C. *et al.* Effect of ethanol on the gelation of aqueous solutions of Pluronic F127. *Journal of Colloid and Interface Science* **351** (2010).

34. Chiu, D. T. & Zare, R. N. Biased diffusion, optical trapping, and manipulation of single molecules in solution. *Journal of the American Chemical Society* **118** (1996).

35. Savin, T. & Doyle, P. S. Static and dynamic errors in particle tracking microrheology. *Biophysical Journal* **88** (2005).

36. Bromberg, L. E. & Ron, E. S. Temperature-responsive gels and thermogelling polymer matrices for protein and peptide delivery. *Advanced Drug Delivery Reviews* **31** (1998).

37. Cohn, D., Sosnik, A. & Levy, A. Improved reverse thermo-responsive polymeric systems. *Biomaterials* **24** (2003).

38. Ugaz, V. M., Lin, R. S., Srivastava, N., Burke, D. T. & Burns, M. A. A versatile microfabricated platform for electrophoresis of double- and single-stranded DNA. *Electrophoresis* **24** (2003).

CHAPTER 6

CONCLUSIONS

I was able to develop two approaches to programmable matter. In the first approach, simulations and experiments were used to investigate a novel fluidic assembly paradigm to create programmable and reconfigurable target structures. In the second approach, I developed an optofluidic technique to creating dynamically reconfigurable microfluidic systems. Below, I present a summary of my research accomplishments and contributions by project.

6.1 Summary of Individual Accomplishments by Project

6.1.1 Analytical Modeling of Fluidic Assembly

- Developed a two-dimensional model for fluid-solid interaction in a fluidic assembly process.
- Validated model by comparison to experiments and three dimensional simulations.
- Developed docking parameters to quantitatively compare different assembly schemes.
    - Inlet jets orthogonal to direction of tile motion gave most successful assembly results.
    - Dual outlet configuration helped tile alignment.
    - Hexagonal tiles underwent minimal rotation in flow field.

- First effort at modeling and quantifying the success of a dynamic fluidic assembly process.

6.1.2 Dynamic Tuning of Affinities in Fluidic Assembly

- Demonstrated the ability to hydrodynamically tune affinities between assembling components using a thermorheological fluid.
- Demonstrated tile reconfiguration, the creation of irregular structures and error correction using this approach.
    - First demonstration of the above in a fluidic assembly process
- Potential to enable assembly of arbitrary, non-predefined and reconfigurable target structures.
- Applications to self healing structures, tunable electronics and displays.

6.1.3 Opto-thermorheological valving

- Reversible fluid valve created using laser beam incident on an absorbing substrate with a thermorheological fluid.
- First demonstration of low power, rapid, dynamic microfluidic flow valving.
- Used low power 40 mW laser for valving.
- Obtained switching times on the order of a second at high flow rates of 1 mm/s.

6.1.4 Optical Image Guided Microfluidic Reconfiguration

- Developed a rapid optofluidic technique to create, move, and remove arbitrary solid regions in a microfluidic flow.
- Demonstrated the ability to create reconfigurable flow pathways and build morphable channel structures.
- Demonstrated dynamic flow modulation on the order of seconds.
- Technique applied to creating dynamic traps for biomolecules, by direct suppression of particle diffusion.
    - Demonstrate trapping of λ-DNA molecules and nanoparticles.
    - 25 fold suppression of diffusion.
- First step to creating truly reconfigurable microfluidic systems similar to FPGAs in the field of electronics.

6.2 Future Directions

6.2.1 Analytical Modeling of Fluidic Assembly

It is possible to further develop the fluid-solid interaction model I have proposed to investigate more accurate models, models of a different nature and explore a wider space of assembly schemes, as discussed below.

- Extend current model.
    - Model could be extended from the single tile system presented here to a multi-tile system, especially given the computational ease of these two-dimensional simulations.

- Model could also be expanded to include the effect of tile-tile and tile-substrate collisions.

- Develop alternate models
  - Hele-Shaw flow cell modeling approaches could be investigated to mitigate the need to solve the full Navier-Stokes equations.
  - The coupling of these kinds of flow equations with control schemes for assembly could be further investigated.

- Investigate further assembly schemes
  - The space of assembly schemes could be further investigated, to better optimize flow and tile geometries for successful assembly.

6.2.2 Dynamic Tuning of Affinities in Fluidic Assembly

- Implementation of on-chip valving
  - We have previously explored the fabrication of on-chip heaters to create on-chip valves, and a further investigation of this area would be a possible future direction of this work

- Three-dimensional assembly
  - Currently, our assembly process consists of a two-dimensional planar assembly approach. Based on the work presented here, and other collaborative work, our research group has also explored the extension of this process to three dimensions[1].

- Extension to large scale assembly

- The assembly process described in Chapters 2 and 3 has been used with silicon tiles on the order of 100 – 500 μm[2-4]. There has been work in our research group to extend this to larger sized assembling components to build macroscale structures, as well as equip these structures with on-chip valves[5].

- Alternative approaches to dynamic assembly
  - The paradigm of dynamically tuning assembly affinities has great potential to creating truly programmable structures. Others in our research group have explored alternative approaches to tunable affinities using on-tile bubbles created using the laser actuation system I developed for opto-thermorheological valving[6].

- Combination of various fluidic assembly paradigms
  - The fluidic assembly paradigm presented in Chapters 2 and 3 are uniquely suited to creating programmable systems. However, a disadvantage of this approach is that the assembly process can prove to be slow, and provide more accuracy of assembly than is perhaps necessary for the target structure. An alternative scalable assembly paradigm could then involve a hybrid approach involving more traditional self-assembly type and hierarchical assembly approaches for "coarse" assembly followed by the use of the fluidic assembly techniques presented here for fine control.

6.2.3 Opto-thermorheological valving

- Further investigate current system
    - Alternative pluronic solutions[7,8], as well as other polymer solutions could be investigated for improved valving times and lowering leakage through valves.
    - Alternative absorbing substrates like carbon black substrates or photothermal nanoparticles[9] could be investigated to further reduce power requirements of system.
    - Alternate arrangements for optical illumination (similar to the spatial modulation arrangement described in Chapter 5) could be investigated to implement multiple valving sites on a single chip.
- Explore alternative valving arrangements
    - The current valving arrangement requires the pluronic solution used for valving to be the active medium of flow. We could also investigate the use of a dual layered system similar to that used for multilayered pumps and valves[10] to further extend the capabilities of this system.
- Applications of dynamic valving
    - This approach of dynamic valving could be used to implement flow cytometry and sorting[11].

6.2.4 Optical Image Guided Microfluidic Reconfiguration

Some of the future directions described above for the opto-thermorheological valving could also be applicable here, in terms of the exploration of alternate polymer blends and absorbing materials for improved performance. In what follows therefore, I will only specifically list future applications that I envision for this system.

- Directed Fluidic Assembly
    - This approach of creating dynamically reconfigurable channel structures could be combined with the fluidic assembly paradigm described in Chapters 2 and 3, to create more versatile assembly processes. Specific pathways could be defined on-the-fly in an assembly chamber along which to direct tiles to target sites, further minimizing assembly errors. Additionally, since structures can now be created and stored in gelled regions of the chip, hierarchical assembly of units is easily made possible.
- Biological Analysis
    - The dynamic trapping experiments described using this technique provide unique tools for single molecule analysis. We could examine the use of this approach with either label or label-free detection techniques for biological analysis[12].
- Thermophoresis
    - The ability to dynamically create and tune thermal fields on chip using optical patterns is being investigated in our research group to

dynamically create waveguides through the thermophoretic action of polystyrene nanoparticles[13].

- Flow actuation
    - Other researchers have presented the ability to actuate flow by asymmetric heating of water and the resulting viscosity gradients[14]. Our spatial light modulation approach, coupled with the use of pluronic solutions that have a strong dependence of viscosity on temperature, could thus be used as both a flow actuation and a flow reconfiguration system.

6.3 Concluding Remarks

I believe my work has helped introduce and develop the paradigm of programmable systems as applied to and enabled by microfluidics. I strongly hope the scientific and engineering contributions I have made shall enable this paradigm to be broadly applied to this field, to create robust and versatile microfluidic tools for the creation of dynamic lab-on-chip devices.

REFERENCES

1. Kalontarov, M., Tolley, M. T., Lipson, H. & Erickson, D. Hydrodynamically driven docking of blocks for 3D fluidic assembly. *Microfluidics and Nanofluidics* **9** (2010).

2. Krishnan, M., Tolley, M. T., Lipson, H. & Erickson, D. Hydrodynamically Tunable Affinities for Fluidic Assembly. *Langmuir* **25** (2009).

3. Krishnan, M., Tolley, M. T., Lipson, H. & Erickson, D. Increased robustness for fluidic self-assembly. *Physics of Fluids* **20** (2008).

4. Tolley, M. T., Krishnan, M., Erickson, D. & Lipson, H. Dynamically programmable fluidic assembly. *Applied Physics Letters* **93** (2008).

5. Neubert, J. *et al.* in *2010 IEEE International Conference on Robotics and Automation (ICRA 2010).* 2479-2484 (Ieee).

6. Krishnan, M., Park, J. & Erickson, D. Opto-thermorheological flow manipulation *Optics Letters* **34** (2009).

7. Wanka, G., Hoffmann, H. & Ulbricht, W. Phase-diagrams and aggregation behavior of poly(oxyethylene)-poly(oxypropylene)-poly(oxyethylene) triblock copolymers in aqueous-solutions. *Macromolecules* **27** (1994).

8. Wanka, G., Hoffmann, H. & Ulbricht, W. The aggregation behavior of poly-(oxyethylene)-poly-(oxypropylene)-poly-(oxyethylene)-block-copolymers in aqueous solution. *Colloid and Polymer Science* **268** (1990).

9. Liu, G. L., Kim, J., Lu, Y. & Lee, L. P. Optofluidic control using photothermal nanoparticles. *Nat. Mater.* **5** (2006).

10. Unger, M. A., Chou, H. P., Thorsen, T., Scherer, A. & Quake, S. R. Monolithic microfabricated valves and pumps by multilayer soft lithography. *Science* **288** (2000).

11. Shirasaki, Y. *et al.* On-chip cell sorting system using laser-induced heating of a thermoreversible gelation polymer to control flow. *Analytical Chemistry* **78** (2006).

12. Mandal, S., Goddard, J. M. & Erickson, D. A multiplexed optofluidic biomolecular sensor for low mass detection. *Lab on a Chip* **9** (2009).

13. Duhr, S. & Braun, D. Why molecules move along a temperature gradient. *Proceedings of the National Academy of Sciences of the United States of America* **103** (2006).

14. Weinert, F. M. & Braun, D. Optically driven fluid flow along arbitrary microscale patterns using thermoviscous expansion. *J. Appl. Phys.* **104** (2008).